Integrating photosystem II and electroactive bacteria with three-dimensional electrodes for semi-artificial photosynthesis

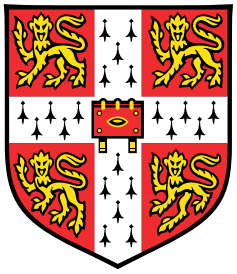

Xin Fang

Supervisor: Prof. Erwin Reisner

Department of Chemistrty
University of Cambridge

This dissertation is submitted for the degree of
Doctor of Philosophy

Queens' College July 2019

They who know the truth are not equal to those who love it, and they who love it are not equal to those who delight in it.

— Confucius (551–479 BC.)

Declaration

I hereby declare that except where specific reference is made to the work of others, the contents of this dissertation are original and have not been submitted in whole or in part for consideration for any other degree or qualification in this, or any other university. This dissertation is my own work and contains nothing which is the outcome of work done in collaboration with others, except as specified in the text and Acknowledgements. This dissertation contains fewer than 60,000 words including appendices, bibliography, footnotes, tables and equations and has fewer than 150 figures.

Xin Fang
July 2019

Acknowledgements

This thesis is under the supervision of Prof. Erwin Reisner, to whom I extend my greatest gratitude. This thesis is supported by the PhD studentship from China Scholarship Council and the Cambridge Trust as well as the research funding from an European Research Council Consolidator Grant.

I am greatly indebted to the following people, without whom the completion of this thesis would not have been possible. Dr. Katarzyna Sokol shared her skills and protocols in electrode preparation and protein film-photoelectrochemistry. Dr. Shafeer Kalathil brought in his knowledge and expertise in microbiology and made pivotal contributions to the second half of this thesis. Dr. Nina Heidary set up the in situ infrared spectroscopy and performed the measurements. Dr. Giorgio Divitini acquired focused ion beam-scanning electron microscopy images. Dr. Qian Wang prepared $BiVO_4$ photoanodes and assisted in oxygen quantification. Prof. A.William Rutherford and Dr. Andrea Fantuzzi from Imperial College London generously provided photosystem II for this study. I would also like to recognise those who have kindly offered assistance throughout the duration of my study: Dr. Heather Greer for electron microscopy, Dr. Demetra Achilleos for X-ray diffraction analysis, Dr. Martin O. Lenz for confocal fluorescence microscopy, Mr. Daniel Anton Garcia for fluorescence spectroscopy, Dr. Michael Casford for atomic force microscopy, Dr. Jane Leung for contact angle measurements, Mr. Adam Brown for X-ray microscopy, Dr. Feng Zheng for numerical simulations, Mr. Arjun Vijeta for NMR quantification, and Dr. Souvik Roy for gas chromatography. Dr. Jenny Zhang, Dr. Nikolay Kornienko, Dr. William Robinson, Ms. Melanie Miller are also acknowledged for their helpful feedback and suggestions on the results presented in this thesis.

It has been a true privilege to complete my PhD degree here at the University of Cambridge. I am grateful to all the colleagues in the Reisner group and Queens' College, who have been constructive, supportive and firmly behind my efforts and goals. It has been a great pleasure to work with so many inspirational, knowledgeable, professional and resourceful individuals who have demonstrated their true belief in integrity, openness, cooperation and

dedication, and who constitute a great team with unwavering commitment to shaping the future with advances in science and technology. I have drawn endless strength from their expertise, creativity, guidance and persistence, and their immense determination to pursue the first-class research leading the field. I remain indebted to many others who have left the group and have helped me set out my PhD project and nurtured my initial ventures in Cambridge. Last, but not least, thanks are also due to my friends and family, to whom my gratitude is more than words can describe.

Abstract

Artificial photosynthesis is at the forefront of strategies to tackle the global reliance on fossil fuels and shape the contour of a sustainable future fuelled by renewable resources. In this way, solar energy is harvested and stored into chemical bonds to render it viable for transport and utilisation. Yet coordinating the interwoven processes therein in an efficient and orderly fashion poses profound challenges for synthetic chemistry. Biology wields plenty of evolutionarily-optimised biosynthetic pathways that operate in concert to yield complex chemicals from simple feedstocks. This thesis aims to achieve the solar-to-chemical conversion through a semi-biological approach: biocatalytic machinery in the form of enzymes and whole cells were integrated with artificial electronics to repurpose their biochemical pathways for the production of value-added fuels and chemicals.

In particular, this thesis works with three-dimensional electrodes with different materials and variable morphologies to host photosynthetic enzymes and electroactive bacteria as biocatalysts. Chapter 1 introduces the fundamentals of biocatalysis and artificial photosynthesis, and reviews the progressing efforts to integrate biocatalysts with synthetic materials for semi-artificial photosynthesis. The rationale and contents of this thesis are outlined at the end of this chapter. Chapter 2 provides the experimental details that underlie this thesis, including protocols for electrode preparation, enzyme separation, bacteria culturing and an array of analytical methodologies. Chapter 3 presents a systematic study on benchmark inverse opal-indium tin oxide (IO-ITO) electrodes for protein film-photoelectrochemistry with photosystem II. The relationships of IO-ITO electrode structure and photosystem II activity were discussed following a combination of microscopic, spectroscopic and photoelectrochemical characterisations. Chapter 4 reports an inverse opal-graphene electrode as the host for photosystem II. The enzyme activity in such carbon-based electrodes is quantified by protein-film photoelectrochemistry and further compared with that in IO-ITO counterparts. Chapter 5 tailors the structure of the IO-ITO electrode to accommodate metal-reducing bacteria *Geobacter sulfurreducens* and *Shewanella loihica*. Their colonisation and current production in electrodes arising from anaerobic respiration are studied. Chapter 6 utilises the resulting biohybrid electrodes to drive reducing reactions within and beyond their native

metabolic pattern, with electrons supplied by an external circuit or ultimately outsourced to a photoanode. Chapter 7 summarises the key findings in this thesis and blueprints future directions of research in this field. The research represents an interdisciplinary approach that takes advantages of biocatalysis featuring high selectivity and efficiency in chemical transformation, and synergistically combines strengths of synthetic materials and analytic toolsets, to induce shifts in the production of high value fuels and chemicals with renewable energy sources.

Table of contents

List of figures

List of tables

Glossary

Symbols

η_F	Faraday efficiency
C	Specific capacitance

Abbreviations

AFM	Atomic force microscope
ATP	Adenosine triphosphate
ATR-IR	Attenuated total reflection infrared
CLSM	Confocal laser scanning microscope
CODH	Carbon monoxide dehydrogenase
CV	Cyclic voltammetry
Cyt	Cytochrome
DCBQ	2,6-Dichloro-1,4-benzoquinone
DCMU	3-(3,4-Dichlorophenyl)-1,1-dimethylurea
DET	Direct electron transfer
EDTA	Ethylenediaminetetraacetic acid
EDX	Energy dispersive X-ray
EET	Extracellular electron transfer
FDH	Formate dehydrogenase

FIB	Focused ion beam
FNR	Ferredoxin-NADP reductase
G. sulfurreducens	*Geobacter sulfurreducens*
GO	Graphene oxide
H_2ase	Hydrogenase
HER	Hydrogen evolution reaction
HOMO	Highest occupied molecular orbital
ICP-OES	Inductively coupled plasma-optical emission spectrometry
IO-ITO	Inverse opal-indium tin oxide
IO	Inverse opal
IR	Infrared
ITO	Indium tin oxide
LUMO	Lowest unoccupied molecular orbital
M. barkeri	*Methanosarcina barkeri*
M. thermoacetica	*Moorella thermoacetica*
MES	2-(*N*-morpholino)ethanesulfonic acid
MET	Mediated electron transfer
NADPH	Nicotinamide adenine dinucleotide phosphate
NMR	Nuclear magnetic resonance
OD	Optical density
OEC	Oxygen evolving centre
OER	Oxygen evolution reaction
PEC	Photoelectrochemistry
PF-PEC	Protein film-photoelectrochemistry

PFE	Protein film electrochemistry
PSII	Photosystem II
PSI	Photosystem I
PS	Polystyrene
PV	Photovoltaics
Q_A	Plastoquinone A
Q_B	Plastoquinone B
RGO	Reduced graphene oxide
ROS	Reactive oxygen species
S. loihica	*Shewanalle loihica*
S. ovata	*Sporomusa ovata*
SEM	Scanning electron microscopy
SHE	Standard hydrogen electrode
STEM	Scanning transmission electron microscopy
TCA	Tricarboxylic acid
TEM	Transmission electron microscopy
TEOA	Triethanolamine
TOF	Turnover frequency
UV–vis	Ultraviolet–visible
XRD	X-ray diffraction

Chapter 1

Introduction

The growing consequences of anthropogenic carbon emissions calls for innovative strategies to eliminate the global reliance on fossil fuels. Harnessing the solar light as a source of energy is a promising avenue toward a sustainable future. Photovoltaics (PV) is the leading technology of solar energy conversion,[1,2] but is plagued with disadvantages in electricity transmission and intermittency. Artificial photosynthesis circumvents these drawbacks by storing the solar energy into chemical bonds with synthetic materials as light absorbers and catalysts.[3,4] While synthetic catalysts still struggle to fulfil the solar-to-chemical conversion in an effective way, nature sets a perfect example of doing this through evolutionarily-optimised biocatalytic machinery. Within such context, this thesis deals with how the biocatalytic machinery can be leveraged to catalyse light-driven chemical reactions by an emerging technology termed "semi-artificial photosynthesis". This is carried out by incorporating biocatalysts in the form of enzymes or whole cells into structurally-crafted electrodes and subjecting the resulting biohybrid systems to (photo)electrochemical controls. Specifically, the first half of the thesis utilised photosystem II (PSII), a photosynthetic enzyme, as the water-oxidising biocatalyst to carry out the bottleneck oxygen evolution reaction during photocatalytic water splitting. The second half of the thesis employed *Geobacter sulfurreducens* (*G. sulfurreducens*), an electroactive bacterium, as a model biocatalyst in the form of whole cell, to synthesise chemicals both within and beyond the scope of metabolism. The nexus of these studies is the three-dimensional electrode with an inverse opal architecture that served as conductive scaffolds to physically integrate biocatalysts and electrochemically control the catalytic reactions. In this chapter, I first introduce the biological processes taking place in natural photosynthesis, and artificial strategies to harness solar energy for water splitting and CO_2 reduction. This is followed by an overview of the rationale and implementation of semi-artificial photosynthesis, with enzymes and microorganisms as

biocatalysts. Then the discussion is focused on the photoelectrochemistry (PEC) of PSII and the electrochemistry of *G. sulfurreducens* with emphasis on the underlying electrode structures.

1.1 Natural photosynthesis

Photosynthesis occurs in photoautotrophs spanning from cyanobacteria, algae and higher plants, which harvest solar energy to produce biomass and O_2 from H_2O and CO_2. Photosynthesis is accomplished by two phases of reactions: the light reaction uses solar light energy to generate energy carrier adenosine triphosphate (ATP) and reducing agent nicotinamide adenine dinucleotide phosphate (NADPH), whereas the dark reaction uses the ATP and NADPH to reduce atmospheric CO_2 into carbohydrates through the Calvin cycle.[5]

1.1.1 Light reactions

The light reaction is carried out by the photosynthetic apparatus in the thylakoid membrane of chloroplasts, including two photosystems, cytochrome b_6f (cyt b_6f), plastoquinone pool, plastocyanin, ferredoxin, ferredoxin-NADP reductase (FNR) and ATP synthase (**Figure 1.1a**). The main light absorbers are two photosystems that contain antenna complexes and reaction centres. The antenna complex comprises hundreds of pigments (chlorophylls and carotenoids), which capture photons and funnel the light energy to the reaction centre at high quantum efficiency of >95%. The reaction centre is a transmembrane protein-pigment complex, where electrons are excited and transferred to the downstream pathway for chemical synthesis. The reaction centre chlorophylls in PSII and photosystem I (PSI) are known as P680 and P700 respectively, due to their light absorption maxima (P stands for pigment and the figure suffix denotes wavelength). The two photosystems and cofactors function in concert to efficiently transfer electrons from H_2O to $NADP^+$ through a "Z scheme" (**Figure 1.1b**). The electron transfer on the thylakoid membrane is initiated by PSII that absorbs a photon and extracts an electron from H_2O to its primary electron acceptor, plastoquinone (PQ). The fully reduced plastohydroquinone (PQH_2) dissociates from the reaction centre, diffuses in the hydrocarbon portion of the membrane and transfers its electrons to cyt b_6f, which further passes electrons to PSI via a small copper-containing protein plastocyanin. At PSI, the arriving electron is energised by a second excitation and finally delivered to ferredoxin-NADP reductase to reduce $NADP^+$ to NADPH (**Figure 1.1a**).[5]

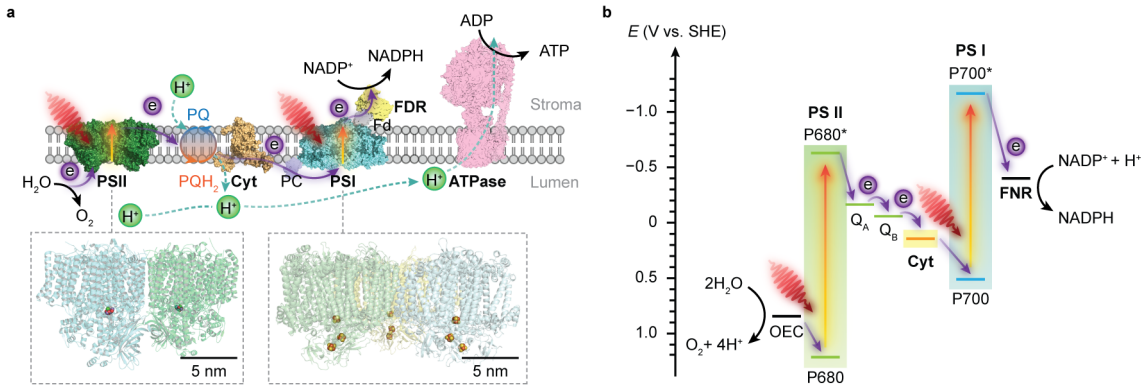

Figure 1.1 Schematic illustration of the light reaction of natural photosynthesis. **a.** Electron and proton transfer pathways in the thylakoid membrane. At the start of the photosynthetic chain is PSII that oxidises H_2O and liberates O_2 and protons upon light absorption. Electrons are delivered to PSI via a plastoquinone (PQ) pool, cyt b_6f and plastocyanin (PC). Electrons are photoexcited for a second time at PSI to reduce $NADP^+$ to NADPH by ferredoxin (Fd) and ferredoxin-NADP reductase (FNR). The water oxidation and electron transport also induces proton translocation from stroma to lumen, which generates proton gradient and chemiosmosis driving the synthesis of ATP by ATP synthase (ATPase). Protein data bank ID: PSII (4ub6), cyt b_6f (4h44), PC (1bxu), PSI (5oy0), Fd-FDR (2yvj), ATPase (6fkf). **b.** Energy level diagram of the Z-scheme electron transfer in the thylakoid membrane. The redox carriers are placed at their midpoint redox potentials at pH 7.

1.1.2 Carbon reactions

The NADPH and ATP produced by the light reaction are used to reduce CO_2 to carbohydrates through the Calvin cycle. During the process, CO_2 and H_2O are enzymatically combined with a carbon acceptor ribulose-1,5-bisphosphate to yield two molecules of 3-phosphoglycerate. This intermediate is then reduced into glyceraldehyde-3-phosphate with ATP and NADPH donated by the light reaction. The cycle ends up with the regeneration of ribulose-1,5-bisphosphate, the initial CO_2 acceptor.[6] Calvin cycle accounts for more than 90% of carbon assimilation on earth. Central to this is ribulose-1,5-biphosphate carboxylase/oxygenase (Rubisco) that covalently fixes CO_2 to a carbon skeleton.[7,8] In contrast to its abundance and ubiquity in nature is its slow catalysis and low selectivity. The TOF of Rubisco is typically less than 10 s^{-1}, rendering the photosynthetic CO_2 fixation inefficient under optimal conditions.[8] Moreover, Rubisco confuses the substrate (CO_2) and product (O_2) of photosynthesis, which offsets the CO_2 uptake and saddles oxygenic phototrophs with energy-dissipating photorespiration.[9] The photorespiration could consume 25% of carbon photosynthetically fixed by C3 plants and such carbon loss is more severe at higher temperature. Some tropical plants, namely C4 plants, overcome the disadvantageous photorespiration by deploying an addition

C4 pathway to increase the local concentration of CO_2. In these plants, phosphoenolpyruvate is first carboxylated into a four-carbon compound oxaloacetate, which undergoes further transformations and decarboxylation to release CO_2. The released CO_2 is then scavenged by Rubisco and drawn into the Calvin cycle with minimal photorespiration.[6]

1.1.3 Photosynthetic efficiency

Photosynthetic organisms have evolved highly efficient light-harvesting systems with quantum efficiency higher than 90%. This is achieved by peripheral antenna proteins that absorb light and funnel the excitation energy to the reaction centre chlorophylls.[10] Nevertheless, the overall photosynthetic efficiency* is surprisingly low: the highest efficiency measured under field conditions are 2.9% for C3 and 4.2% for C4 plants and typical efficiencies are 0.2%–1% for crop plants.[11,12] Several reasons are responsible for the low photosynthetic efficiency:[11,13] (1) As the pigments in photosystems and antennae are primarily sensitive to the visible light (λ = 400–700 nm), photosystems can only intercept 48.7% of the incident solar energy; (2) Light reflection and transmission due to weak absorption to green light (λ = 500–600 nm) cause at least 4.9% of energy loss;[10] (3) 6.6% of energy will be dissipated as heat during the transfer in antenna complexes, before reaching the red light-absorbing chlorophylls in reaction centres; (4) Energy expenditure associated with carbohydrate synthesis accounts for 24.6% and 28.7% for C3 and C4 plants, respectively; (5) Oxygenation and ensuing photorespiration cost extra 6.1% of energy in C3 plants; (6) Respiratory metabolism for maintenance and growth consumes minimum 1.9% (C3 plants) and 2.5% (C4 plants) of the entire energy input from solar irradiation. Summing all these energy losses, the maximal solar-to-biomass conversion efficiency is 4.6% for C3 plants and 6.0% for C4 plants (30 °C).[11,13]

1.2 Artificial photosynthesis

Natural photosynthesis inspires artificial endeavours to make fuels and chemicals from H_2O and CO_2 with solar energy. Artificial photosynthesis was first materialised by Fujishima and Honda who carried out the light-driven water splitting reaction in a PEC cell.[14] Following this paradigm, a diversity of solar water-splitting systems have been developed by coupling light absorbers (molecular dyes or semiconductors) and catalysts for hydrogen evolution re-

* The ratio between the energy in the biomass (combustion heat of glucose to CO_2(g) and H_2O(l) at 25 °C, 100 kPa) and energy input from solar irradiation (100 W cm^{-2}, AM 1.5G).

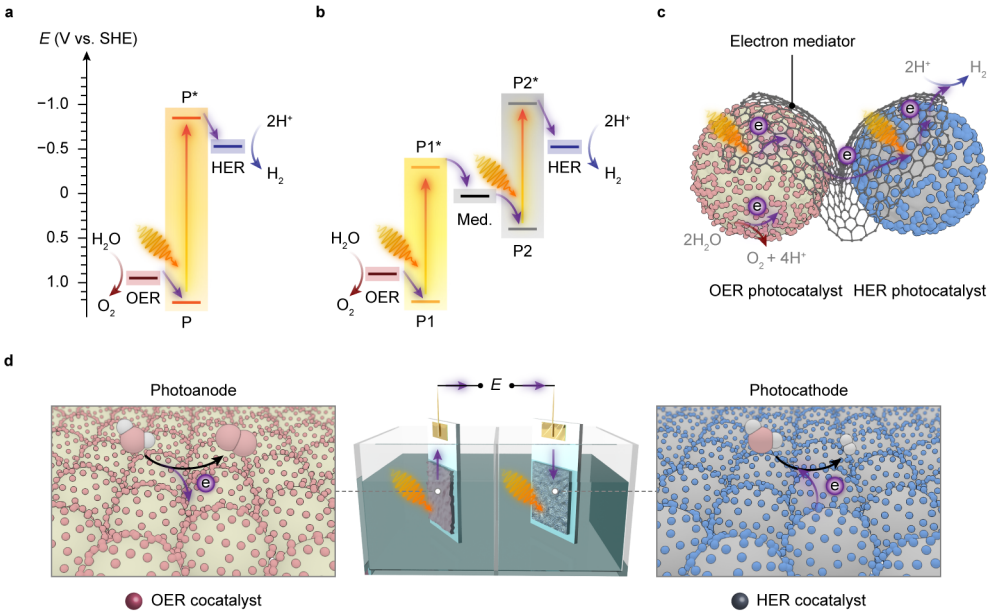

Figure 1.2 Chemical approaches to artificial photosynthesis. **a,b.** Energy level diagrams of light-driven water splitting: single-step excitation (**a**) and two-step excitation (**b**). P and P*: light absorber in ground and excited state, respectively. Med.: electron mediator. **c.** Representation of a two-step photocatalytic water-splitting system with semiconductor particles and HER and OER cocatalysts. The HER and OER photocatalysts are interfaced with a solid-state electron mediator. **d.** Representation of a PEC tandem water-splitting system. Photoanode and photocathode are semiconductors immobilised with OER and HER cocatalysts respectively.

action (HER) and oxygen evolution reaction (OER). Thermodynamics decides the suitability of light absorbers for autonomous solar water splitting from an energetic perspective. First, their energy band positions i.e., conduction and valence band edges*, should straddle the electrochemical potentials $E^{\circ}(H^{+}/H_2)$ and $E^{\circ}(O_2/H_2O)$ to confer charge carriers sufficient energy for HER and OER (**Figure 1.2a**). Second, the standard Gibbs energy of water splitting (237.1 kJ mol^{-1}) requires the band gaps of light absorbers greater than 1.23 eV (usually in the range of 1.6–2.4 eV to account for overpotentials).[15] Third, the thermodynamic redox potentials of light absorbers should be properly aligned with respect to their energy band positions to prevent themselves from photoinduced corrosion.[16]

Semiconductors whose electronic structures suffice for overall water splitting with visible light are limited, such as TaON, Ta_3N_5, CdS and CdSe.[17] However, these metal chalcogenides suffer from photodegradation as S^{2-} and Se^{2-} anions are oxidised by photogenerated

* For photoactive dye molecules, lowest unoccupied molecular orbital (LUMO) and highest occupied molecular orbital (HOMO) are used as the equivalent of conduction band edge and valence band edge of semiconductors, respectively.

holes.[18] Moreover, limited by the band gap of a single light absorber, only a small portion of visible light (usually λ<500 nm) can be harvested to produce charge carriers. An alternative strategy is to align the band position of two light absorbers and catalyse HER and OER respectively with electron mediators (**Figure 1.2b**),[19] which resembles the photosynthetic electron transfer ("Z-scheme") in the thylakoid membrane (**Figure 1.1b**). The two-step excitation system can expand the light absorption by harvesting low-energy photons,[20,21] and bring together materials that could merely drive either HER or OER.[22–24] Such tandem systems can enable larger driving forces for water splitting, and permit higher theoretical solar-to-hydrogen conversion efficiency than the single light-absorber systems.[25] Yet two light absorbers also multiply chances of charge recombination and pose challenges to control the kinetic balance of the electron transfer process.[3,21]

Artificial photosynthesis can be implemented in two manners: first, light absorbers are loaded with electrocatalysts and then suspended in a buffer solution in a photoreactor (**Figure 1.2c**);[26] The second manner is performed in a PEC cell where photocatalysts are immobilised on electrodes and photoinduced electrons flow across the external circuit (**Figure 1.2d**).[17] From a techno-economical viewpoint, the photocatalytic system is more advantageous, as PEC systems are required to achieve ∼25% solar-to-hydrogen conversion efficiency to rival with petrol in energy prices, primarily due to higher investment in installations, whereas efficiency of 5–10% would suffice to render photocatalytic reactors cost-competitive.[4,26] However, the highest solar-to-hydrogen conversion efficiency of particle-based systems is around 1%,[27] while that of electrode-based systems can typically achieve > 10%.[28,29] PEC systems also have several merits that are appealing for fundamental research and practical applications: (1) immobilisation of photocatalysts on electrodes enables detailed studies of half-reactions individually with or without sacrificial reagents and allows in situ probing photoredox chemistry through spectroscopic methodologies;[30–32] (2) from application's perspective, the electrode-based configuration enables separation of H_2 and O_2,[33] and can be transformed into a continuous fuel-production system where electrolyte streams past.[34] On the other side, drawbacks emerge: (1) preparation of photoelectrodes requires conductivity and high film-forming capability of semiconductors; (2) operation of PEC cell generates pH gradients that account for substantial potential loss and subject electrodes to increasingly corrosive environments;[35,36] (3) the high internal resistance usually necessitates external bias potential to drive the electron flow from photoanode to photocathode.

Artificial photosynthesis does not reproduce the reactions exactly happening in photoautotrophs, but exploits light absorbers and electrocatalysts to produce fuels and chemicals with earth-abundant feedstocks. Hydrogen is deemed as an ideal energy carrier to overcome the

intermittency of solar irradiation. Light-driven water splitting, either performed in particulate systems or PEC cells, has been under intense investigation over several decades. Yet it still faces challenges arising from the light harvesting, photocatalysts stability, interfacial charge transfer and the bottleneck water oxidation reaction.[37] The four-electron water oxidation to dioxygen involves multiple bond rearrangements and concerted proton release, and thus causes both thermodynamic uphill and kinetic sluggishness that confront the existing catalytic chemistry.[38] As a result, many solar water splitting systems expediently utilise sacrificial reagents like triethanolamine (TEOA) or ethylenediaminetetraacetic acid (EDTA) as the electron donor, which renders the whole system unsustainable.

Photocatalytic CO_2 reduction closes the loop of anthropogenic carbon cycle and offers a viable pathway for carbon fixation,[39] but it faces profound challenges: (1) Activating the linear CO_2 molecule for the ensuing endothermic reactions requires substantial energy input, which is reflected in the negative potential (-1.9 V vs. SHE, pH 7.0) during the formation of $CO_2^{\bullet -}$;[40–42] (2) The activation of CO_2 is followed by stepwise proton and/or electron transfer, which can yield miscellaneous products with poor selectivity;[39,43] (3) Due to the low solubility of CO_2 in water (0.033 mol L^{-1}, at 25 °C, 100 kPa),[40] the reduction of CO_2 usually competes with hydrogen evolution from H_2O that is kinetically more favourable, which further reduces the selectivity and solar-to-chemical conversion efficiency.[42] (4) The current solar CO_2 reduction systems cannot afford value-added multicarbon products that require high overpotential and controlled C–C formation, which undermines the economic incentives of this technique.

1.3 Semi-artificial photosynthesis

Artificial photosynthesis establishes solar-to-fuel pathways to address the global energy challenge, but it is bottlenecked by key-step reactions during the fuel-forming process. Biology is highly capable of tackling these synthetic challenges through naturally-refined biocatalytic machinery. Enzymes comprise only a handful of earth-abundant metal atoms as catalytic centres and cofactors, whereas the rest polypeptide chains set an ideal environment to control the access of reactants and carry out specific functions such as light harvesting, electron relay and proton transfers. Enzymes perfectly orchestrate the charge transfer, reactant delivery, bond formation and product removal at the active site, thereby reducing the energy threshold and expediting the reaction kinetics. In addition, enzymes widely employ steric hindrance and electrostatic or hydrogen bond interactions to stabilise selected intermediates and transition states, and therefore usher the reaction toward a single products.[44]

Whole microbial cells include biochemical pathways as an entirety and can produce hosts of metabolites of synthetic interest with high specificity at physiological conditions. Microorganisms wields numerous enzyme cascades that operate in concert to maintain intracellular metabolism. Different metabolic pathways are spatially ordered to divert metabolites or enzymes that can react promiscuously, so as to maintain selectivity, concentrate reactants to drive unfavourable reactions, and protect enzymes or unstable intermediates from harmful cytoplasmic contents.[45] Moreover, these biosynthetic pathways are under dynamic regulation to keep cellular functionalities in tune with physiological needs at different conditions. These features allow microbes to synthesise complex products from the simplest feedstocks (e.g., H_2O, CO_2, N_2, etc) and render microbial catalysis resilient to environmental perturbations.

Biocatalysts also have limitations. Enzymes are evolved to carry out specific biochemical reactions with fixed stoichiometry, and thus most enzymes are exclusive to non-natural substrates. In addition, the structure and functionality of enzymes cannot be readily engineered through conventional chemical methodologies, which constricts their applications for different reactions or in non-physiological conditions. On the other side, microorganisms rank their physiological needs to survive ahead of synthetic capacity to produce target chemicals. Carbon and electron fluxes in the metabolism are partially directed toward biomass synthesis for cell growth and maintenance, which reduces the pathway efficiency in chemical synthesis. Moreover, rerouting biochemical pathways toward desired products encounters resistance from the intracellular regulation, which renders such alteration problematic.[46,47]

Artificial photosynthesis, however, permits much more flexibility in system design and modification. Taking light harvesting as an example: most chlorophylls in nature have minimum absorption to green light (λ = 500–600 nm),[10] which partially accounts for the low photosynthetic efficiency, whereas in artificial photosynthesis, broadband absorption can be readily achieved with a variety of semiconductors and molecular dyes.[12] Furthermore, artificial systems allow coupling fuel-forming reduction reactions with useful chemical transformations. Several attempts already demonstrated that electrons could be withdrawn from biomass, organic compounds and even plastics to produce H_2 with versatile light-absorbing systems.[48–51] Artificial photosynthesis systems eliminate the dissipation of energy and electrons along the pathway, enabling high solar-to-fuel efficiency (>10%) routinely surpassing their natural counterparts.[28,52–54] Artificial photosynthesis is also empowered by an array of characteristic techniques such as electrochemistry, spectroscopy and in operando methodologies.[32,39,55] The well-defined features of synthetic materials permit systematic investigations to understand reaction mechanisms and establish structure-function relationships for system design and optimisation.[56]

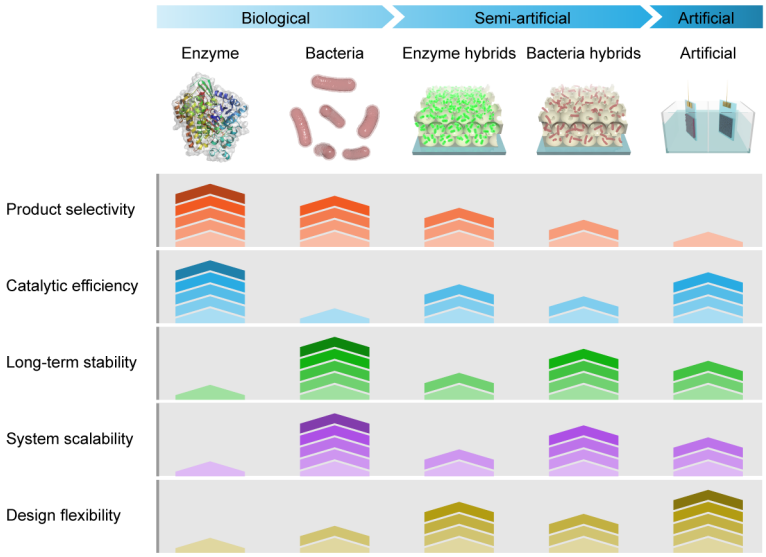

Figure 1.3 Comparison of catalytic systems spanning from natural to artificial regime. The strengths and limitations of each system are qualitatively evaluated in terms of product selectivity, catalytic efficiency, system stability, scalability and system variability by tuning its components.

Semi-artificial photosynthesis provides a hybrid approach for solar-to-chemical conversion, by integrating biocatalytic machinery (enzymes and microbes) with synthetic materials (dyes, electrocatalysts, semiconductors, electrodes, mediators) and analytic technologies.[57] The photosynthetic biohybrid systems seek to outsource tasks to the components that can perform the best and thus combine strengths of both while bypass limitations of each (**Figure 1.3**). In such hybrid systems, enzymes and microbes function as catalysts to drive synthetic reactions with thermodynamic uphill and/or chemical complexity, while synthetic materials act as substrates to immobilise biocatalysts and/or functional components that carry out light absorbing, electron transfer and chemical transformations etc. According to the forms of biocatalysts, semi-artificial photosynthesis falls into two categories—the enzymatic system and the microbial system, and each of these systems can be implemented either in a colloidal suspension or in an electrochemical cell (**Figure 1.4**).

1.4 Enzymatic hybrid systems

An enzymatic hybrid system employs separated electroactive or photoactive enzymes as electrocatalysts, light absorbers or electron conduits, to function in concert with synthetic components in driving reactions with high rates and yields (**Figure 1.4a,b**). Amongst a

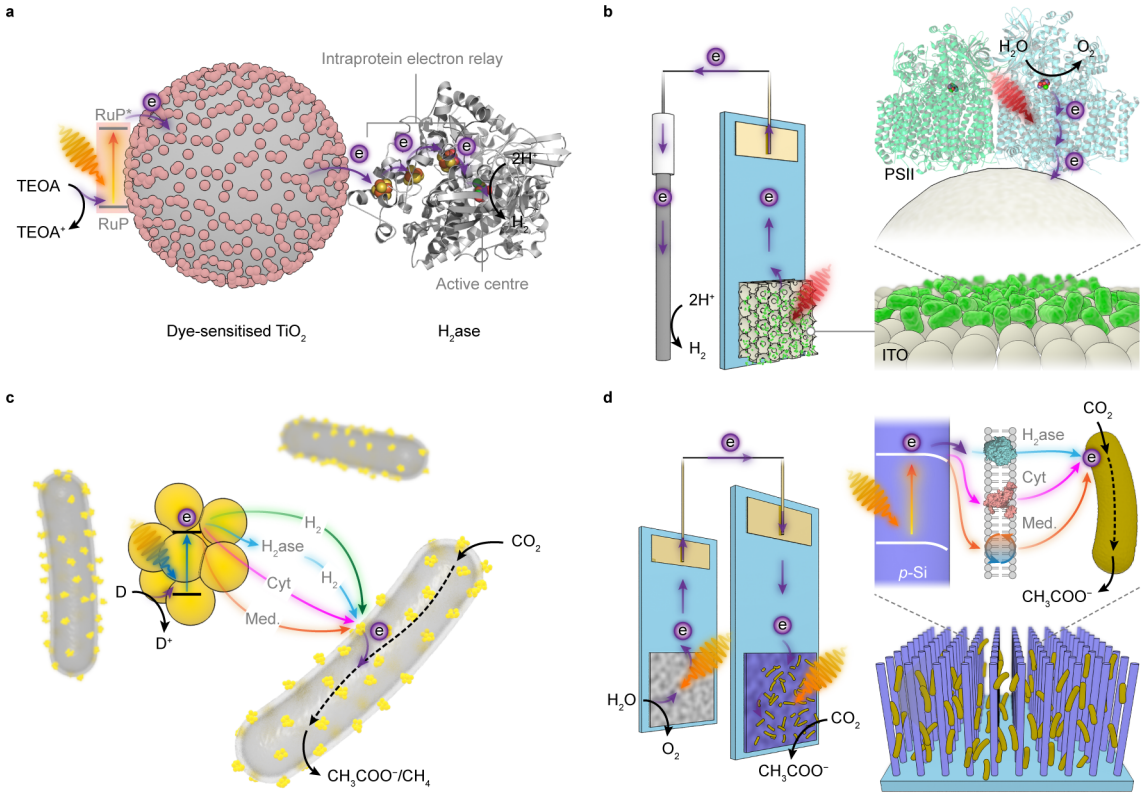

Figure 1.4 Representative semi-artificial photosynthesis systems. **a.** A colloidal system with dye-sensitised TiO_2 nanoparticles and hydrogenase (H_2ase) (Ref. [58]). **b.** An electrode system with a three-dimensional indium tin oxide (ITO) electrode and PSII (Ref. [59]). **c.** A colloidal system with CdS nanoparticles and CO_2-reducing bacteria *M. thermoacetica* (Ref. [60]). **d.** A hybrid tandem system with TiO_2 nanowires as the photoanode and Si nanowires integrated with acetogenic bacteria *S. ovata* as the photocathode (Ref. [61]).

myriad of enzymes available in nature, only a handful of them are of interest in synthetic reactions with the simplest feedstocks (e.g., H_2O, N_2 and CO_2). Translation of their catalytic prowess in vivo into synthetic power in vitro is confronted with profound challenges. Whereas synthetic catalysts are either integral parts of electrodes or discrete entities (particles or molecules), these redox enzymes are proteins with molecular weight of 10^4–10^6 and areal footprints of 100–400 nm^2. Their active sites (catalytic centres) are embedded within the protein matrices, which prevent indiscriminate reactions with substrate analogues, and also disallow direct exchange with exogenous electrons. Yet these enzymes have evolved intraprotein electron relays such as haems and [Fe-S] clusters that can carry electrons between active sites and electrodes.[62] The electron relays define vectorial electron transfer pathways within the protein and allow electrochemical suites to activate, monitor and modulate the enzymatic redox chemistry.[63] To approach the catalytic perfection, enzymes are expected

to accelerate the chemical reactions toward diffusion control.[64] As such, enzymes must engage with electrodes in an "electroactive" orientation to enable rapid electron transfer kinetics between the distal relay centre and electrode surfaces. In this regard, the enzyme-electrode interface must be rationally engineered with respect to topology, porosity and surface chemistry (hydrophilicity, surface charge, functional moieties, etc). From an energetic perspective, redox enzymes reduce the activation energy by electrostatic stabilisation,[65] and thus, minimise the electrochemical overpotential needed to drive a reaction.[44] This means that enzymes can catalyse redox reactions at or very close to their thermodynamic potentials and thus allow more light energy to carry out reactions that would otherwise not be affordable because of large overpotentials. The well-defined redox potentials can simplify system design by judiciously pairing with light absorbers and electron mediators according to their energy levels, and relieve synthetic challenges to seek materials with larger driving forces.

For example, Hydrogenases (H_2ases) are metalloenzymes that can catalyse the interconversion between H_2 and H^+ with a high TOF of >1000 s^{-1}.[66] The HER activity of H_2ases per active site is comparable with that of the benchmark Pt catalyst.[67] In view of the protein's large footprint and low active site density, H_2ases facilely surpass their synthetic counterparts with respect to atomic efficiency.[68] [NiFeSe]-H_2ase holds great promise as a model biocatalyst and has been rationally coupled with various light absorbers for photocatalytic HER. To this end, semiconductors were used as light absorbers and/or to immobilise H_2ases. Thus photogenerated electrons can stream directly from the conduction band toward the enzyme's distal relay centre. Coadsorbing [NiFeSe]-H_2ases on **RuP**-TiO_2 particles through the putative interaction between TiO_2 surface and side-chain carboxylates near the distal [Fe-S] cluster yielded 3.56 μM H_2 in the first hour of irradiation and a benchmark TOF_{H_2ase} of 50 s^{-1} (**Figure 1.4a**).[58,69] Enzymes such as PSII have also been immobilised on electrodes for PEC studies, which will be detailed later in this chapter (**Figure 1.4b**).[59,70]

1.5 Photoelectrochemical water oxidation with photosystem II

1.5.1 Structure and functionality of photosystem II

PSII is a 700 kDa transmembrane protein complex at the start of the photosynthetic chain, and is the only enzyme in nature catalysing the water oxidation reaction.[71,72] Every PSII

monomer contains dozens of protein subunits and cofactors including 35 chlorophylls and a Mn_4CaO_5 cluster, the oxygen evolution centre (OEC).[73] Two transmembrane subunits, D1 and D2, constitute the reaction centre complex of PSII and associate all cofactors involved in water oxidation and electron transfer. D1 and D2 subunits are flanked by two proteins, CP47 and CP43, which bind a host of chlorophylls for light absorption (**Figure 1.5a**).[74] A cyanobacterial PSII dimer has a geometric dimension of 205 Å × 110 Å × 105 Å.[75] In plants, the PSII core complex is usually surrounded with peripheral antenna light-harvesting complexes II to acclimatise to limited light, which renders the PSII supercomplex larger than its cyanobacterial counterpart.[76–78] Despite such differences, the structure and functionality of the PSII core complex are well-conserved amongst prokaryotic cyanobacteria, eukaryotic algae and higher plants during evolution.[79,80]

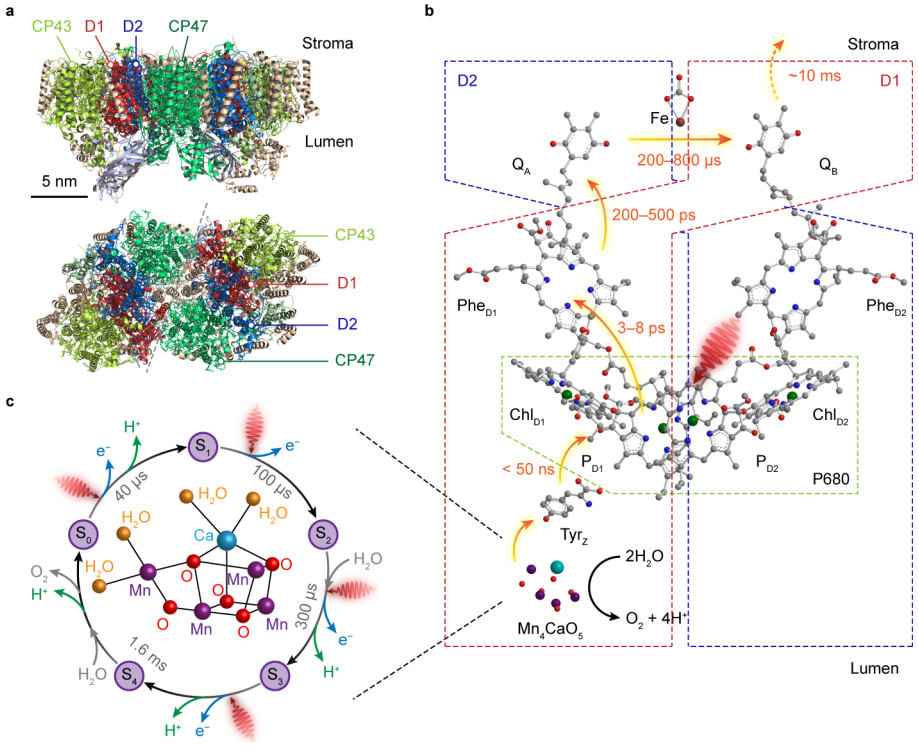

Figure 1.5 The structure and functionality of photosystem II. **a.** Protein structure of a PSII dimer from the side view and top view (Protein Data Bank ID: 4ub6). The main protein subunits (CP43, CP47, D1 and D2) are colourised. **b.** Schematic representation of the electron transfer pathways (indicated by the orange arrow) in the reaction centre complex of PSII. **c.** S_i states (i = 0–4) (Kok cycle) of the oxygen evolution at the Mn_4CaO_5 cluster.[81]

Antenna complexes in PSII harvest solar light and funnel the light energy to P680, where charge separation occurs within a few picoseconds.[82] This is followed by an electron transfer toward a pheophytin molecule (Phe_{D1}^-) and later to plastoquinone A (Q_A) (**Figure 1.5b**). The

resulting highly oxidising P_{D1}^{+} can extract an electron from a redox-active tyrosine Y_Z (Tyr_Z) and then provoke water oxidation at the Mn_4CaO_5 cluster.[82] On the stroma side, Q_A is tightly bound to the D2 protein and acts as a single-electron acceptor while Q_B in D1 protein can accept two electrons and be fully protonated. The electron transfer from Q_A to Q_B is aided by a non-haem iron midway between them.[79] The formed Q_BH_2 departs from the reaction centre and is replenished by the plastoquinone pool in the thylakoid membrane. The electron transfer is biased to the D1 side, and the symmetric cofactors (Chl_{D2} and Phe_{D2}) in the D2 protein are not functional.

High resolution structural analysis reveals that the core of the Mn_4CaO_5 cluster is a distorted cubane, where three manganese, one calcium and four oxygen atoms occupy vertices (**Figure 1.5c**).[71,73,74] The fourth manganese and the fifth oxygen are located outside of the cubane, forming a distorted chair with the cubane as the chair base and the isolated manganese and oxygen atoms as the chair back. Such structure allows the Mn_4CaO_5 cluster to perform structural rearrangements needed for catalysing the water oxidation.[74].

The consensual mechanistic model of O_2 evolution at the Mn_4Ca_5O cluster is known as Kok cycle. In this model, the OEC undergoes four intermediate redox states (S_i states, i = 0–4) to liberate one O_2 and four protons from two H_2O molecules (**Figure 1.5c**).[81,83–85] The four-electron oxygen evolution at the Mn_4CaO_5 cluster is synchronised with the one-electron photochemistry at the reaction centre by the the Tyr_Z. Each photon captured by P680 yields a $Tyr_Z^{\bullet+}$, which extracts an electron from the OEC and drives the stepwise transition of S_i states. Summing the halflife of S_i states ($t_{1/2} \approx 2$ ms), the turnover frequency (TOF) of the Mn_4CaO_5 cluster is estimated as 500 s^{-1}, which outpaces most molecular catalysts (typical TOF: 10^{-3}–10 s^{-1}) in driving water oxidation.[86] In spite of this, the measured oxygen evolution rate of isolated PSII is in the range of 2,000–5,000 $\mu mol_{O_2}\, mg_{Chl}^{-1} h^{-1}$, corresponding to a TOF of 18–43 s^{-1}.[87–90] This large discrepancy stems from the intraprotein electron relay where the downstream electron transfer from Q_A to Q_B ($t_{1/2}$ = 200–800 µs) and the release of Q_BH_2 ($t_{1/2} \approx 10$ ms) are the rate-determining steps.[91]

Apart from being an energy source, sunlight also causes damage to PSII, thereby inhibiting photosynthetic activity. Phototrophic organisms have developed protective mechanisms to reduce the light-induced damage and rapidly repair the photodamaged PSII. Photoinhibition will occur when the photodamage overrides repair.[92,93] The photodamage to PSII involves a consecutive two-step process: first, UV and/or blue light disrupts the Mn_4CaO_5 cluster, interrupting the electron supply to quench the excited chlorophylls. The accumulated $P680^+$ then impairs the photochemical reaction centre by attacking the surrounding amino acid residues mainly in the D1 subunit.[94,95] Second, sunlight also generates harmful reactive oxygen

species (ROS) such as $O_2^{\bullet -}$, H_2O_2 and $^{\bullet}OH$ due to the electron transfer from redox-active cofactors to O_2, and singlet-state $^1O_2$ from energy transfer from triplet-state chlorophyll to $^3O_2$.[96–98]

1.5.2 Photoelectrochemistry of photosystem II

For artificial photosynthesis, whereas water is the ideal terminal electron source to feed the downstream fuel-forming reactions, few electrocatalysts can handle this multielectron process in an orderly and efficient manner, which is further complicated by the coordination with light absorbers. PSII, however, respectively assigns the tasks of light harvesting and water oxidation to antenna proteins and the Mn_4CaO_5 cluster, and orchestrates photochemistry in concert with catalysis in a stepwise manner via efficient intraprotein electron relays. Therefore, PSII is a model biological OER catalyst that inspires synthetic endeavour to mimic its core components,[99–101] and stimulates mechanistic investigations to understand its functionality.[98,102] Wiring PSII with an electrode allows the resulting biohybrid electrode to supply photoelectrons from water for synthetic reactions, and permits protein film-photoelectrochemistry (PF-PEC) to benchmark enzymatic activity in vitro, dissect photoinduced electron transfer pathways, and repurpose biogenic electrons to drive unnatural endergonic reactions.[103]

Attempts to interface PSII with an electrode surface started three decades ago,[104] when isolated PSII was deposited on a Pt electrode and generated a photocurrent of few microamperes as a result of water oxidation. However, the minuscule amount of PSII loaded on the electrode renders in-depth studies and applications untenable. Underlying PSII-PEC is the electrode that provides a physical scaffold to immobilise enzymes and an artificial electron acceptor to biogenic electrons. PSII's photochemistry and the ensuing current output can be greatly influenced by the material, structure and physical property of the electrode scaffold, which dictates the strength of protein binding, the capacity of protein loading, the accessibility to intraprotein electron relays, the depth of light penetration, and the transport of reactants and products therein.[105] The trajectory of intraprotein electron relay makes the interfacial electron transfer highly dependent on the protein orientation. Q_B, the terminal electron acceptor in PSII, can only undertake outward electron transfer if the stromal side of PSII is proximal to an electrode surface (**Figure 1.6a**). The electron transfer via intrinsic plastoquinones, namely, direct electron transfer (DET) can be registered as anodic photocurrent by chronoamperometry under irradiation, and verified by the addition of 3-(3,4-dichlorophenyl)-1,1-dimethylurea (DCMU) that inhibits the Q_B site and interrupts the electron flow from Q_A.[106] DET often results in relatively low photocurrent because

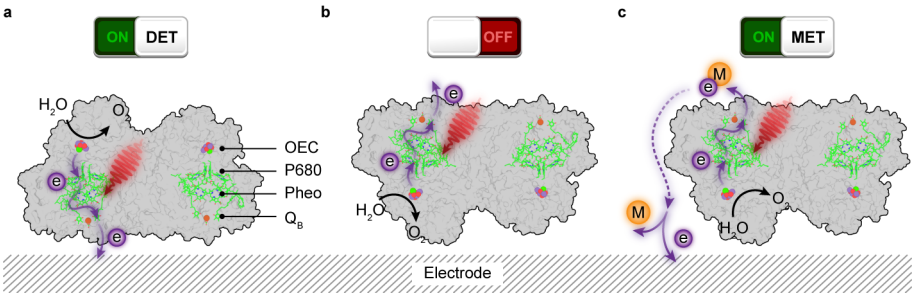

Figure 1.6 Electron transfer at the PSII-electrode interface. Electron transfer can only take place provided that the stromal side of PSII intimately interfaces with the electrode (electroactive orientation, **a**). PSII cannot donate electrons to external acceptors in other orientations (**b**) unless there are diffusional redox couples that can mediate electrons between Q_B and electrodes (**c**).

most PSII are adsorbed in an unfavourable orientation or remote from the electrode surface (**Figure 1.6b**). This problem can be mitigated by using diffusional mediators such as DCBQ to shuttle electrons from Q_B site to electrodes (**Figure 1.6c**). Yet the termed mediated electron transfer (MET) comes at an expense in both energetics and kinetics, as extra energy is needed to drive the redox turnover of electron mediators and the diffusion of mediators is likely to govern the overall rate of electron transfer.

From both fundamental and practical viewpoints, an electrode with a large number of proteins being wired in an electroactive way is highly desired to produce high photocurrent that can afford reliable analysis and viable applications (**Figure 1.7a**).[103] The making of such electrodes enables new possibilities to create solar-to-fuel pathways unattainable in biology. The chronology of the electrode design will be outlined below.

In the nascent stage of PSII-PEC, PSII with a polyhistidine tag (His-tag) at its stromal side was immobilised on flat Au electrodes by a self-assembled monolayer (**Figure 1.7b**).[88,107–109] The interaction between nickel-nitrilotriacetic acid chelators and His-tags allowed for site-selective binding of PSII on Au electrodes. However, the flatness of the electrode surface limited the protein loading typically below 10 pmol cm^{-2} and thus resulted in submicroampere photocurrents.[88] The problems can be alleviated by the use of redox polymer matrix that provides a solvated environment to electrically wire a high amount of proteins and enables redox centres on the polymer backbone to access intraprotein electron relays, regardless of their orientation and distance (**Figure 1.7c**).[110] A polymer grafted with Os^{2+}/Os^{3+} redox couple ($E_{1/2} = 0.39$ V vs. SHE) was employed as both an immobilisation matrix and an electron mediator to PSII, which gave rise to a benchmark photocurrent density up to 45 μA cm^{-2}.[111] The second generation of electrodes are mesoporous films made with metal

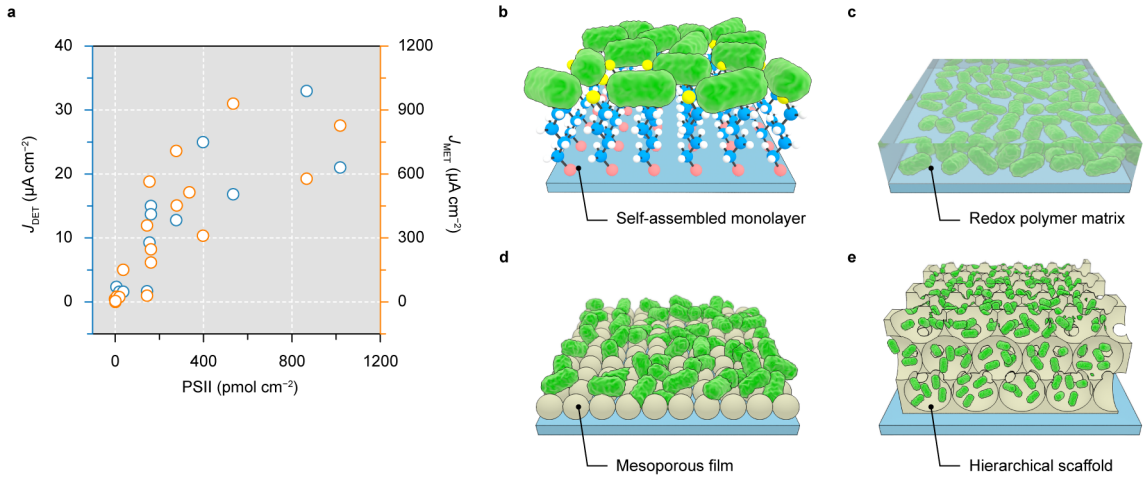

Figure 1.7 Synthetic electrodes to wire PSII for semi-artificial photosynthesis. **a.** Correlation between protein loading in electrodes and the resulting photocurrent by DET (blue dots) and MET (orange dots). **b–e.** PSII wired to an electrode via a self-assembled monolayer (**b**), a redox-polymer matrix (**c**), a mesoporous film with nanoparticles (**d**) and a three-dimensional hierarchical scaffold (**e**).

oxides such as Fe_2O_3, TiO_2 and ITO.[112–117] A mesoporous ITO (meso-ITO) film have a thickness of 3 μm and a pore size up to 100 nm,[116–119] which suites the dimension of PSII (10 nm×10 nm×20 nm) (**Figure 1.7d**). The meso-ITO afforded a PSII loading density of 19 pmol cm^{-2} and a mediated photocurrent of 22 μA cm^{-2}*.[116] In addition, the surface chemistry of ITO can be readily modified so as to covalently bind PSII in favour of an electroactive orientation.[117] The meso-ITO film can also be deposited onto a rotating ring disk electrode as a key part of an apparatus to study the oxygenic photoreactivity in PSII (Section 1.8).[98]

The state-of-art electrodes for PSII-PEC feature a hierarchical inverse opal structure with both macroporosity and mesoporosity (**Figure 1.7e**).[59,70,120–125] Such architecture has interconnected macropores that provide large surface area accessible by protein diffusion. On the skeleton is a mesoporous surface consisting of conducting and hydrophilic nanoparticles (ITO or TiO_2) where proteins are adsorbed. The inverse opal electrodes are fabricated via a coassembly method using polystyrene beads as the structural template and ITO or TiO_2 nanoparticles as the electrode material. Such method makes electrode structure easily tunable in accordance with biocatalysts with different dimensions.[126,127] The hierarchical structure also benefits both mass transport and light transmission, and permits high PSII loading in the

*Conditions: *Thermosynechococcus elongatus* PSII on an IO-ITO photoanode (0.25 cm^2), 0.5 mM DCBQ, 40 mM MES, 15 mM $CaCl_2$, 15 mM $MgCl_2$, 50 mM KCl, 5% glycerol, pH 6.5, 25 °C, $E = 0.5$ V vs. SHE, 8 mW cm^{-2}, $\lambda = 635$ nm

range of 30–1000 pmol cm^{-2} (depend on thickness).[59,120,121] A 40 µm IO-ITO electrode attained a high photocurrent of 17 µA cm^{-2} out of DET and 930 µA cm^{-2} with the presence of DCBQ mediators*.[59] Os-based polymers can further be incorporated to the IO-ITO scaffold to improve the electrical wiring and eliminate the use of diffusional additives.[70] Compared with flat electrodes,[111] the IO-ITO electrode with the polymer matrix achieved higher photocurrent of 381 µA cm^{-2} due to higher PSII (336 pmol cm^{-2}) loading.[70] The high photocurrent allowed for reliable O_2 quantification to calculate the Faraday efficiency, which was not possible with flat electrodes.[59,70] Such electrode also underpinned PF-PEC to dissect electron transfer pathways at the enzyme-electrode interface. A competing pathway stemming from the photoinduced O_2 reduction has been identified to account for the monitored cathodic current at < 0.2 v vs. SHE.[96] The electrochemical window of ITO (−0.6–2 V vs. SHE, pH 7.0) limits its application at negative potentials needed to drive reducing reactions.[128] In view of this, ITO can be substituted with semiconductive TiO_2 to fabricate similar IO-scaffolds that are applicable under cathodic conditions.[129] Moreover, the IO-TiO_2 electrode allowed for additional dye-sensitisation to complement the limited light absorption of PSII in the visible spectrum and provide sufficient driving force to carry out proton and CO_2 reduction.[120,121] However, the intrinsic fragility of PSII under light irradiation limited the longevity of the photocurrent ($\tau_{1/2} < 10$ min) and rendered the downstream synthesis unfeasible.[103]

In contrast to the rapid development of electrodes, our understanding into the enzyme-electrode interaction is advancing slowly. How many enzymes are loaded onto an electrode? How does the enzyme loading relate to the electrode porosity? How do enzymes interact with electrode surfaces? How do they distribute within the electrode scaffold? What are factors governing the catalytic activity of enzymes inside an electrode? These are key questions to understand the enzyme-electrode interface, which also provide clues to optimise the biohybrid systems for better catalytic performance. Using PSII as a model biocatalyst, this thesis adopts a multidisciplinary approach combining conventional PF-PEC with an orthogonal set of techniques to deliver insightful answers and to draw a clearer picture of PSII-ITO biohybrid systems.

*Conditions: 535 pmol cm^{-2} *Thermosynechococcus elongatus* PSII on an IO-ITO photoanode (0.25 cm^2, pore size: 750 nm, thickness: 40 µm), 1 mM DCBQ, 40 mM MES, 20 mM $CaCl_2$, 15 mM $MgCl_2$, 50 mM KCl, 5% glycerol, pH 6.5, 25 °C, in air, $E = 0.5$ V vs. SHE, 10 mW cm^{-2}, $\lambda = 660$ nm

1.6 Microbial hybrid systems

Compared with enzymatic counterparts, the microbial hybrid system is still in its infancy but has provoked increasing interest in solar-to-chemical conversion, due to their synthetic complexity, better stability and prospects for scalability.[130] Recently, CdS nanoparticles were interfaced with *Moorella thermoacetica* (*M. thermoacetica*), an acetogenic and electrotrophic bacterium, by in situ deposition (**Figure 1.4c**). *M. thermoacetica* could directly use photogenerated electrons from the excited CdS to reduce CO_2 into acetate via the intracellular Wood-Ljungdahl pathway, while holes produced by CdS were quenched by electron donors.[60] Likewise, CdS nanoparticles were deposited on the surface of the *Methanosarcina barkeri*, a methanogenic bacterium, for photoinduced CO_2 reduction to CH_4.[131]

There are few attempts to directly interface microorganisms with photoelectrodes. The difficulty is due in part to the large footprint of cells, which requires appropriate electrode geometry to achieve a high loading density while maintain the light penetration. A notable example is an array of Si nanowires that served both as a light-absorbing semiconductor and a physical scaffold for the acetogenic bacterium, *Sporomusa ovata* (**Figure 1.4d**).[61] The bacteria were electrochemically integrated with the Si nanowires by taking electrons from its conduction band to sustain metabolism. The resulting biohybrid electrode was assembled with a photoanode made of TiO_2 nanowires for autonomous photoreduction of CO_2 to acetate. The PEC cell produced a stable photocurrent of 0.3 mA cm^{-2} for more than 120 h, yielding an acetate titre of 20 mM and Faraday efficiency of 86%. Acetate could further be activated into acetyl-coA, a common biochemical intermediate, to access a variety of biosynthetic fine chemicals. The downstream synthesis could be performed by genetically-engineered *E. coli* that transformed acetate into *n*-butanol, polyhydroxybutyrate polymer, and isoprenoid compounds.[61]

1.7 Electrochemistry with electroactive bacteria

1.7.1 Electroactive bacteria

Geobacter and *Shewanella* are Gram-negative dissimilatory metal-reducing bacteria ubiquitously thriving in subsurface and aquatic sediments and play an important biogeochemical role in cycling metals and organics in nature. The hallmark feature of *Geobacter* is their ability to anaerobically oxidise organic compounds into CO_2 while reduce insoluble Fe(III) and Mn(IV) oxides via outer membrane cytochromes and conductive bacterial nanowires.[132]

Geobacter is the most abundant Fe(III)-reducing microorganisms on earth, and is so far the most current-producing bacteria and the dominant species in microbial electrochemical systems.[132,133] All *Geobacter* species can use acetate to assimilate carbon and conserve energy for growth via the tricarboxylic acid (TCA) cycle.[134,135] Besides acetate, certain *Geobacter* species can use a variety of substances such as formate, lactate, aromatics, alcohols and hydrogen as electron donors.[132,136,137] For example, *G. sulfurreducens* can oxidise formate and lactate with Fe(III) as terminal electron acceptors by deploying different metabolic routes.[137] *Geobacter* species can also use different electron acceptors for their anaerobic respiration, including soluble nitrate, fumarate, metal ions and insoluble Fe(III) and Mn(IV) oxides.[132] They can reduce soluble U(VI) and Cr(VI) into less soluble U(IV) and Cr(III), which allows for bioremediation of wastewater containing heavy metals.[138,139] Their ability to indiscriminately interact with various electron acceptors endows themselves with native compatibility to inorganics, and by analogy, to synthetic electrodes for microbial electrochemistry.[140]

Shewanella genus welds the most diverse respiratory pathways to survive in both oxic and aoxic environments.[141] They can use a wide range of organic and inorganic compounds as electron acceptors including Fe(III) and Mn(IV) oxides, nitrate, dimethylsulfoxide, sulfite, thiosulfate and elemental sulfur.[142] Their metabolic versatility promises great potential in bioremediation of environmental pollutants. *Shewanella* usually produces less current than *Geobacter*, therefore *Shewanella* is less employed in microbial fuel cells.[143]

Besides producing electrons, *G. sulfurreducens* was found able to receive electrons from graphite electrodes to reduce fumarate into succinate,[144] which promises its applications in bioremediation. *G. sulfurreducens* has been employed to decontaminate the U(VI)-containing wastewater with electrons supplied by a graphite electrode.[145] By this means, soluble U(VI) was biotically reduced into insoluble U(IV) and immobilised on the electrode.

1.7.2 Extracellular electron transfer

The cell envelop is neither physically permeable to minerals nor electrically conductive, *Geobacter* and *Shewanella* therefore have developed various extracellular electron transfer (EET) mechanisms to fulfil their survival needs.[146] By coupling intracellular metabolism with extracellular redox transformations, EET creates opportunities to leverage the microbial metabolism for sustainable energy production and chemical synthesis. Despite a phylogenetic diversity, EET can happen via three pathways: *c*-type cytochromes (cyt *c*), conductive bacterial nanowires and self-excreted electron shuttles.[147]

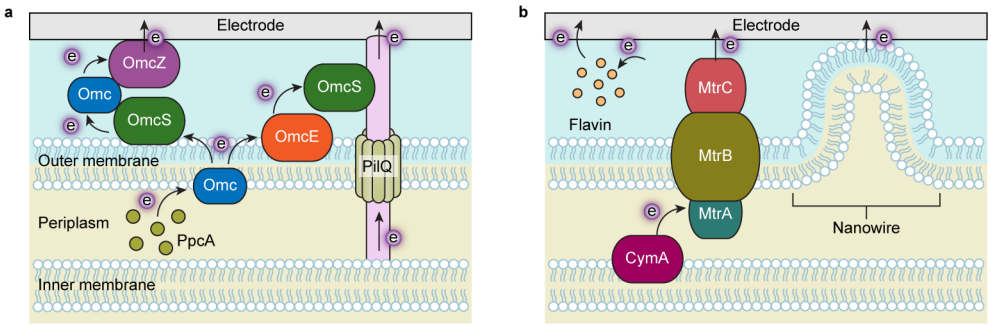

Figure 1.8 Microbial extracellular electron transfer pathways. **a.** In *Geobacter*, metabolic electrons are transferred across the cellular membrane via outer membrane cytochromes and conductive pili. **b.** In *Shewanella*, metabolic electrons are transferred via cytochromes, conductive nanowires and self-excreted flavins.

Cyt *c* contains haems that comprise porphyrin rings and iron atoms and function as the electron transfer centre. Genome analysis revealed that *Geobacter sulfurreducens* (*G. sulfurreducens*) has 111 genes encoding cytochromes distributed in inner membrane, periplasm and outer membrane.[148] Outer membrane cytochromes including OmcB, OmcE, OmcS and OmcZ along with a periplasmic cytochrome PpcA have been identified underlying the EET in *Geobacter* (**Figure 1.8a**).[147] PpcA acts as an intermediary electron carrier between cytoplasmic electron donors and extracellular electron acceptors.[149] OmcZ is thought essential for current production and long-distance electron transfer in biofilms.[150] The physiological functionality of other cytochromes remains elusive.[146] The genome sequencing revealed 39 cytochromes in *Shewanella oneidensis* (*S. oneidensis*).[142] CymA is an inner-membrane-bound tetrahaem cytochrome vital for *Shewanella* EET. It functions as the major electron conduit across the periplasm by directly interacting with periplasmic redox proteins (**Figure 1.8b**).[151] Metal-reducing proteins MtrA, MtrB and MtrC assemble into a complex that carries electrons across the ~40 Å outer membrane, and is the best-understood pathway for microbial EET.[152–154]

Both *Geobacter* and *Shewanella* can grow conductive pili termed"bacterial nanowires" in response to a deficiency of electron acceptors nearby (**Figure 1.8**).[155,156] The conductive nanowires allow bacteria to access electron acceptors several micrometres away, and thus are evolutionarily meaningful for them to survive in subsurface environments where metal oxides are heterogeneously dispersed. *Geobacter* nanowires are assembled by micrometer-long polymerization of the hexaheme cytochrome OmcS, with haems packed within ~3.5–6 Å of each other.[157] Distinct from *Geobacter*, *Shewanella* nanowires are extensions of the outer membrane and periplasm, which contain the redox-active multihaem cytochromes

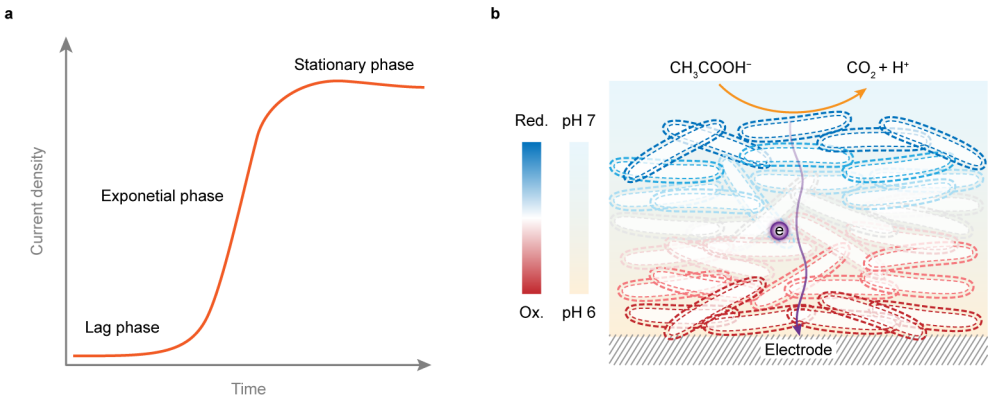

Figure 1.9 The formation of biofilm during anodic growth. **a.** Typical anodic current of microbial growth on an electrode. **b.** The redox and pH gradients (indicated by the colour bars) inside a biofilm on an electrode.

(MtrA, MtrC, OmcA etc),and allow electrons to transport via a multistep redox hopping mechanism.[158,159]

Besides the direct electron transfer via outer membrane cytochromes and bacterial nanowires, *Shewanella*, but not *Geobacter* can also secretes flavins, mainly riboflavin and flavin mononucleotide, to shuttle electrons. The mediated electron transfer accounts for more than 70% of the EET capacity.[160–162] Whereas the ATP cost for synthesising flavins is less than 0.1%, the EET kinetics is governed by the diffusion of electron shuttles, rendering *Shewanella* less efficient in current production.[160,163]

1.7.3 Microbial electrogenesis

Some microorganisms can generate electrical current has been known for more than a century.[164] Renewed interest in this phenomenon, termed microbial electrogenesis, stimulates continuous research in microbial fuel cells to harness the power of microbial metabolism for electricity production or wastewater treatment.[146,165] Microbial electrogenesis is undertaken by electrogenic microorganisms that can discharge respiratory electrons to an anode by EET.[154] Here, I outline the current understanding of the assembly of biofilms on electrodes and electron transfer mechanisms with primary focus on *G. sulfurreducens*.

The development of a biofilm on an electrode undergoes three phases, namely lag phase, exponential phase and stationary phase, which is registered as anodic current by chronoamperometry (**Figure 1.9a**). During the lag phase, planktonic cells land on the electrode surface and laterally proliferate into a monolayer biofilm with little current output. The current begins to increase exponentially when the biofilm thickens and cyt *c* accumulates

locally.[166] The mechanisms of intrabiofilm electron transfer still lack consensus due to the unresolved contention between the metallic-like conductivity and redox conductivity (electron superexchange).[167–171] The superexchange mechanism is progressively attested by the mounting experimental evidence.[172–174] Within this framework, the following discussion will depict how electrons traverse the biofilm with dozens of micrometre thickness and pinpoint factors limiting the biofilm growth and maximum current density.[175,176]

The *Geobacter* biofilm conduction stems from multistep electron hopping mainly through multihaem cyt *c*, which is driven by the redox gradient arising from the disparity in local oxidation states of the biofilm far from and close to the anode surface (the local electron concentration is higher farther from the anode surface) (**Figure 1.9b**).[172,175] Such scheme also partly accounts for the upper limit of the thickness of anode-grown biofilms. At a certain distance away from the electrode surface, local concentration of oxidised cytochromes in the biofilm becomes too low to accept electrons, thereby inhibiting additional growth beyond the existing thickness.[175,177] The other limiting factor is the pH gradient. The anode respiration of one acetate molecule entails a stoichiometric production of eight protons. Inefficient proton dissipation incurs pH gradient in the biofilm, where the local pH near the anode surface could decrease to 6.1 from neutrality (**Figure 1.9b**).[178] The local acidification suppresses the metabolic activity of microbes, positively shifts the redox potentials of cytochromes, and in consequence, hinders the continual growth of biofilm and its current production.[175] Despite these gradients, it has been demonstrated that microbes throughout the biofilm are active in metabolism and able to release electrons, regardless of their spatial locations.[179] In enzymatic hybrids, efficient intraprotein electron relays render the protein-material interface rate-limiting, whereas biofilm voltammetry analysis concludes that the anodic current is largely governed by the intrabiofilm electron transport via redox cofactors.[176,180,181] Reactant diffusion within the biofilm, microbial metabolism with acetate and electron transfer across the microbe-electrode interface are not likely to account for the finite current.[180]

1.7.4 Microbial (photo)electrosynthesis

Microbial (photo)electrosynthesis is carried out in a biohybrid system where microorganisms are immobilised on electrodes to catalyse redox reactions driven by light or electricity (**Figure 1.10a**). Underlying this process is the electron uptake ability of microorganisms from the interfacing electrode (**Figure 1.10b–d**).[182] This can happen directly between the electrode and microorganisms and also be mediated by H_2 or diffusional redox couples. The direct electron transfer is the preferred means for microbial electrosynthesis, as it bypasses the handicap of low solubility of H_2 and the diffusional limitations of electron shuttles. Besides,

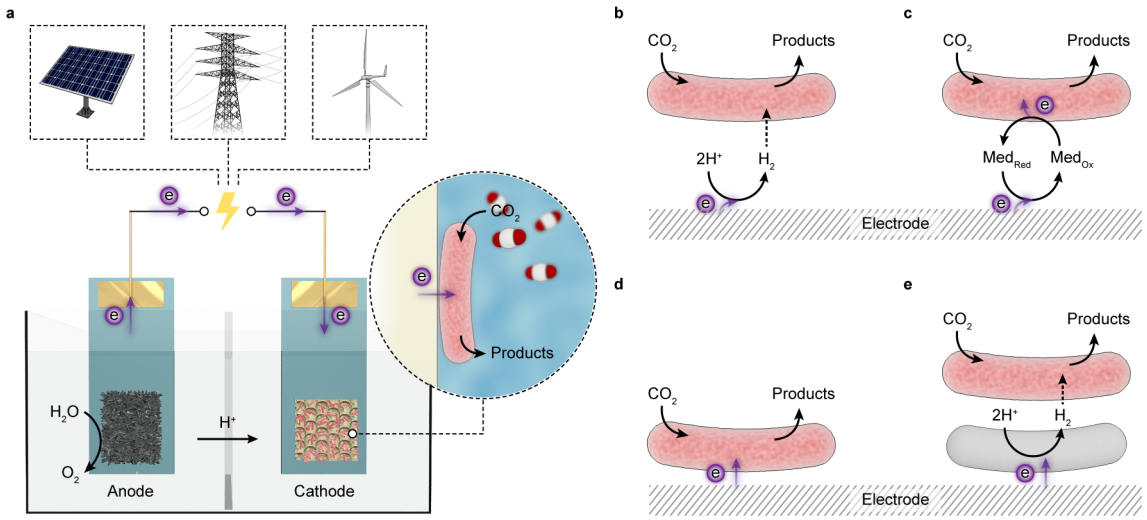

Figure 1.10 Microbial electrosynthesis. **a.** Schematic representation of a microbial electrosynthetic cell powered with electricity that can be derived from renewable sources (solar light, wind, et al). PEM: proton exchange membrane. At the anode chamber, an electrode donor (e.g., H_2O) is oxidised, providing electrons that are later energised by the energy input. At the cathode chamber is a microbial hybrid electrode where microorganisms receive electrons from the interfacing electrode scaffold and drive the reduction reaction (e.g. CO_2 reduction). **b–e.** Mechanisms for electron transfer from electrodes to microorganisms. Electrons from the electrode can be delivered to the microorganisms by H_2 (**b**), redox mediators (Med_{Red}/Med_{Ox}, **c**), direct electron transfer (**d**) or interspecies hydrogen transfer (**e**).

it avoids the high overpotential necessary to generate H_2 at poorly catalytic electrodes and the potential toxicity of some mediators (e.g., methyl viologen).[183] As electricity can be finally derived from solar light by photovoltaic devices, one can readily and flexibly extrapolate the application of the microbe-electrode hybrid to photosynthesis, either by pairing with a photoelectrode in a PEC cell or connecting with a solar cell for photovoltaic electrolysis.

Few light-absorbing semiconductors have been optimised to fit the dimension of microorganisms. Integration of microbes into the electrode scaffold also poses challenges on the chemical stability, biocompatibility, conductivity and surface chemistry of the semiconducting materials, not least the impact on light transmission. A more favoured strategy is to immobilise microorganisms on electrodes with tailored morphologies while outsource light harvesting to photoanodes or photovoltaics in tandem systems. Such way decouples photochemistry with microbial metabolism, and thereby suppresses unwanted parasitic reactions and eliminates possible oxidative stresses stemming from photoinduced ROS. The simplified design also grants more flexibility in the making of electrode architectures to enhance the loading capacity and engineer the electrode surface to improve the interaction. Therefore, more efforts converge on interfacing microbial cells with tailored electrodes and improving

the interfacial electron transfer and mass transport. Such exploitation can capitalise on decades of research in microbial fuel cells,[184] and be guided by recent understandings of the interaction between synthetic materials and microorganisms.[185]

The first report appeared in 2004 when graphite electrodes were employed to feed *G. sulfurreducens* with electrons for fumarate reduction.[144] The H_2-mediated electron transfer was ruled out because the electrode barely produced H_2 at the applied potential (0.3 V vs. SHE, pH 6.8). Instead, *G. sulfurreducens* directly received electrons from the electrode through a separate pathway other than its outward extracellular electron transfer.[186] The same reaction could also be accomplished by *S. oneidensis* cultured on a graphite electrode or in a three-dimensional reduced graphene oxide (RGO) scaffold.[187,188] But distinct from *G. sulfurreducens* is that exogenously-supplied electrons were routed reversibly via the outer membrane protein complex (MtrCAB) to the cell and engaged with cytoplasmic fumarate reductase through CymA and menaquinone pool.[187] An envisioned application for microbial electrosynthesis is bioremediation, namely, decontaminating the wastewater possibly powered by solar energy.[165] For example, under applied negative potentials, *G. sulfurreducens* could precipitate soluble U(VI) ions on electrodes, which can be easily collected.[145] Bacteria such as *G. lovleyi* and *Anaeromyxobacter dehalogenans* with the ability to respire with chlorinated compounds can also be exploited to dechlorinate contaminants (e.g., tetrachloroethene, 2-chlorophenol) in this manner.[189,190]

1.7.5 Electrode architectures for microbial electrochemistry

Electrodes underlie the operation of microbial fuel cells in several ways: they intimately interface with electrogenic microorganisms and collect electrons discharged from microbial metabolism. Also, they provide a biocompatible scaffold for microbial proliferation and during the course, ensure effective delivery of feedstock and dissipation of products. As such, the chemical components, scaffold structure, as well as surface topology and chemistry of electrodes, will fundamentally influence the physical interaction and electrical interplay at microorganism-material interfaces.[140,185] The early studies used carbon-based electrodes such as graphite and carbon cloth (**Figure 1.11a,b**), which are conductive, electrochemically stable, biocompatible and inexpensive.[144,199,200] The later use of carbon nanomaterials, e.g., carbon nanotubes and graphene, introduced more topological features on the electrode surface, and thereby created larger surface area accessible to microorganisms.[201–204] Metals like copper, silver and stainless steel can also serve as microbial electrodes.[205] The main advantage of metal electrodes is their exceptionally high conductivity (10^6–10^7 S m^{-1}) that is several orders of magnitude higher than that of carbonaceous counterparts. Yet their drawbacks arise

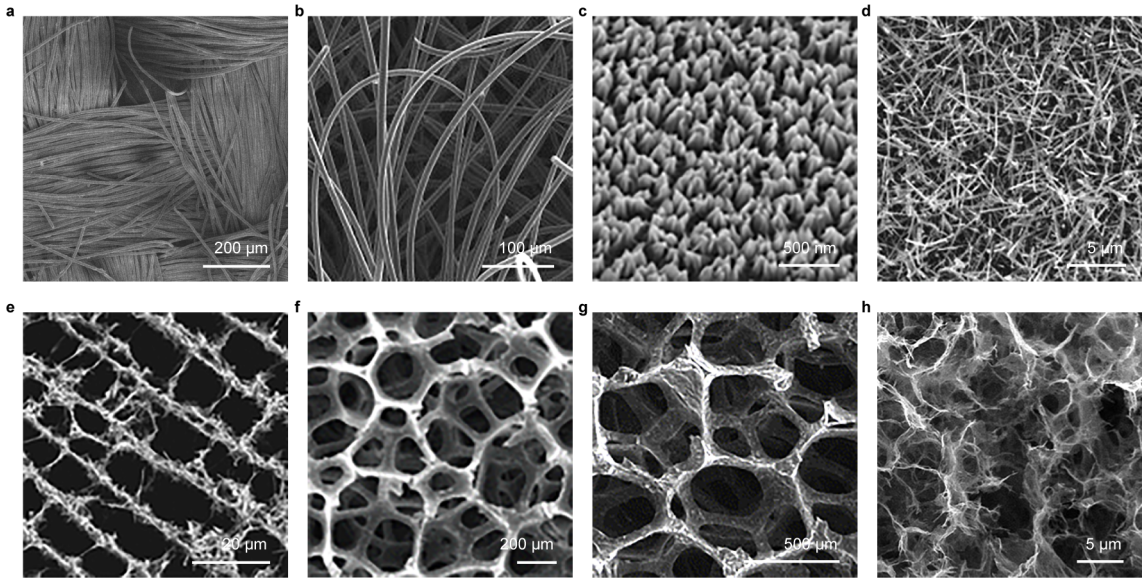

Figure 1.11 Representative electrode scaffolds employed in microbial fuel cells. **a.** Carbon cloth. Reproduced with permission from Ref.[191]. **b.** Graphite belt. Reproduced with permission from Ref.[192]. **c.** Polyaniline nanowires. Reproduced with permission from Ref.[193]. **d.** ITO nanowires. Reproduced with permission from Ref.[194]. **e.** Carbon nanotube-chitosan scaffold. Reproduced with permission from Ref.[195]. **f.** Carbon nanotube sponge. Reproduced with permission from Ref.[196]. **g.** Graphene sponge. Reproduced with permission from Ref.[197]. **h.** Graphene aerogel. Reproduced with permission from Ref.[198].

from high cost and incidental dissolution under applied electrochemical potentials, which could incur unwanted electrode corrosion and possible cytotoxicity. Alternatively, conducting polymers (e.g. polyaniline) and mental oxides (e.g. TiO_2, ITO) were explored as conductive scaffold to facilitate the extracellular electron transfer (**Figure 1.11c,d**).[193,194,206,207] A more universal strategy is to hybridise different materials and combine their traits. Such synergy has been realised on several binary or ternary composites with graphene as the structural platform whilst metallic nanoparticles, metal oxides or conducting polymers as the guest components.[198,208–211]

Single cell-level electrochemical studies revealed that the current output per cell (*G. sulfurreducens* or *S. oneidensis*) fell in the range of 15–200 fA,[212–214] which promises an areal current of $\sim$10 mA cm^{-2} or a volumetric current of $\sim 10^3$mA cm^{-3} based on single cell's geometry and represents an intrinsic upper limit of the current density attainable from a microbial fuel cell. These values are 2–3 orders of magnitude higher than those produced by state-of-the-art microbial fuel cells.[140] Rational design of the electrode architecture offers scope for improvement, by increasing the loading density of cells. Typical examples

are monolithic three dimensional electrodes such as carbon sponges, graphene aerogels (**Figure 1.11e–h**).[127,140,184,206] But their porosity was not compatible to the dimension of cells, resulting in the formation of compact biofilms with sluggish electron transfer and inefficient mass transport[175]. Thus, a hierarchical electrode with tailored structure is needed to multiply the surface area available for microbial colonies, and improve the performance of microbial electrogenesis and electrosynthesis.

1.8 Analytical techniques

Semi-artificial photosynthesis, in a broader context, also enables a suite of powerful analytical tools to delve into fundamental questions relevant to physiological functionality, biocatalytic redox chemistry and biotic-abiotic interaction.[32,215]

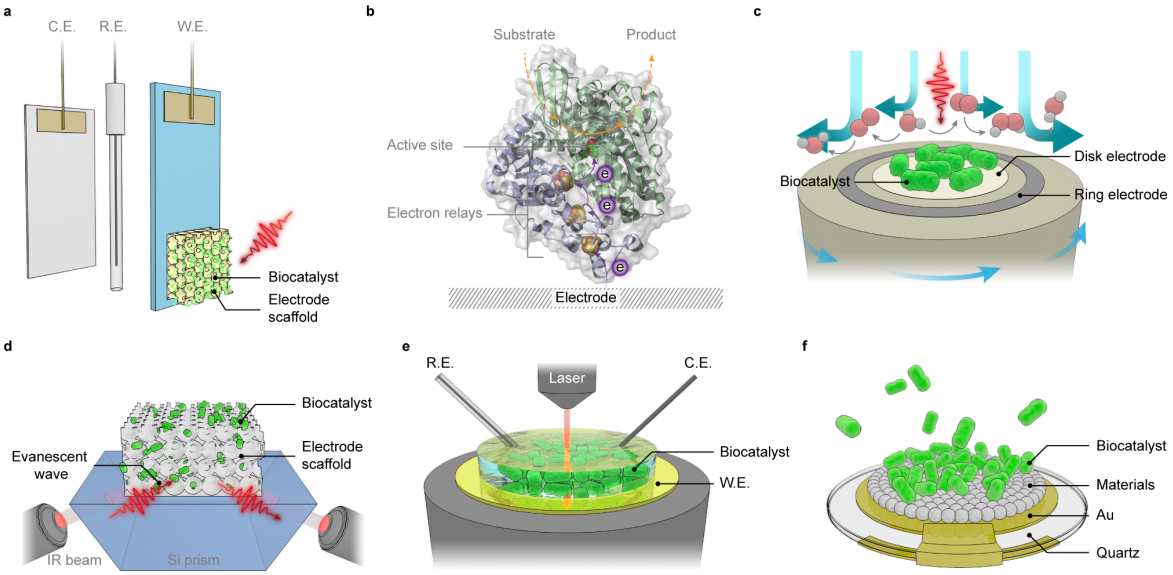

Figure 1.12 Analytic techniques employed in semi-artificial photosynthesis. **a.** A three-electrode setup comprising a working electrode (W.E.), counter electrode (C.E.) and reference electrode (R.E.) for protein film electrochemistry and microbial biofilm electrochemistry. **b.** An enzyme-electrode interface. An enzyme adsorbed on the electrode surface catalysing a redox reaction. Electrons from the electrode are delivered to the active site via intraprotein electron relays. **c.** A rotating ring disk electrode with a biocatalysts-adsorbed disk electrode and a Pt ring electrode. **d.** An ATR-IR setup with an electrode scaffold deposited on an optical waveguide crystal (e.g., a Si prism). **e.** In situ spectroelectrochemistry that combines vibrational/electronic spectroscopy with biofilm electrochemistry. **f.** A typical piezoelectric chip for quartz crystal microbalance.

Wiring enzymes or cells to an electrode allows electrochemical methods to probe their redox chemistry and physiological functionality under turnover and non-turnover conditions, through the electron transfer at the interface (**Figure 1.12a,b**).[63,216] Modulating the electrode potential or altering reaction conditions (e.g. reactant/inhibitor concentration, temperature, pH) can induce electron exchange between the electrode surface and the biocatalysts, which registers as a varying current that bears thermodynamic and kinetic features. A wealth of information with mechanistic and physiological relevance can be extracted from the interpretation of the potential-current interplay by theoretical or modelling means. For example, protein film electrochemistry has been employed to determine redox potentials, benchmark turnover rates, and delineate catalytic schemes of electroactive enzymes,[44,217] while biofilm voltammetry is used to decipher the pathways of extracellular electron transfer and unravel mechanisms of biofilm conduction.[180,218] The simplicity of the electrochemical apparatus (typically in a three-electrode electrochemical cell) renders it readily compatible with an extra light source to investigate the light-driven redox reactions of photoactive enzymes (**Figure 1.12a**).[103] Besides stationary electrodes, rotating electrodes, namely rotating disk electrodes or rotating ring disk electrodes, provide an effective way to eliminate the limitations in mass transport that often obscures catalytic features.[219] This technique has recently been applied to monitor H_2O oxidation by PSII films on electrodes and look into the photocathodic current stemming from the generation of H_2O_2 (**Figure 1.12c**).[98] The scope of electrochemical analysis can further be expanded with microelectrode-based platforms such as scanning electrochemical microscopy or microelectronic chips. These techniques allow probing the physiological functionality and catalytic activities of discrete enzymes or cells down to the single-entity level.

Complementary to electrochemical methods are spectroscopic techniques. The spectroelectrochemical measurements allow for in vivo detection of electronic and vibrational changes with relevance to enzymatic or cellular functionalities under electrochemical control and provide structural or mechanistic insights that were otherwise intractable with electrochemistry alone.[215] For example, infrared (IR) spectroscopy is a powerful method to study the structure and functionality of proteins through their vibrational signatures. A typical protein's IR spectrum features two prominent amide bands (e.g., amide I at $\sim$1650 cm^{-1}, amide II at $\sim$1550 cm^{-1}) that are sensitive to protein's secondary structure.[220] IR spectroscopy can be performed in an attenuated total reflection (ATR) mode that generates an evanescent wave to probe the surface-adsorbed entities (**Figure 1.12d**). The ATR-IR technique has been employed to monitor the enzyme (H_2ase and FDH) penetration inside an electrode scaffold and study the nature of protein-material interaction.[221,222] Resonance Raman spectroscopy can selectively probe the vibrational signatures involving metal ligands,

which further unveiled more structural and electronic subtleties of the active site of H_2ase during the catalytic cycle (**Figure 1.12e**).[223,224] This technique has recently been extended to MtrC loaded on a mesoporous ITO electrode, in attempt to elucidate its peroxidase activity.[119] UV–vis absorption spectroscopy has commonly been used to quantify the enzyme loading on an electrode via innate chromophores, i.e., chlorophylls in PSII and haem groups in MtrC.[59,118,119]

Beyond electrochemistry and spectroscopy, quartz crystal microbalance (with dissipation) enables a sensitive method to measure the mass change down to the single-molecule level on a piezoelectric quartz chip (**Figure 1.12f**).[56] This allows quantification of enzyme loadings in an electrode scaffold, which is not readily accessible by electrochemical or spectroscopic means and can be further extrapolated to evaluate the nature of enzyme interaction with electrode materials.[221,222] With more tools being added to the toolbox, these emerging analytic techniques can provide fresh insights from different perspectives to assemble a more comprehensive picture of biohybrid systems.

1.9 Thesis outline

The aim of this thesis is to develop an array of electrodes that are versatile for biocatalysts with different morphologies and functionalities. PSII and *G. sulfurreducens* were employed as model biocatalysts in the form of enzyme and whole cell. Chapter 2 describes all the experimental details in this thesis, including electrode preparation, enzyme loading, bacteria culturing, electrochemical measurements and physical characterisation. Chapter 3 aims to establish a relationship between electrode structure and enzyme activity, which will help to formulate strategies for the design and optimisation of future photosynthetic biohybrid systems. This was achieved by a side-by-side comparison amongst an array of IO-ITO electrodes with different macro- and mesostructures, with the aid of confocal fluorescence microscopy, ATR-IR and PF-PEC. Chapter 4 extended the methodology to inverse opal-graphene electrodes as the host for PS II. The graphene electrodes underperformed in enzyme loading and photoactivity compared with IO-ITO electrodes due to their structure flaws and light absorption, which underlines the importance of electrode materials.

Chapter 3 cemented IO-ITO as a robust and versatile electrode scaffold for photoactive enzymes. In view of strengths of whole cells as biocatalysts, Chapter 5 tailored the structure of the IO-ITO electrode to host electroactive bacteria *G. sulfurreducens*. The IO-ITO electrode provided conductive and hydrophilic surfaces and thus enabled bacteria to discharge electrons arising from anaerobic respiration. A record high current density was attained with such

electrode at 0.1 V vs. SHE, indicating a high population of bacteria actively metabolising inside the scaffold. The anodic current was found dependent on the potential applied on the electrode and differential gene expression analysis was performed to gain mechanistic insights into such correlation. Chapter 6 utilised these bacteria-colonised hybrid electrodes to drive reducing reactions within and beyond their native metabolic pattern, with electrons supplied by an external circuit or ultimately outsourced to a photoanode. Chapter 7 summarises key findings in this thesis and blueprints future directions of research in the field of semi-artificial photosynthesis. This thesis represents an interdisciplinary approach to address the challenge of sustainable solar-to-chemical conversion and is part of an ongoing exploration that synergistically combines biocatalysis with synthetic materials to induce shifts in the production of high value fuels and chemicals with renewable energy sources.

Chapter 2

Experimental Section

Experiments presented in this chapter were performed solely by the author of this thesis, unless otherwise stated in the text. Contributions from others are outlined here: Dr. Tarek A. Kandiel developed the hydrothermal method of synthesising ITO nanoparticles; Dr. Katarzyna Sokol developed the IO-ITO 750 nm electrode with Sigma-Aldrich ITO nanoparticles. Prof. A. William Rutherford and Dr. Andrea Fantuzzi provided the purified PSII; Dr. Qian Wang prepared the $BiVO_4$-CoO_x electrodes; Dr. Shafeer Kalathil cultured the bacteria, performed the protein quantification and extracted RNA for sequencing; The RNA sequencing and data analysis was conducted by Cambridge Genomic Services (CGS); Dr. Nina Heidary set up the ATR-IR spectroscopy measurements and analysed the data; Dr. Giorgio Divitini acquired the FIB-SEM images.

2.1 Electrode preparation

2.1.1 Synthesis of indium tin oxide nanoparticles

The ITO nanoparticles were synthesised following a solvothermal method developed by Dr. Tarek A. Kandiel.[225] Typically, anhydrous $InCl_3$ (4.5 mmol) and $SnCl_4 \cdot 5H_2O$ (0.5 mmol) were dissolved in ethylene glycol (4 mL). To this mixture, a NaOH solution in ethylene glycol (2.5 M, 6 mL) was added under continuous stirring at 0 °C. The final NaOH concentration was 1.5 M. After 15 min of stirring, the suspension was transferred into a Teflon-lined autoclave and heated at 250 °C for 12 h to obtain ITO nanoparticles with an average size of 10 nm or for 96 h to obtain 20 nm ITO nanoparticles. After cooling to room temperature, the product was washed three times with ethanol and twice with water/ethanol mixture (50%

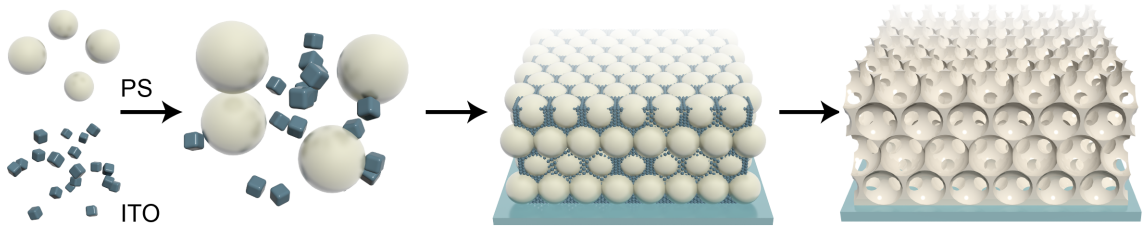

Figure 2.1 Schematic illustration to the preparation of IO-ITO electrodes by a coassembly method with PS beads and ITO nanoparticles.

v/v) then once with acetone and dried under vacuum at room temperature. For 40 nm ITO nanoparticles, NaOH concentration was adjusted to be 1.0 M and the reaction time was 96 h.

2.1.2 Inverse opal-indium tin oxide electrodes

IO-ITO electrodes with 750 nm macropores (IO-ITO 750 nm) were prepared by a coassembly method developed by Dr. Katarzyna Sokol and Dr. Dirk Mersch (**Figure 2.1**).[59,70]. Typically, ITO nanoparticles (35 mg) were dispersed in 300 µL of a mixture solution of methanol and water (6:1, v:v) and sonicated for 3 h. Monodispersed PS latex (750 nm, 2.5 wt% in water) was purchased from Polysciences Inc. and stored at 4 °C. PS latex (1 mL) was centrifuged at 7,000 rpm for 6 min to remove the supernatant and redispersed in methanol. The PS dispersion was vortexed and centrifuged again to remove the supernatant. The dispersion of ITO nanoparticles was mixed with the PS beads and the mixture was vigorously vortexed and sonicated for 30 min in ice water (< 4 °C). ITO coated glass (Visiontek System Ltd., 1 cm × 2.5 cm × 0.11 cm, 12 Ω cm^{-2}) was pre-cleaned by sonicating in acetone, isopropanol and ethanol, and stored at 150 °C. A Parafilm ring (ϕ = 0.56 cm) was placed onto the ITO glass and heated at 125 °C for 1 min to define a geometrical area of 0.25 cm^2. Then PS-ITO mixture was dropcast into the defined area and dried in air for 20 min. To make 20 µm thick IO-ITO electrodes, the volume of PS-ITO mixture varied with different ITO nanoparticles: 7.5 µL for 10 nm and 20 nm, 12 µL for 40 nm and 8.5 µL for Sigma-Aldrich (SA) ITO nanoparticles. The electrodes were annealed in air at 500 °C for 20 min with a ramping rate of 1 °C min^{-1} from room temperature.

IO-ITO electrodes with 3 µm macropores (IO-ITO 3 µm) were prepared by the coassembly method with a modified formula. Typically, ITO nanoparticles (40 mg) were dispersed in a mixture solution (350 µL) of methanol and water (11:1, v:v) and sonicated for 3 h. 1 mL of monodispersed PS latex (3 µm, 2.5 wt% in water, Polysciences Inc.) was centrifuged at 10,000 rpm for 3 min and washed with methanol. The dispersion of ITO nanoparticles

was mixed with the PS beads and sonicated for 30 min in ice water (< 4 °C). Then PS-ITO mixture was dropcast into the defined area (0.25 cm^2) on ITO glass and dried in air for 20 min. To make 20 μm thick IO-ITO electrodes, the volume of PS-ITO mixture varied with different ITO nanoparticles: 9 μL for 10 nm and 20 nm, 8 μL for 40 nm and SA ITO nanoparticles. The electrodes were annealed in air at 500 °C for 20 min at 1 °C min^{-1}.

IO-ITO electrodes with 10 μm macropores (IO-ITO 10 μm) were prepared following a modified coassembly method. Typically, ITO nanoparticles (20 mg) were dispersed in a mixture solution (125 μL) of methanol and water (11:1, v:v) and sonicated for 3 h in ice water. 750 μL of monodispersed PS latex (10 μm, 2.5 wt% in water, Polysciences Inc.) was centrifuged at 10,000 rpm for 3 min and washed with methanol. The dispersion of ITO nanoparticles was mixed with the PS beads and sonicated for 30 min in ice water (< 4 °C). 15 μL of PS-ITO mixture was dropcast into the defined area (0.25 cm^2) on ITO glass and dried in air for 20 min. The electrodes were then annealed in air at 500 °C for 20 min at 1 °C min^{-1}.

IO-ITO electrodes with 20 μm macropores (IO-ITO 20 μm) were prepared following a modified co-assembly method. Typically, ITO nanoparticles (15 mg) were dispersed in a mixture solution (150 μL) of methanol and water (11:1, v:v) and sonicated for 3 h in ice water. 1 mL of monodispersed PS latex (10 μm, 2.5 wt% in water, Polysciences Inc) was centrifuged at 10,000 rpm for 3 min and washed with methanol. The dispersion of ITO nanoparticles was mixed the PS beads and sonicated for 30 min in ice water (< 4 °C). 15 μL of PS-ITO mixture was dropcast into the defined area (0.25 cm^2) on ITO glass and dried in air for 20 min. The electrodes were then annealed at 500 °C for 20 min at 1 °C min^{-1}.

2.1.3 Inverse opal-graphene electrodes

Graphene oxide (GO) was synthesised by a modified Hummer's method.[226] In brief, H_2SO_4 (20 mL, 98%), $K_2S_2O_8$ (4.2 g), graphite powder (5 g, 325 mesh) were added to a 250 mL round bottom flask. The mixture was vigorously stirred at 80 °C for 4.5 h, then cooled down to room temperature. The mixture was then diluted with water and left overnight. The mixture was repeatedly washed with 1 L water and dried in the air overnight to obtain a pre-oxidised graphite. Next, a 250 mL round bottom flask was placed in an ice bath. H_2SO_4 (58 mL, 98%) and graphite oxide (2.5 g) were slowly added into the flask with vigorous stirring. Then HNO_3 (1.25 g) and $KMnO_4$ (8.0 g) were slowly added during which the temperature was kept below 10 °C. The mixture was then heated to 35 °C and stirred for 2 h, and then diluted with 58 mL water and stirred for another 2 h, followed by adding 350

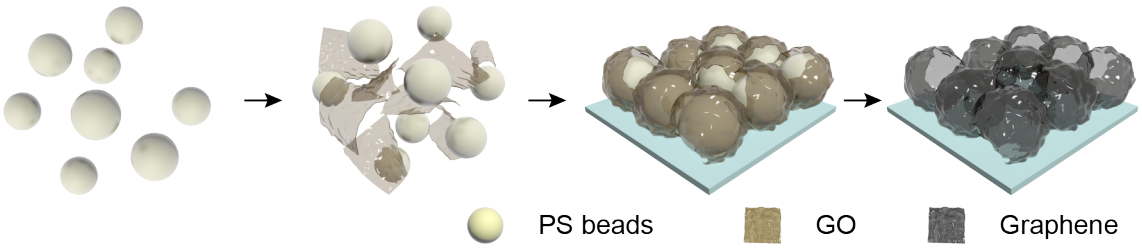

Figure 2.2 Schematic illustration to the preparation of IO-graphene electrodes by a coassembly method with PS beads and GO microsheets.

mL water. H_2O_2 (25 mL, 30%) was added in dropwise to the solution and left overnight for stratification. The supernatant was decanted and the GO was washed with water and 1 M HCl for five times to remove the metal oxides, washed with water until the supernatant was nearly neutral. Finally, GO was dispersed in water and sonicated for 30 min to obtain a brownish solution. GO powder was obtained by freeze-drying the GO solution at $-76\,^{\circ}C$ for 72 h.

The IO-graphene electrodes were prepared by coassembling PS beads with GO, followed by thermal reduction into reduced GO (RGO) (**Figure 2.2**). In this thesis, GO powder was redispersed in water to make colloidal solutions of different concentrations (4 mg mL^{-1} and 10 mg mL^{-1}, denoted as Gr I and Gr II respectively). 1 mL of PS latex (750 nm, 3 µm, 2.5 wt%) was centrifuged and washed with water. GO solutions were mixed with PS beads and sonicated in ice water (< 4 °C) for 2 h. A Scotch tape ring was placed on ITO-coated glass (Visiontek System Ltd., 1 cm × 2.5 cm × 0.11 cm, 12 Ω cm^{-2}) to define a geometrical area of 0.25 cm^2. To make 20 µm thick electrodes, different volumes of PS-GO mixtures were dropcast on the ITO glass and dried in air for 1 h: 18 µL Gr I-750 nm, 7 µL Gr I-3 µm, 9 µL Gr II-750 nm, and 7 µL Gr II-3 µm. The electrodes were annealed at 500 °C at for 20 min at 1 °C min^{-1} in Ar flow (80 sccm) to remove PS beads and reduce GO. The resulting IO-graphene electrodes were treated with a UV-ozone cleaner for 20 min to improve hydrophilicity.

2.1.4 Inverse opal-titanium oxide electrodes

TiO_2 nanoparticles (Evonik, Aeroxide, P25, 21 nm, anatalse:rutile (80:20), 5 mg) were dispersed in a mixture of methanol and water (6:1, v:v, 75 µL) and sonicated for 2 h. 10 µm PS latex (1 mL, 2.5 wt% in water.) was washed and mixed with TiO_2 nanoparticles by sonicating for 30 min in ice water (< 4 °C). 5 µL of the PS-TiO_2 mixture was dropcast onto

ITO glass slides with a pre-defined area of 0.25 cm^2.The electrodes then were annealed at 500 °C in air for 20 min at a ramping rate of 1 °C min^{-1}.

2.1.5 Inverse opal-zirconium oxide electrodes

ZrO_2 nanoparticles (20–30 nm, 20 mg) were dispersed in a mixture of methanol and water (11:1, v:v, 150 µL) and sonicated for 2 h. 10 µm PS latex (0.75 mL, 2.5 wt% in water.) was washed with water and methanol. PS beads were then mixed with the ZrO_2 nanoparticles dispersion by sonicating for 30 min in ice water (< 4 °C). 15 µL of the PS-ZrO_2 mixture was dropcast onto ITO glass slides with a pre-defined area of 0.25 cm^2.The electrodes then were annealed at 500 °C in air for 20 min at a ramping rate of 1 °C min^{-1}.

2.1.6 Bismuth vanadate electrodes

The $BiVO_4$-CoO_x electrode was prepared by Dr. Qian Wang according to a previously-reported method.[227] Bismuth precursor thin films were first electrochemically deposited on FTO glass slides (Sigma Aldrich; 8 Ω cm^{-2}) in a three-electrode system consisting of a Ag/AgCl reference electrode (in 3 M NaCl solution) and a Pt counter electrode. $Bi(NO_3)_3$ solution (25 mL 0.1 M, in acetic acid, pH 4.8) was mixed with *p*-benzoquinone (20 mL, 0.3 M, in ethanol) as the electrolyte. Electrodeposition was performed on an FTO glass slide with a pre-defined area of 1.0 cm^2 at 2.3 V vs. Ag/AgCl for 7 min at 25 °C using a potentiostat (MultiEmStat3+). The obtained bismuth precursor film was washed with water and dried in air, followed by dip-coating with vanadyl diacetylacetonate (0.2 M in dimethylsulfoxide/ethanol (1:1, v:v)). The electrode was then calcinated at 520 °C in air for 2 h at a ramping rate of 2 °C min^{-1}. Then the electrode was washed with NaOH (1 M) for 10 min and water to remove excess VO_x. The obtained $BiVO_4$ electrode was immersed in a $Co(NO_3)_2$ solution (20 mL, 10 mM, in 10 mM $NH_3 \cdot H_2O$, pH 8.4) for 30 min to load CoO_x. The $BiVO_4$-CoO_x electrode was then washed with water and annealed at 250 °C in air for 30 min at a ramping rate of 2 °C min^{-1}.

2.2 Photosystem II photoelectrochemistry

2.2.1 Photosystem II separation and purification

PSII used in this thesis was provided by Prof. A. William Rutherford and Dr. Andrea Fantuzzi from Imperial College London and was prepared according to a previously reported protocol.[89,228–230] In brief, thermophilic cyanobacteria *Thermosynechococcus elongatus* (*T. elongatus*) (43-H strain) were grown in 3 L Erlenmeyer flasks in a rotary shaker (120 rpm) at 45 °C under continuous fluorescent white-lamp illumination ($\approx$ 80 µmol $m^{-2}s^{-1}$). The cells were grown in a CO_2-enriched atmosphere until they reached an optical density (OD) 1.0 at 800 nm. The cells were centrifuged and washed once with a buffer solution (buffer I, pH 6.5) containing 40 mM 2-(*N*-morpholino)ethanesulfonic acid (MES), 15 mM $MgCl_2$, 15 mM $CaCl_2$, 10% glycerol, 1.2 M betaine and resuspended in the same buffer with 0.2% (w/v) bovine serum albumin, 1 mM benzamidine, 1 mM aminocaproic acid and 50 µg mL^{-1} DNase I to make chlorophyll (Chl) concentration 1.5 mg mL^{-1}. The cells were ruptured with a French press (700 psi), followed by centrifugation (1000 $\times g$, 5 min) to remove the unbroken cells. Thylakoids were pelleted by centrifugation (180,000 $\times g$, 35 min) at 4 °C and washed twice with buffer I. Thylakoids were finally resuspended in buffer I and stored in liquid N_2 at a Chl concentration of 1 mg mL^{-1} before use.

Thylakoids (1 mg mL^{-1}) were treated with 1% (w/v) *n*-dodecyl-β-maltoside (β-DM, Biomol, Germany) in buffer I with 100 mM NaCl. After stirring in the dark at 4 °C, the suspension was centrifuged (170,000 $\times g$, 10 min) to remove the non-solubilised material. The supernatant was mixed with an equal volume of Probond resin (Invitrogen, Groningen, The Netherlands) that had been pre-equilibrated with buffer I. The resulting slurry was transferred to an empty column and the supernatant was removed after resin sedimentation. The resin was washed with buffer II (40 mM MES, 15 mM $MgCl_2$, 15 mM $CaCl_2$, 100 mM NaCl, 15 mM imidazole, 0.03% (w/v) β-DM, 10% (v/v) glycerol, 1.2 M betaine, pH 6.5) until the OD value of the eluate at $\approx$ 670 nm decreased below 0.05. Then, PSII core complexes were eluted with buffer III (150 mM MES, 15 mM $MgCl_2$, 15 mM $CaCl_2$, 200 mM NaCl, 300 mM imidazole, 0.1% (w/v) β-DM, 10% (v/v) glycerol, 1.2 M betaine, pH 6.5). The eluate was then precipitated with buffer I containing 15% (w/v) polyethylene glycol 8000 by centrifugation (170,000 $\times g$, 10 min). PSII core complexes were finally resuspended in buffer I at a Chl concentration of 1–1.5 mg mL^{-1} and stored in liquid N_2 before use.

2.2.2 Loading photosystem II on electrodes

A PSII stock solution (4.25 mg_{Chl} mL^{-1}, 136 µM PSII monomers) was diluted with a stock buffer (pH 6.5) containing 40 mM MES, 30 mM $MgCl_2$, 15 mM $CaCl_2$, 10% (v/v) glycerol and 1 M betaine. 1.25 µL of PSII stock solution (2.13 mg_{Chl} mL^{-1}, 85.2 pmol PSII monomers) was dropcast on each IO-ITO electrodes while 0.9 µL of PSII stock solution (1.30 mg_{Chl} mL^{-1}, 37.4 pmol PSII monomers) was dropcast on each IO-graphene electrode. The PSII-loaded electrodes were incubated in air for 15 min in the dark.

The PSII monomers loaded on electrodes were quantified by UV–vis analysis after each PF-PEC experiment.[116] The IO-ITO and IO-graphene scaffolds were scratched from the ITO glass and dispersed in methanol (0.5 mL). After centrifugation (10,000 rpm, 4 min), the supernatant was extracted and transferred into a quartz cuvette for UV–vis analysis. Assuming each PSII monomer has 35 Chl *a* molecules, the amount of PSII monomers were determined according to Equation (2.1)

$$\Gamma_{PSII} = \frac{A_{665\,nm} - A_{750\,nm}}{35 \cdot \varepsilon \cdot l} \cdot V_{MeOH} \tag{2.1}$$

where Γ_{PSII} is the amount of PSII monomers; $A_{665\,nm}$ and $A_{750\,nm}$ are absorbance at 665 nm and 750 nm respectively; ε is the molar attenuation coefficient (ε = 79.95 mL mg^{-1} for Chl *a* molecules);[231] l is the path length of the light beam through the quartz cuvette (l = 1 cm); V_{MeOH} is the volume of methanol (V_{MeOH} = 0.5 mL).

2.2.3 Protein film-photoelectrochemistry

PF-PEC experiments were performed in a three-electrode system in an electrochemical cell that was enveloped with a water jacket (25 °C). A potentiostat (Ivium CompactStat) was coupled with a monochromatic red LED light source (λ = 685 nm, I = 10 mW cm^{-2}) collimated by two plano-convex lenses (THORLABS N-BK7, d = 7.5 cm, f = 5.0 cm). The working electrode was placed to face the LED light source with its front side. The light intensity reaching the electrode surface was calibrated by a light meter (QRT1 Quantitherm, Hansatech Instruments) before each experiment. A Pt mesh was used as the counter electrode and Ag/AgCl (in 3 M NaCl solution) as the reference electrode. The electrolyte solution (pH 6.5) contained 40 mM MES, 20 mM $CaCl_2$, and 5% (v/v) glycol. 40 µL of 2,6-dichloro-1,4-benzoquinone (DCBQ) solution (0.1 M in dimethyl sulfoxide) was added to the electrolyte solution for mediated photocurrent measurements. A potential of 0.5 V vs. SHE was applied throughout all measurements. The PSII-loaded electrodes were kept in the dark for 90 s and

then periodically irradiated for 15 s with an interval of 15 s. The TOF of PSII monomer was calculated assuming 100% Faraday efficiency of oxygen evolution using Equation (2.2):

$$\mathrm{TOF} = \frac{M_{\mathrm{O_2}}}{\Gamma_{\mathrm{PSII}}} = \frac{J}{4eN_A \cdot \Gamma_{\mathrm{PSII}}} \tag{2.2}$$

where Γ_{PSII} is PSII loading on electrodes; $M_{\mathrm{O_2}}$ is the amount of oxygen evolution; J is the photocurrent density (normalised by the geometrical area of electrodes); N_A is the Avogadro constant; e is the elementary charge.

2.3 Microbial electrochemistry

2.3.1 Culturing of bacteria

Bacteria used in this thesis were cultured by Dr. Shafeer Kalathil. *Geobacter sulfurreducens* PCA (*G. sulfurreducens*) (ATCC 51573) and *Shewanella loihica* PV-4 (*S. loihica*) were purchased from Leibniz-Institut DSMZ-Deutsche Sammlung von Mikroorganismen und Zellkulturen GmbH, Germany. *G. sulfurreducens* was cultured anaerobically in a medium solution (DSMZ 826) using sodium acetate (20 mM) as the electron donor and sodium fumarate (50 mM) as the electron acceptor. The bacterial strain was inoculated in 20 mL of the medium solution in a sterilised vial and was purged with N_2:CO_2 (80:20 v:v%) for 1 h. The inoculated media were kept in a shaking incubator (30 °C, 180 rpm) for 5 days. *S. loihica* was cultured aerobically in Luria-Bertani medium solution by keeping in a shaking incubator (30 °C, 180 rpm) overnight. The concentration of bacteria suspension was determined by measuring optical density at 600 nm using a UV–vis spectrometer (Varian Cary 50, Agilent Technologies). To suppress the outer-membrane cyt *c* without altering their genes, *G. sulfurreducens* was cultured in the standard medium solution containing 2,2′-bipyridine (30 µM) as the iron chelator to limit the iron availability.[232] *G. sulfurreducens* was first cultured in an iron-lacking medium at 30 °C for 5 days. Then 30 µM 2,2′-bipyridine was added into the medium and the bacteria were cultured anaerobically at 30 °C for another 5 days.

2.3.2 Microbial electrochemistry

The chronoamperometry and cyclic voltammetry were performed using a potentiostat (Multi-EmStat3+) in a three-electrode system in a three-neck round bottom flask in a water bath (30 °C) under continuous stirring (200 rpm). A Pt mesh was used as the counter electrode

Table 2.1 Components of medium for *G. sulfurreducens* (DSMZ 826)

NH_4Cl	1.50 g
Na_2HPO_4	0.60 g
KCl	0.10 g
$NaHCO_3$	2.50 g
Trace element solution	10.0 mL
Vitamin solution	10.0 mL
H_2O	980.0 mL

Table 2.2 Components of medium for trace element solution

Nitrilotriacetic acid	1.50 g
$MgSO_4 \cdot 7H_2O$	3.00 g
$MnSO_4 \cdot H_2O$	0.50 g
NaCl	1.00 g
$FeSO_4 \cdot 7H_2O$	0.10 g
$CoSO_4 \cdot 7H_2O$	0.18 mL
$CaCl_2 \cdot 2H_2O$	0.10 mL
$ZnSO_4 \cdot 7H_2O$	0.18 g
$CuSO_4 \cdot 5H_2O$	0.01 g
$KAl(SO_4)_2 \cdot 12H_2O$	0.02 g
H_2BO_3	0.01 g
$Na_2MoO_4 \cdot 2H_2O$	0.01 g
$NiCl_2 \cdot 6H_2O$	0.03
$Na_2SeO_3 \cdot 5H_2O$	0.30 g
$Na_2WO_4 \cdot 2H_2O$	0.40 g
H_2O	1000.0 mL

Table 2.3 Components of Vitamin solution

Biotin	2.0 mg
Folic acid	2.0 mg
Pyridoxine-HCl	10.0 mg
Thiamine-$HCl \cdot 2H_2O$	5.0 mg
Riboflavin	5.0 mg
Nicotinic acid	5.0 mg
D-Ca-pantothenate	5.0 mg
Vitamin B12	0.1 mg
p-Aminobenzoic acid	5.0 mg
Lipoic acid	5.00 g
H_3BO_3	0.01 g
H_2O	1000.0 mL

Table 2.4 Components of Luri-Bertani medium

Tryptone	10.0 g
Yeast extract	5.0 g
NaCl	10.0 g

and Ag/AgCl (in 3 M NaCl solution) as the reference electrode. Sodium acetate (40 mM) was added into the medium solution (14 mL) as the electrolyte and purged with N_2:CO_2 (80:20 v:v%) for 40 min. *G. sulfurreducens* suspension (1 mL) was inoculated into the medium solution (final OD: 0.6) and purged for 20 min. The IO-ITO electrodes were used as the anode and poised at different potentials (0.0–0.4 V vs. SHE). Cyclic voltammetry was carried out at a scan rate of 5 mV s^{-1} after the anodic current reached a plateau. To perform microbial electrosynthesis, the electrolyte was replaced with a medium solution containing sodium fumarate (50 mM) and purged with N_2:CO_2 (80:20 v:v%) for 40 min. A potential of −0.45 V vs. SHE was applied on the microbial electrodes and the cathodic current was recorded. To coculture with *S. loihica*, sodium lactate (40 mM) was added in the medium solution (13 mL) as the electron donor to *S. loihica*, and purged with N_2:CO_2 (80:20 v:v%) for 40 min. *G. sulfurreducens* suspension (1 mL, final OD: 0.6) and *S. loihica* (1 mL, final OD: 0.6) were inoculated into the medium solution and purged for 20 min. The IO-ITO electrodes were used as the working electrode and poised at a potential of 0.4 V vs. SHE.

2.3.3 Microbial photoelectrosynthesis

IO-TiO_2 (pore size: 10 µm; thickness: 40 µm; geometrical area: 0.25 cm^2) were cleaned with a UV-ozone cleaner for 15 min before use. The IO-TiO_2|**RuP** photoanode was prepared by immersing the IO-TiO_2 electrodes in [Ru(II)bis(2,2′-bipyridine)(2,2′-bipyridine-4,4′-diylbis(phosphonic acid))]Br_2 (**RuP**, 0.25 mM in H_2O) for 16 h in the dark, followed by rinsing with water to remove weakly adsorbed dyes. Stepped chronoamperometry of the IO-TiO_2|**RuP** electrode was conducted in TEOA (25 mM, pH 7.2, in 0.1 M NaCl solution) in a N_2:CO_2 atmosphere (80:20, v:v%) with Pt and Ag/AgCl as the counter and reference electrode, respectively. The electrode was under periodic irradiation (10 s in light, 30 s in dark, I = 100 mW cm^{-2}, AM 1.5G) at stepped potentials from −0.7 V to 0.4 V vs. SHE every 40 s. The $BiVO_4$-CoO_x electrode (1.0 cm^2) was directly used as the photoanode without any pre-treatment. Linear sweep voltammetry of the $BiVO_4$-CoO_x electrode was carried out in a phosphate buffered saline solution (20 mM Na_2HPO_4, 3.6 mM KH_2PO_4, 5.4 mM KCl, 0.274 M NaCl, pH 7.3) in N_2:CO_2 (80:20, v:v%) under periodic irradiation (5 s in light, 5 s in dark, I = 100 mW cm^{-2}, AM 1.5G) at a scan rate of 5 mV s^{-1} with Pt

and Ag/AgCl as the counter and reference electrode, respectively. The photoanode and the IO-ITO|*G. sulfurreducens* electrode were connected in a two-compartment, two-electrode PEC cell separated by a Nafion membrane. A bare IO-ITO electrode without bacteria and an IO-ITO hybrid electrode with *G. sulfurreducens* inactivated by 0.1% glutaraldehyde were used for control experiments. TEOA (25 mM, pH 7.2, in 0.1 M NaCl solution) was used as the electrolyte and electron donor for the IO-TiO_2|**RuP** electrode, whereas a phosphate buffered saline solution (20 mM Na_2HPO_4, 3.6 mM KH_2PO_4, 5.4 mM KCl, 0.274 M NaCl, pH 7.3) was used as the electrolyte for the $BiVO_4$-CoO_x electrode. Sodium fumarate (20 mM, in medium solution) was used as the substrate and electrolyte for the cathode. The PEC cell was purged with N_2:CO_2 (80:20 v:v%) for 40 min. The photoelectrosynthesis was performed using simulated solar light (I = 100 mW cm^{-2}, AM 1.5G) (LOT Quantum Design) from a 150 W Xe lamp (Newport). Light intensity was calibrated by a thermal sensor (S302C, Thorlabs) and power meter console (PM100D, Thorlabs). Zero bias (U = 0) was applied between the photoanode and the cathode during the PEC experiment. Dark current was recorded for 30 min before and after irradiation for 24 h. Solution in the cathode chamber before and after the light experiment was extracted for product quantification.

2.3.4 Protein quantification

The proteins in the electrodes were quantified by Dr. Shafeer Kalathil through a colorimetric assay.[233] The microbial electrode was immersed in a sodium dodecyl solution (5 mL, 10 wt%) solution at 99 °C for 15 min to extract proteins from the electrode. Then the solution was centrifuged (14,000 rpm, 10 min) to remove the impurities. The supernatant was used to quantify the protein using the Bio-Rad protein assay. Typically, 100 µL of the protein solution was added into a clean test tube, followed by adding 5 mL of the diluted dye reagent and incubating at 25 °C for 10 min. Then the light absorbance at 600 nm was measured using a UV–vis spectrometer. Bovine serum albumin was used as the standard protein to make the correlation curve. The protein concentration was calculated from the standard curve. Each protein solution was assayed in triplicate.

2.3.5 Differential gene expression analysis

The RNA sequencing and differential gene expression analysis was conducted by Cambridge Genomic Services (CGS). IO-ITO|*G. sulfurreducens* electrodes were prepared at different potentials following the method reported above. The plateau current density attained at 0.1 V and 0.4 V vs. SHE were 1.12 ± 0.05 mA cm^{-2} and 2.82 ± 0.25 mA cm^{-2}, respectively. The

biohybrid electrode was scratched off the ITO glass slide and cells in electrodes were lysed with TissueLyser II immediately after the chronoamperometry was stopped. The mixture was sonicated for 1 min and centrifuged at 8000 $\times g$ for 15 min. The resulting supernatant was used for RNA extraction. *G. sulfurreducens* anaerobically cultured in acetate (20 mM) and fumarate (50 mM) at 30 °C was used as control samples. RNA of *G. sulfurreducens* were extracted by Dr. Shafeer Kalathil using a RNeasy protect bacteria mini kit (Qiagen, USA) at room temperature. The extracted RNA were eluted in nuclease free water. The quality control showed the q-score across all samples are above 30, signifying high sample quality. Reads were mapped with *G. sulfurreducens* reference genome using STAR v2.5.2a. Using the genes annotation defined in the *G. sulfurreducens* gtf file from Ensembl Bacteria. The reads mapping into genomics features were counted using HTSeq v0.6.0. A feature is considered as the union of all gene's exons whose genomic coordinates are determined from the *G. sulfurreducens* gtf. Reads with a mapping quality less than 10, or those that map to multiple loci or to overlapping gene regions are discarded to avoid ambiguity and false positives. Differential gene expression analysis was performed using the counted reads and the R package edgeR version 3.16.5 for the 3 pairwise comparisons.

2.4 Physical characterisations

2.4.1 ATR-IR spectroscopy

ATR-IR spectroscopy of IO-ITO|PSII electrodes was conducted by Dr. Nina Heidary on a Bruker Vertex 70 spectrometer equipped with a PIKE ATR set-up, a liquid nitrogen-cooled mercury cadmium telluride detector (HgCdTe) and a Globar IR radiation source. The spectrometer chamber was purged with N_2 for all experiments. The customized ATR-IR unit consisted of a trapezoidal silicon crystal with an incident angle of 60° and with an aperture setting of 3 mm. Spectra were acquired in the spectral region between 4000 and 1000 cm^{-1} with a spectral resolution of 4 cm^{-1}. Each spectrum was accumulated from 200 scans in 90 s. The IO-ITO films (SA, 750 nm and 3 µm) on the silicon prism were prepared according to the same method previously described (Section 2.1.2). The 40 nm planar ITO film was sputtered on the silicon prism by a sputter coater (Quorum Q150T ES) at a rate of 16 nm min^{-1} and a sputter current of 100 mA, using a high purity ITO sputter target (Labtech International Ltd). 1 µL of PSII stock solution (2.5 $mg^{-1}_{Chl\ a}$ mL^{-1}, 80 pmol PSII monomers) was dropcast on each electrode. The spectra of IO-ITO|PSII electrodes were corrected with a stock buffer solution (pH 6.5, containing 10% glycerol, 30 mM $MgCl_2$, 15 mM $CaCl_2$ and 40

mM MES). All the spectral data was processed with the OPUS 5.5 software. Biexponential fitting $A = A_0 + A_1 e^{-t/\tau_1} + A_2 e^{-t/\tau_2}$ was applied in the first 25 min. A_0, A_1 and A_2 present the absorbance intensities of amide I or amide II band at the final adsorption time, at the first and the second completed adsorption process, respectively. τ_1 and τ_2 present time constants for the first and the second adsorption process, respectively.

2.4.2 Confocal laser scanning microscopy

Confocal laser scanning microscopy (CLSM) images of IO-ITO|PSII electrodes were acquired on a Leica TCS SP8 confocal microscope using a ×10 objective in air. A 633 nm laser (HeNe) was used for excitation and a hybrid dector (HyD) was used to collect the emitted fluorescence in the range of 650–750 nm. CLSM images were captured with a high-resolution galvano scanner (400 Hz, 512 × 512 pixels). Z-stack images were acquired by first focusing on the electrode surface using the optical microscope and then scanning downwards for 20 µm (z-depth of 0.5 µm) to include the entire electrode. Images were processed by ImageJ software to reconstruct a 3D view. Each IO-ITO electrode (geometrical area: 0.25 cm^2) was dropcast with 80 pmol of PSII monomers (1 µL of PSII stock solution ∼2.5 $mg^{-1}_{Chl\ a}$ mL^{-1}) while each IO-graphene electrode (geometrical area: 0.25 cm^2) was dropcast with 37 pmol of PSII monomers (0.9 µL of PSII stock solution ∼1.3 $mg^{-1}_{Chl\ a}$ mL^{-1}). PSII-loaded electrodes were then incubated in air for 30 min in the dark at room temperature before CLSM imaging. CLSM images of IO-ITO|*G. sulfurreducens* electrodes were acquired on a confocal laser scanning microscope (Leica TCS SP8) using a 488 nm laser and a hybrid detector (600–650 nm). 100 µL of 5-cyano-2,3-ditolyl tetrazolium chloride (10 mM in medium solution) was dropcast on an IO-ITO|*G. sulfurreducens* electrode that was then incubated in the dark for 30 min at 25 °C.

2.4.3 General characterisations

Scanning electron microscope (SEM) images were acquired on a TESCAN MIRA3 at an accelerating voltage of 5 kV. The energy dispersive X-ray (EDX) spectra and element mapping images were acquired from an EDX detector (Brucker QUANTAX EDS), at an accelerating voltage of 10 kV. Transmission electron microscope (TEM) images were obtained from a transmission electron microscope (Tecnai G2) performed at an accelerating voltage of 200 kV. Scanning transmission electron microscope (STEM) images were acquired on a scanning electrode microscope (TESCAN MIRA3) at an accelerating voltage of 30 kV. Cross-sectional SEM images of IO-ITO|*G. sulfurreducens* were acquired by Dr. Giorgio Divitini on a

focused ion beam-scanning electron microscope (FIB-SEM, ZEISS Crossbeam 540) at an acceleration voltage 1.6 kV. Serial sectioning was carried out using FIB milling at a 3 nA ion current and a slice thickness of 500 nm. Before SEM imaging, the bacteria-colonised electrodes were treated with 2.5 wt% glutaraldehyde and 2 wt% osmium tetraoxide, and then dehydrated with a series of ethanol solutions with increasing concentrations (30, 50, 70, 90 and 100%) and dried in air. X-ray microscopy image of the IO-ITO electrode was acquired on a 3D X-ray microscope (Zeiss Xradia 510 Versa). Atomic force microscope (AFM) images were acquired on an atomic force microscope (NanoIR2, ANASYS Instrument) in a contact mode using a gold-coated silicon tip. Raman spectra and Raman mapping images were obtained from a HORIBA LabRAM HR Evolution system with an incident laser of 533 nm. IR spectra were recorded on a Nicolet iS50 spectrometer in an ATR mode. The powder XRD patterns of the ITO nanoparticles were collected on an X'Pert PRO X-ray diffractometer (PANalytical B.V.). The contact angle measurement was conducted on an FTA 1000 drop shape analyser using ultrapure water. UV–vis absorption and transmission spectra were recorded on a Varian Cary 50 spectrophotometer. The photoluminescence spectra were obtained from a Spectrofluorometer FS 5 (Edinburgh instruments) using a front face sample holder (SC-10). The iron contents of wild-type and cytochrome-suppressed bacteria were determined by inductively coupled plasma-optical emission spectrometry (ICP-OES, Thermo scientific). ^{1}H NMR spectroscopy analysis was conducted on a Bruker 400 MHz NMR spectrometer in D_2O. Sodium 3-(trimethylsilyl)propionate-2,2,3,3-d^4 (TMSP-d^4, 1 mM) was used as the reference and internal standard for quantification. NMR spectra were processed with MestReNova v12.0.

All experiments were performed in three individual replicates unless otherwise mentioned. Data are presented in bar diagrams as mean $\pm$ standard error of the mean (s.e.m.). The mean values and standard errors of the mean were calculated from the number of repeats of independent experiments. Statistical analyses were conducted using GraphPad Prism v.6.0 g. Statistical significance was determined by one-sided analysis of variance (ANOVA) for multiple groups of samples and Student's t tests for unpaired two samples. $P < 0.05$ was considered statistically significant.

Chapter 3

Interfacing photosystem II with inverse opal-indium tin oxide electrodes

The contents of this chapter have been published in a peer-reviewed article: Xin Fang, Katarzyna P. Sokol, Nina Heidary, Tarek A. Kandiel, Jenny Z. Zhang, Erwin Reisner, Nano. Lett.,* ***2019****, 19, 1844–1850. Results presented in this chapter were obtained solely by the author of this thesis, with contributions from others as outlined here: Dr. Katarzyna Sokol developed the IO-ITO 750 nm electrode with Sigma-Aldrich ITO nanoparticles; Dr. Tarek A. Kandiel developed the hydrothermal method of synthesising ITO nanoparticles; Prof. A. William Rutherford and Dr. Andrea Fantuzzi provided the purified PSII; Dr. Nina Heidary set up the ATR-IR spectroscopy measurements and analysed the data.*

3.1 Introduction

Natural photosynthesis harvests sunlight to energise electrons and pump protons from water oxidation for carbon dioxide fixation, which is carried out by a series of enzymes that are orchestrated in thermodynamics and kinetics (Section 1.1).[10] PSII is the only enzyme known able to photocatalyse the energy-demanding water oxidation reaction at a high TOF of $\sim$100 s^{-1},[90] extracting electrons from water and initiating the vectorial electron transfer in the thylakoid membrane (**Figure 1.5**). Photoelectrogenesis in PSII starts from the excitation of the reaction center chlorophylls (P680), followed by electron transfer from the excited $P680^*$ to the terminal acceptor Q_B via pheophytin and Q_A. In nature, the fully-reduced Q_B (Q_BH_2) will dissociate from the reaction centre complex and donate the electrons to PSI via a cyt b_{6f} complex.[5] The electron transfer pathway from PSII to the cytochrome

can be intercepted by exogenous acceptors such as molecular mediators and synthetic electrodes,[103,106] which enables unique opportunities to redirect the photosynthetic electron flux for chemical synthesis and fuel production.

Semi-artificial photosynthesis combines strengths of both synthetic materials and biocatalysts to produce value-added chemicals with high selectivity and efficiency, which cannot be achieved by synthetic biology or artificial photosynthesis alone (Section 1.4).[57,130] Photosynthetic enzymes have been wired into many synthetic electrodes via self-assembled monolayers, metal oxide scaffolds, and redox polymer matrices, but their responsive photocurrent was limited by the low protein loading (Section 1.5). To overcome this limitation, hierarchical three-dimensional electrodes with high surface area were produced to enhance protein loading and facilitate electron exchange at the protein-electrode interface (biointerface). For example, IO-ITO electrodes allow proteins to penetrate through their interconnected macropores, and have mesoporous skeletons with high surface area for protein binding and electronic communication,[59,70,120,122,123] thereby increasing the mediated photocurrent up to 1 mA cm^{-2}.[59,70] A major challenge facing semi-artificial photosynthesis is that enzymes integrated in electrodes often exhibit reduced activity when stripped from their in vivo environment and that only a small fraction of enzymes at the biointerface are in an electroactive orientation (**Figure 1.6**). Addressing these challenges requires an in-depth interrogation of bioelectrodes to identify factors governing the photoelectrogenesis at the biointerface. Nevertheless, such investigations are lacking due to difficulties in accessing the nanoscale proteins in complex three-dimensional structures, which renders the protein-electrode interaction and its correlation with photoelectrochemistry largely unclear, and further confounds efforts to enhance the photocatalytic performance of bioelectrodes.

This chapter presents a systematic study of PSII-integrated three-dimensional electrodes to outline the structure-activity relationship underlying enzymatic water oxidation therein, through a new approach combining material synthesis, microscopy, spectroscopy and electrochemistry. IO-ITO electrodes with varied macro- and mesostructures were fabricated to integrate with PSII, and confocal laser scanning microscopy (CLSM) and in situ ATR-IR spectroscopy were employed to visualise the protein distribution and monitor their penetration into the electrode scaffolds, respectively. The yielded structural insights were finally correlated with the enzyme activity that was quantified by PF-PEC. I find that the three-dimensional hierarchical electrodes with smaller macropores and mesopores larger than the protein size enabled higher loading capacity and better enzyme retention, whereas the individual enzyme activity is more sensitive to the light intensity and electronic communication at the biointerface, rather than the electrode morphology. These results reveal the relationship

between the electrode structure and enzyme activity and provide useful guidelines for the design and optimisation of photoactive bioelectrodes.

3.2 Electrode structures and properties

The IO-ITO electrodes were fabricated by coassembling PS beads and ITO nanoparticles,[59,70] which were used as sacrificial templates to create macroporosity and building blocks to form mesoporous scaffolds, respectively (Section 2.1.2). Given the size of a PSII dimer (20 nm × 10 nm × 10 nm),[75] the benchmark IO-ITO electrode used 750 nm PS beads and commercial polydispersed ITO nanoparticles from Sigma Aldrich (10–120 nm; denoted as ITO-SA) to create ∼750 nm macropores and ∼150 nm wide channels for protein penetration, and mesoporosity for protein binding. Here I employed 750 nm and 3 μm PS beads to create different macropores: larger PS beads will give rise to larger macropores and interconnecting channels for protein penetration after burning off the PS template, but reduce the effective surface area for protein binding. To vary the mesostructure, I used polydispersed ITO nanoparticles (ITO-SA) and synthesised monodispersed ITO nanoparticles with average sizes of approximately 10 nm (ITO-10), 20 nm (ITO-20) and 40 nm (ITO-40) (**Figure 3.1**). Powder X-ray diffraction (XRD) analysis shows the synthesised ITO nanoparticles have the same cubic crystal structure with the commercial ITO (ITO-SA) (**Figure 3.2**). ITO-10 and ITO-20 nanoparticles have comparable dimension with PSII, whereas ITO-40 and ITO-SA nanoparticles are larger than the enzyme. The size differences resulted in different topographical features on their mesoporous films, which reflects different mesostructures in IO scaffolds (**Figure 3.3a**). The ITO-10 and ITO-20 films were uniform under the scan of atomic force microscope (AFM), whilst the ITO-40 and ITO-SA films exhibited a distinct granular texture that created large cavities to trap proteins. The contact angle measurements show similar hydrophilicity of the ITO nanoparticles (**Figure 3.3b**).

All the electrodes had a controlled film thickness of 20 μm and a geometrical area of 0.25 cm^2 (**Figure 3.4, 3.5**). The electrochemical properties of IO-ITO electrodes were characterised by CV. CV scans of IO-ITO electrodes showed a typical electrical double layer capacitive behaviour and no distinct redox waves appeared during the scan (**Figure 3.6a,b**), suggesting the electrochemical inertness of IO-ITO electrodes within the potential window of 0–0.5 V vs. SHE at pH 6.5. The structural complexity of the electrode scaffolds makes measuring the surface area technically intractable. Results from N_2 adsorption cannot represent the surface area available for charge transfer in an electrolyte solution due to interventions from surface wettability and mass transport. As the capacitance of an electrical

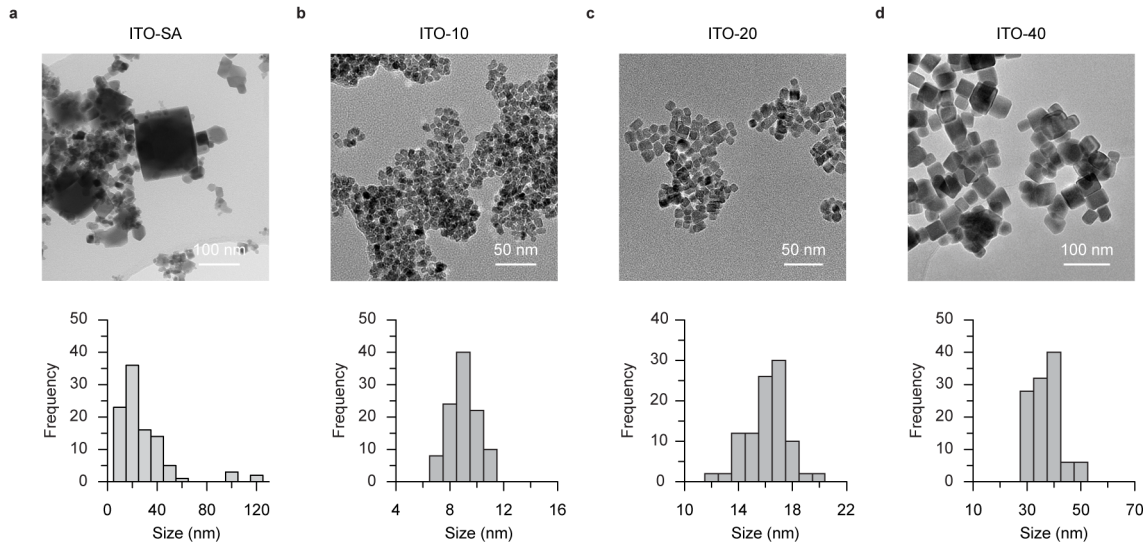

Figure 3.1 Morphology and size distribution of ITO nanoparticles. **a.** Commercial (Sigma-Aldrich) ITO nanoparticles. **b–d.** Synthesised ITO nanoparticles with average sizes of 10 nm, 20 nm and 40 nm respectively

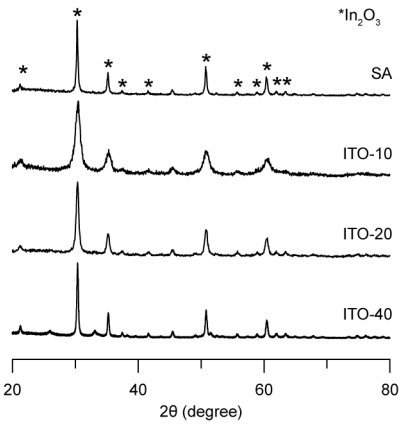

Figure 3.2 Powder XRD patterns of commercial (SA) and synthesised ITO nanoparticles

double layer capacitor scales proportionally with the electrochemically active surface area of electrode materials,[234] specific capacitance (*C*) was used as a measure of the surface area accessible to electrolyte solution.[122] The specific capacitance of IO-ITO electrodes decreased with increasing ITO particle size because smaller nanoparticles create higher surface area exposed to electrolyte solution (**Figure 3.8a**).

The optical transmission of the IO-ITO electrodes was measured by UV–vis spectroscopy (**Figure 3.6c,d**). The IO-ITO electrodes showed similar transmittance (< 4%) regardless of macro- and mesostructures (**Figure 3.8b**). Due to its high work function (> 4 eV), ITO has minimum light absorbance in the visible light spectrum, and therefore has been widely-used

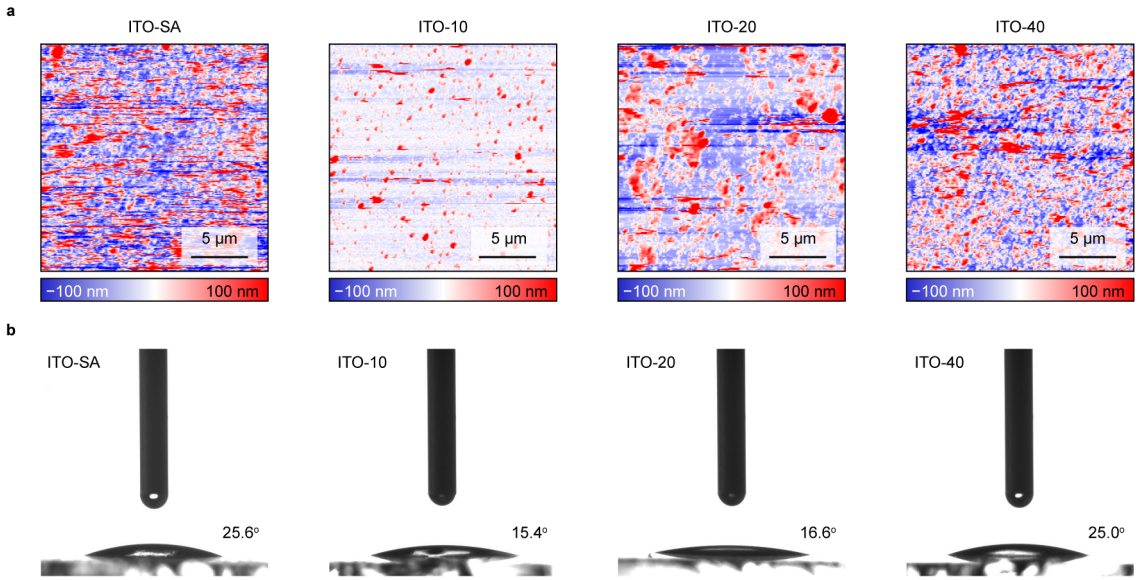

Figure 3.3 Morphology of the mesoporous ITO films made from different ITO nanoparticles. **a.** Atomic force microscopy (AFM) images of mesoporous ITO films formed by different ITO nanoparticles, which represents different mesostructures of the IO-ITO scaffolds. **b.** The contact angle of different mesoporous ITO films.

Figure 3.4 Photographs of IO-ITO electrodes (geometrical area: 0.25 cm^2).

for transparent electrodes.[235,236] Thus, most of the light was likely to penetrate within the 20 μm thick IO-ITO scaffold aided by strong internal scattering.[237,238] As the light intensity reaching the photoactive proteins in electrode scaffolds varies with the irradiation intensity

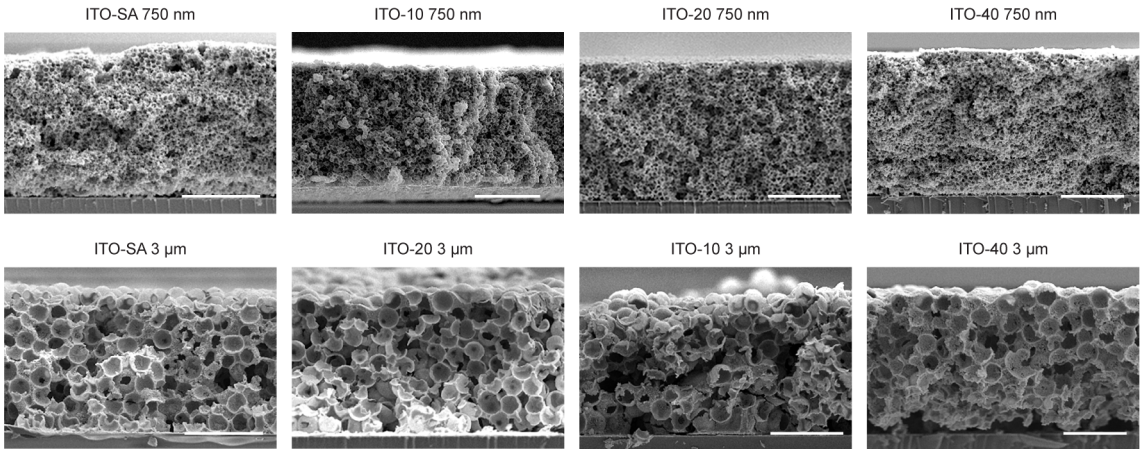

Figure 3.5 Cross-sectional SEM images of 20 µm thick IO-ITO electrodes. Scale bars: 10 µm.

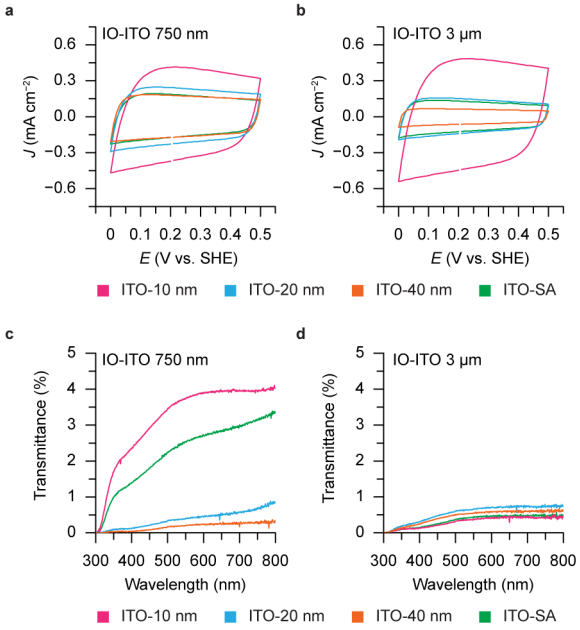

Figure 3.6 **a,b.** CV scans of 750 nm (**a**) and 3 µm (**b**) IO-ITO electrodes. **d,e.** UV–vis spectra of 750 nm (**d**) and 3 µm (**e**) IO-ITO electrodes (geometrical area: 0.25 cm^2).

and electrode thickness, photoactive protein films embedded deeper than 20 µm in electrodes are less accessible to irradiation, which minimises their contribution to the photocurrent.

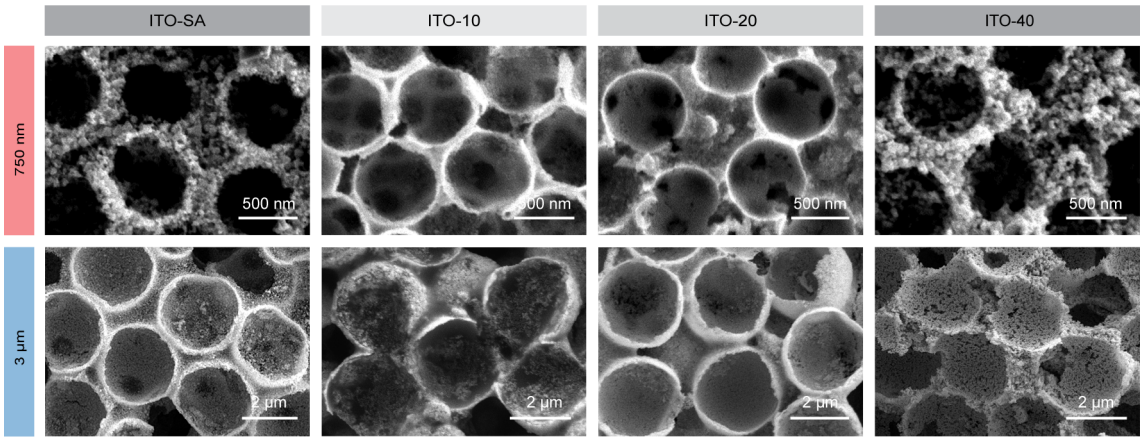

Figure 3.7 Structures of the IO-ITO electrodes. SEM images of 750 nm IO-ITO electrodes and 3 µm IO-ITO electrodes made with different ITO nanoparticles (ITO-SA, ITO-10, ITO-20, ITO-40).

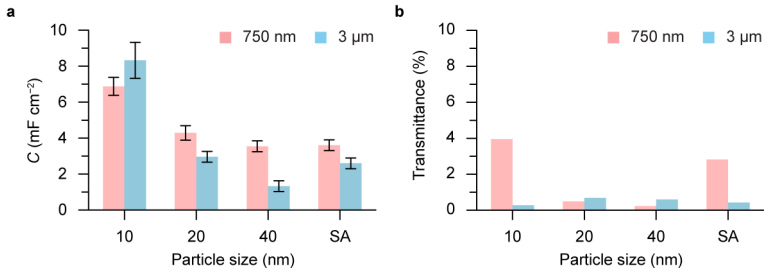

Figure 3.8 Electrochemical and optical properties of IO-ITO electrodes. **a.** Specific capacitance (C) of IO-ITO electrodes derived from CV scans (mean ± s.d., n = 3). **b.** Light transmittance at 665 nm of IO-ITO electrodes derived from UV–vis spectra.

3.3 Integration of photosystem II

PSII core complexes were isolated from the thermophilic cyanobacterium *Thermosynechococcus elongatus* due to their relative robustness and high oxygen evolution activity (Section 2.2.1).[103] Purified PSII was loaded on the IO-ITO electrodes by dropcasting and incubating in the dark for 15 min, followed by rinsing with the electrolyte solution to remove the weakly-bound PSII (Section 2.2.2). The appearance of the resulting PSII-loaded IO-ITO electrodes (IO-ITO|PSII) turned into green (**Figure 3.9**), indicating the impregnation of PSII within the electrode scaffolds. PSII monomers immobilised by electrodes were quantified by UV–vis analysis (Section 2.2.2). Both macro- and mesostructure affected PSII loading (**Figure 3.10a**). More PSII was retained in 750 nm electrodes than 3 µm ones. Although ITO-SA 750 nm and ITO-SA 3 µm electrodes had comparable specific capacitance, the PSII loading in 750 nm electrode was three times higher than that in 3 µm electrode, suggesting

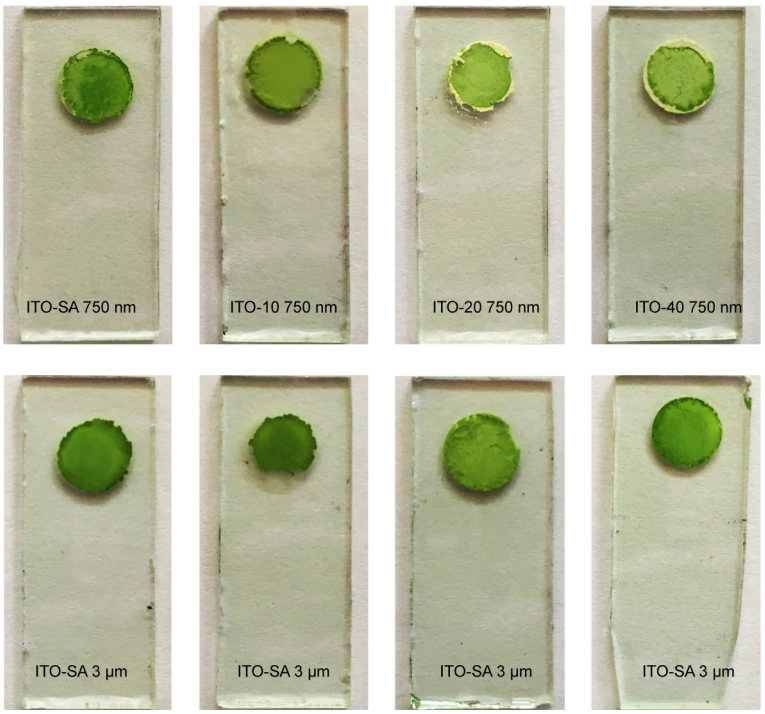

Figure 3.9 Photographs of the PSII-loaded IO-ITO electrodes. The appearance of the PSII-loaded IO-ITO electrodes turned into green, indicating the impregnation of PSII within the electrode scaffolds.

that the electrochemically-active surface area cannot be fully translated into the capacity for protein binding. With the same pore size, ITO-40 and ITO-SA electrodes achieved higher PSII loading, suggesting PSII was more likely trapped by the mesopores that were larger than the dimension of the protein. At the centre of electrode design for bioelectronics is creating large conductive surfaces to interface with redox-active proteins.[239] However, this well-known principle should be complemented by considering the footprint of protein and the resulting interaction with electrodes, so as to ensure the increased surface is accessible to proteins.

Despite diverse hybrid electrodes developed for enzymatic water oxidation, PSII integration and distribution within electrodes has not been studied, which makes it difficult to evaluate the merit of electrode structures. Here, CLSM was employed to visualise the spatial distribution of PSII within the electrode scaffolds by its strongly fluorescent chlorophyll *a* molecules. CLSM is a powerful technique to image biofilms through inherent or artificial fluorescent labels, which allows for optical imaging of biofilms embedded in complex architectures that would otherwise be difficult for physical sectioning.[188,198,211] Three control experiments were performed to rule out possible artefacts arising from light

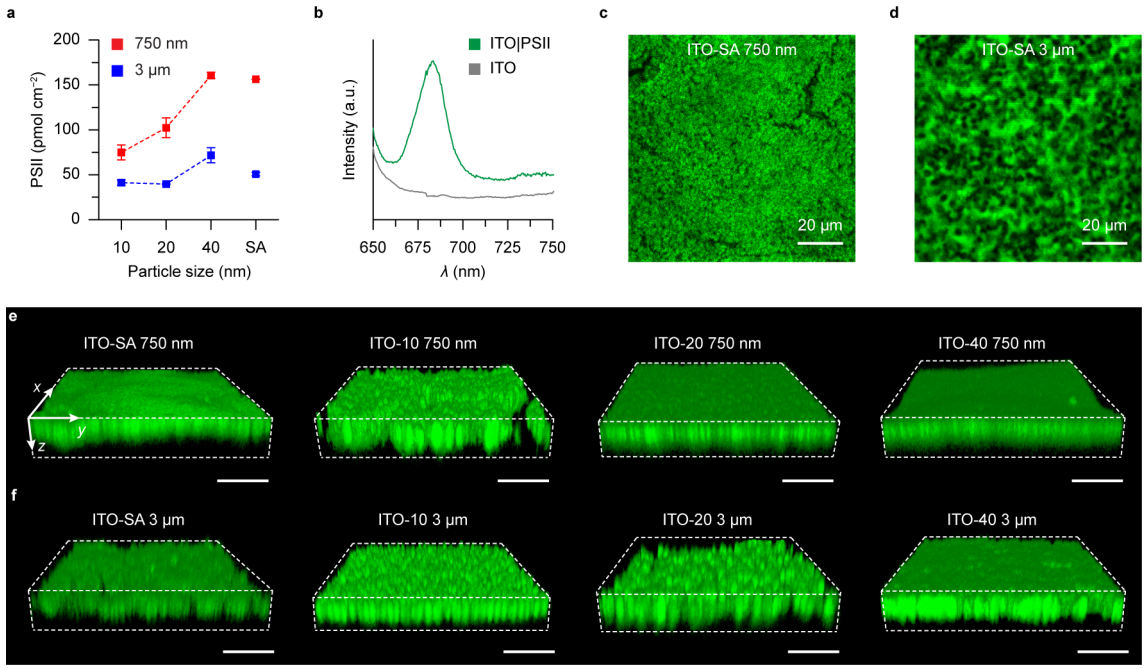

Figure 3.10 PSII integration within the IO-ITO electrodes. **a.** PSII (monomer) loadings on IO-ITO electrodes obtained from UV–vis analysis (mean ± s.d., $n = 3$). **b.** Fluorescence emission spectra of a bare and an IO-ITO|PSII electrode (ITO-SA 3 µm). The maximum intensity at 680 nm is derived from chlorophyll *a* in PSII. **c,d.** CLSM images of the PSII in ITO-SA 750 nm (**c**) and ITO-SA 3 µm (**d**) electrodes. **e,f.** 3D visualisation of the PSII distribution within ITO-750 nm (**e**) and ITO-3 µm (**f**) electrodes. The 3D view was reconstructed from *z*-stacking images that were acquired by scanning 20 µm downwards from the electrode surface. Each electrode (0.25 cm^2) was dropcast with 80 pmol of PSII monomers. Excitation: λ_{ex} = 633 nm; Emission: λ_{em} = 650–750 nm. Scale bars in **e,f**: 20 µm.

scattering or substrate interference. First, fluorescence spectra of IO-ITO|PSII electrodes showed a maximum intensity around 680 nm which agrees with that of PSII and chlorophyll *a* (**Figure 3.10b**).[103] Second, CLSM images show only the presence of PSII could produce fluorescence. Moreover, by varying the filter, we acquired images at a span of every 10 nm from 650 nm to 750 nm and their intensity changed in accordance with the fluorescence spectrum (**Figure 3.11a**), confirming the fluorescence only stemmed from PSII without the interference from artefacts. Third, IO-ITO electrodes were impregnated with excess Rhodamine B solution for CLSM imaging. Fluorescence emitted by Rhodamine B (500–600 nm) could be imaged regardless of the depth of the focal planes in electrodes (**Figure 3.11b**), which shows that the fluorescence intensity can be used as a qualitative reflection of the protein population in the electrode scaffolds.

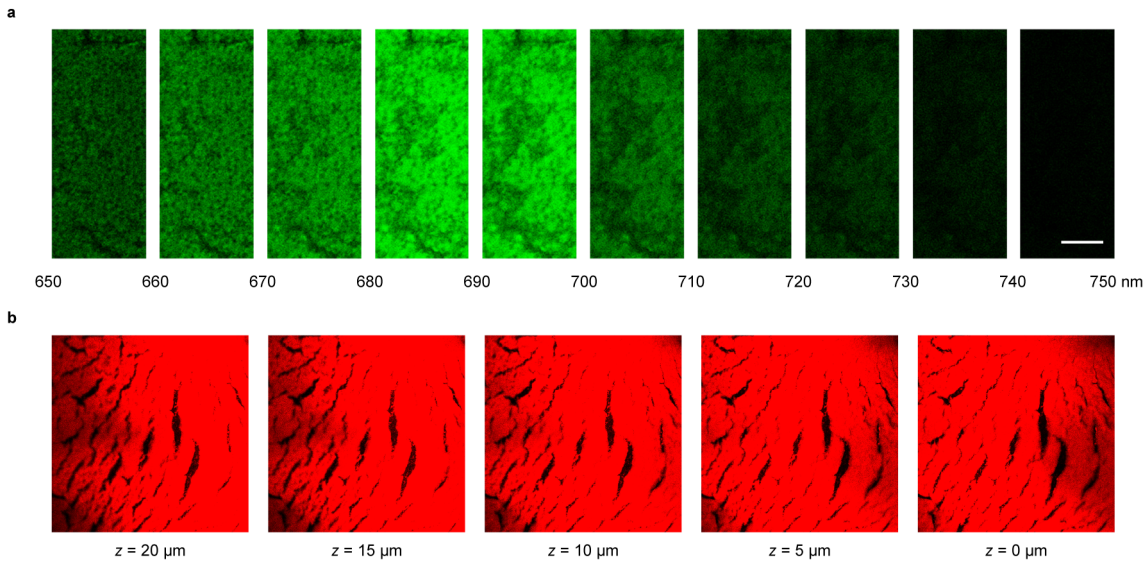

Figure 3.11 Control experiments for CLSM imaging of IO-ITO|PSII electrodes. **a.** CLSM images of an IO-ITO|PSII hybrid electrode of varying fluorescence wavelengths. It shows that the fluorescence intensity varied according to the fluorescence spectra of PSII. Excitation: λ_{ex} = 633 nm. Scale bar: 100 µm. **b.** CLSM images of an IO-ITO electrode (ITO-SA 750 nm) dropcast with 5 µL of Rhodamine B solution (0.1 mg mL^{-1} in ethanol). Fluorescence emitted by Rhodamine B could be imaged regardless of the depth of the focal planes in electrodes, which shows that the fluorescence intensity can qualitatively reflect the protein population in electrode scaffolds. Excitation: λ_{ex} = 561 nm; Fluorescence: λ_{em} = 500–600 nm. A surface area of 1160 µm × 1160 µm (1.35 mm^2) was captured. z = 0 indicates the surface of an electrode.

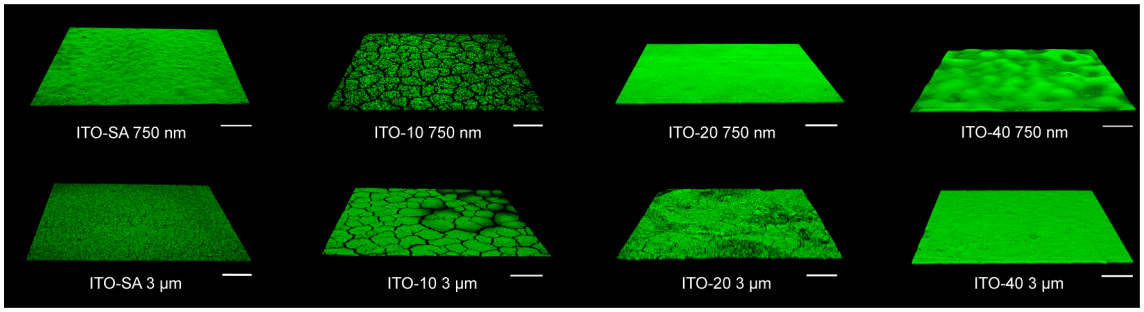

Figure 3.12 3D visualisation of the PSII distribution in IO-ITO electrodes. A surface area of 1160 µm × 1160 µm (1.35 mm^2) was captured for each electrode. z-stacking images were acquired by scanning 20 µm downward from the electrode surface to include the entire electrode scaffold. Excitation: λ_{ex} = 633 nm; Fluorescence: λ_{em} = 650–750 nm. Scale bars: 200 µm.

The morphology of PSII films reflects the macroscale structural features of electrodes such as macroporosity and cracks (**Figure 3.12**). PSII uniformly distributed in 750 nm IO-ITO

electrodes, whereas formed aggregates in 3 µm IO-ITO electrodes (**Figure 3.10c,d**). In both cases, PSII can penetrate throughout the entire IO-ITO scaffold via channels interconnecting macropores (**Figure 3.10e,f**). The depth profile of fluorescence indicates that most PSII populated in the middle range of the electrode scaffold (**Figure 3.13**). Although the light intensity will decay along the electrode depth, the light scattering within the electrode will likely enable most PSII to access irradiation.

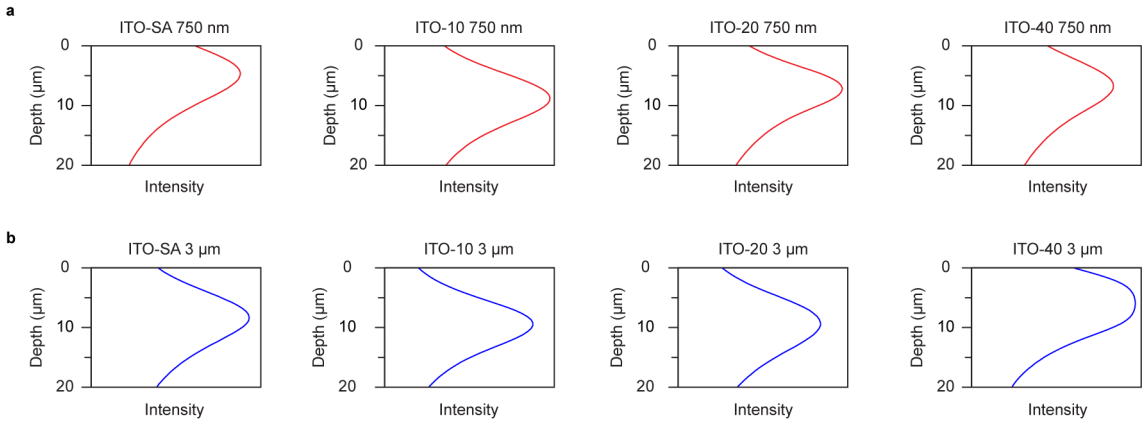

Figure 3.13 Integrated fluorescence intensity over the z-axis of the IO-ITO|PSII electrodes. Zero depth ($z = 0$) indicates the electrode surface. The fluorescence intensity was integrated from the relative fluorescence yield at each focal plane.

The protein-electrode interaction was further investigated from a dynamic perspective, by monitoring the process of protein adsorption and desorption within the electrode scaffold. This was possible by employing in situ ATR-IR spectroscopy to track the PSII penetration within the IO-ITO scaffolds. ATR-IR spectroscopy features its surface-sensitivity to molecular vibration and can indicate protein unfolding or denaturation through changes in its spectral bands.[222,240] The ATR-IR setup consisted of a 20 µm-thick IO-ITO scaffold deposited on a silicon prism (**Figure 1.12d, 3.14a**). As the evanescent IR wave will penetrate ~0.5 µm from the internal surface of the silicon prism,[241] the monitored spectral features of protein amide bands can only stem from PSII at the bottom layer of the IO-ITO scaffold. Hence, the dynamic adsorption process of PSII can be probed by its characteristic amide I and amide II bands centred at 1656 cm^{-1} and 1546 cm^{-1}, respectively.[220,240] The amide I band corresponds mainly to C=O stretching vibrations of the backbone peptide, whereas amide II originates from a combination of C–N stretching vibrations and N–H in-plane bending.[220,240] Compared with a PSII film deposited on a silicon prism, PSII adsorbed in IO-ITO electrodes displayed a slight shift in band positions, indicating a minor change in backbone conformations, possibly caused by the interaction with the mesoporous electron skeleton (**Figure 3.14b**).

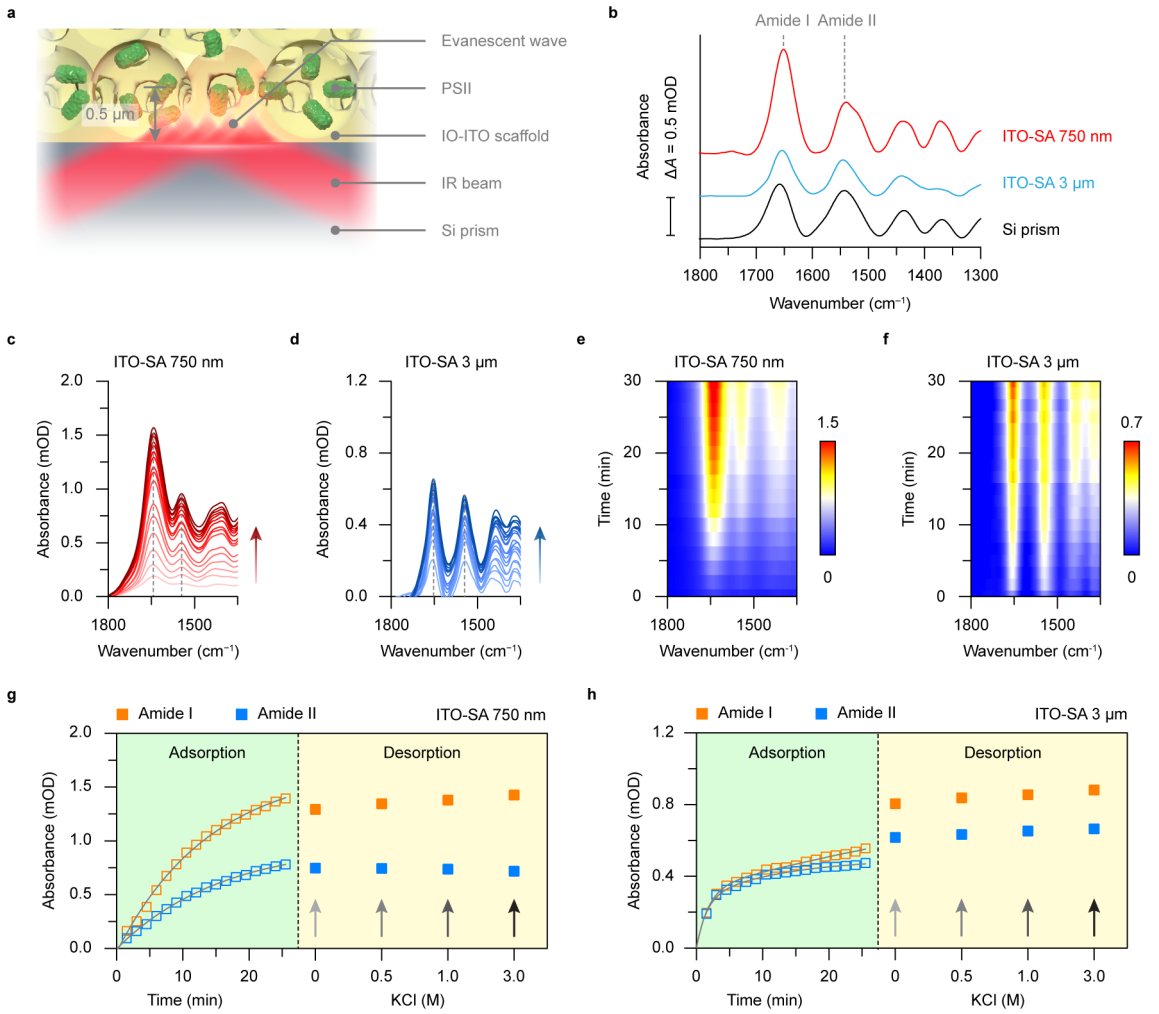

Figure 3.14 ATR-IR spectroscopy of PSII-loaded IO-ITO scaffolds. **a.** Schematic representation of the ATR-IR setup used in this study. **b.** ATR-IR spectra of the PSII film on the silicon prism, in ITO-SA 750 nm and ITO-SA 3 μm scaffolds. PSII adsorbed in IO-ITO scaffolds displayed similar amide band positions with that on the silicon prism, indicating a well-retained protein secondary structure when immobilised on electrodes. **c,d.** ATR-IR spectra of PSII adsorption at the bottom of ITO-SA 750 nm (**c**) and ITO-SA 3 μm (**d**) scaffolds. **e,f.** 2D visualisation of the position and intensity of amide bands during the PSII adsorption in ITO-SA 750 nm (**e**) and ITO-SA 3 μm (**f**) scaffolds. The colour bars indicate the IR absorbance (mOD). **g,h.** Adsorption kinetics and electrolyte-induced desorption of PSII loaded in ITO-SA 750 nm (**g**) and ITO-SA 3 μm (**h**) scaffolds. The PSII was desorbed by electrolyte buffer solutions containing different concentrations of KCl. The biexponential fitting is shown as grey lines in (**g**) and (**h**). Each electrode (0.25 cm^2) was dropcast with 80 pmol of PSII monomers.

The ATR-IR setup used here only detect proteins at the bottom layer of the IO-ITO scaffold where the IR evanescent wave can reach. Hence the protein penetration can be

tracked by the increasing band intensities over time. When PSII was dropcast on the IO-ITO scaffold, the growing intensities of both amide I and amide II bands indicated an increased amount of PSII reaching the bottom of the IO-ITO structure, confirming the penetration of PSII through the entire 20 µm-thick film (**Figure 3.14c,d**). Whilst positions of amide I and amide II bands remained unchanged during the PSII adsorption in both 750 nm and 3 µm IO-ITO scaffolds (**Figure 3.14e,f**), their intensity followed a biexponential increase consisting of a fast and a slow kinetic process (**Figure 3.14g,h**). The first exponential growth was completed after 15 min for 750 nm and 1.8 min for 3 µm electrodes, which shows that larger macropores favoured fast protein penetration within the electrode scaffold and further suggests that smaller macropores enable more mesoporous skeletons available for protein adsorption.

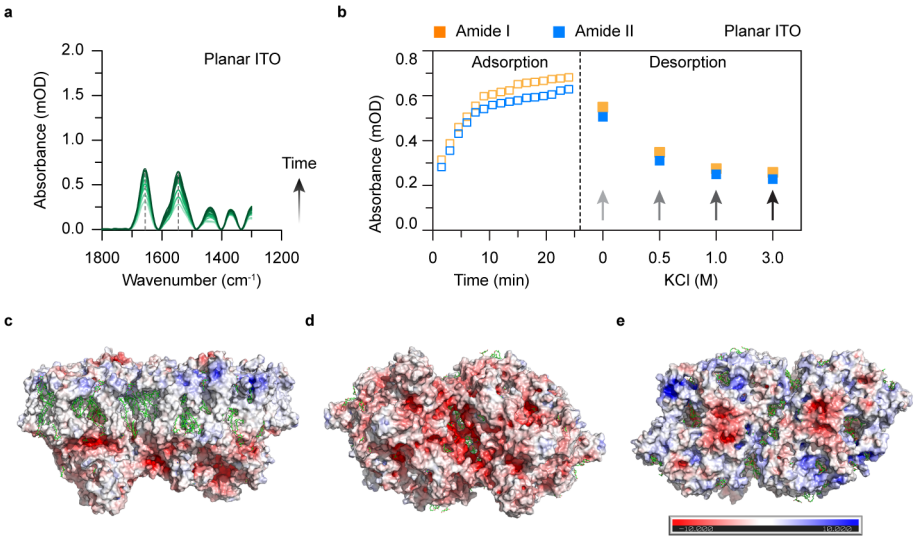

Figure 3.15 **a.** ATR-IR spectra of PSII adsorption on a planar ITO film (40 nm) sputtered on the silicon prism. **b.** Adsorption kinetics and desorption experiments of PSII on the surface of a planar ITO film demonstrated by the amide I and amide II band intensities derived from the ATR-IR spectra in **a**. The decrease of amide bands indicates that PSII on the planar ITO surface was desorbed by high ionic strength solutions, which suggests a dominating electrostatic interaction between between PSII and the ITO. **c–e.** The distribution of electrostatic potential of a PSII dimer (Protein Data Bank ID: 4ub6) from (**a**) side view, (**b**) bottom view from the lumen side and (**c**) top view from the stromal side. The electrostatic potential surface is generated by PyMOL with the adaptive Poisson-Boltzmann solver (ABPS) plugin. The red surfaces indicate the negative potential and the blue surfaces indicate the positive potential.

The nature of protein-electrode interaction was examined by a desorption experiment: the PSII-loaded IO-ITO scaffolds were washed with the PSII stock buffer solution (10% glycerol, 30 mM $MgCl_2$, 15 mM $CaCl_2$, 40 mM MES, pH 6.5) and buffer solutions with

increasing KCl concentrations (0.5 M, 1.0 M, 3.0 M). In the 750 nm IO-ITO scaffold, the desorption process caused only minor changes in the amide bands intensities (**Figure 3.14g**), suggesting PSII was well retained within the scaffold. In contrast, the amide bands increased steadily with KCl concentrations in the 3 μm IO-ITO scaffold (**Figure 3.14h**), indicating that an increased amount of PSII was desorbed from the scaffold by high ionic strength solutions and penetrated deeper into the IO scaffold thereafter. The difference in protein desorption can be attributed to the macroporosity, where desorbed proteins are more likely to be recaptured by the 750 nm IO-ITO scaffold but diffuse to the bottom in the 3 μm IO-ITO scaffold. The protein desorption induced by the high ionic strength solutions can be further verified by a desorption experiment on a planar ITO surface that eliminated the impact from hierarchical structure. Most PSII adsorbed on the ITO surface was removed by a concentrated saline solution, which points to a dominating electrostatic interaction between PSII and the IO-ITO scaffold (**Figure 3.15a,b**). The positive charge of ITO nanoparticles (ζ-potential: + 32 mV at pH 6.5) enables PSII to interact with the IO-ITO scaffold via its negatively charged surfaces (**Figure 3.15c–e**). The PSII-ITO interaction is different with what has been reported between FDH and TiO_2, where 60–70% of FDH remained adsorbed on the TiO_2 surface after multiple rinsing, suggesting a substantial contribution from chemisorption.[222]

3.4 Protein-film photoelectrochemistry

The photoactivity of IO-ITO|PSII electrodes was quantified by PF-PEC (**Figure 3.16, Table 3.1**). DET photocurrent of IO-ITO electrodes correlated broadly with the PSII loading, except for ITO-40 750 nm that underperformed in DET compared with the ITO-SA 750 nm electrode (**Figure 3.17a**). This may be due to thick PSII films that were inadequately wired by the conductive scaffold in ITO-40 750 nm and monodispersed ITO-40 nanoparticles that formed less contact sites with PSII compared with polydispersed ITO-SA nanoparticles. This problem was mitigated by introducing a diffusional redox mediator (DCBQ) that can shuttle electrons from proteins to the electrode, regardless of aggregates and orientation. Both ITO-40 and ITO-SA 750 nm electrodes showed a comparable MET photocurrent (**Figure 3.17a**). The MET photocurrent of 750 nm IO-ITO electrodes increased proportionally with the PSII loading, whereas that of 3 μm IO-ITO electrodes showed a major deviation from the PSII loadings, which may result from different mediator transport within protein films in different electrodes (**Figure 3.17a**).

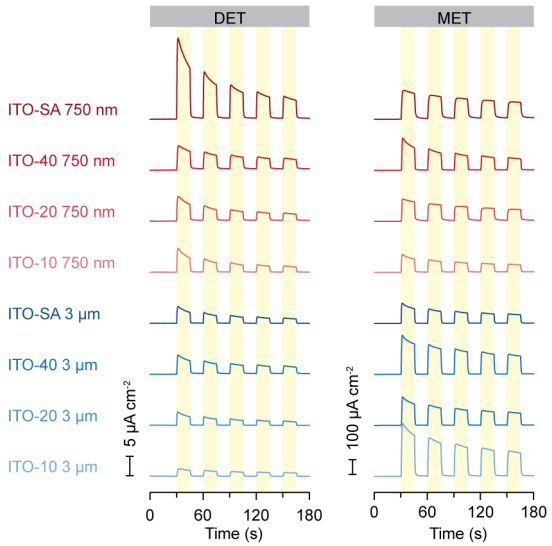

Figure 3.16 Representative photocurrent traces of DET and MET of IO-ITO|PSII electrodes. The photocurrent (corrected with the baseline in the dark) at the end of the third irradiation was used for comparison and to calculate the TOF. 85 pmol of PS II monomers were dropcast on each electrode (geometrical area: 0.25 cm^2) and incubated in air for 15 min in the dark. Conditions: λ = 685 nm, I = 10 mW cm^{-2}, E = 0.5 V vs. SHE, DCBQ (1 mM for MET), 25 °C.

Table 3.1 Summary of PF-PEC measurements of IO-ITO electrodes. 85 pmol of PS II monomers were dropcast on each electrode (geometrical area: 0.25 cm^2) and incubated in air for 15 min in the dark. TOFs were calculated assuming 100% Faraday efficiency of oxygen evolution.

Electrode	Thickness	PSII loading	J (µA cm^{-2})		TOF (s^{-1})	
	(µm)	(pmol cm^{-2})	DET	MET	DET	MET
ITO-SA 750 nm	19.7 ± 1.0	156.4 ± 0.2	5.9 ± 0.5	151.1 ± 1.8	0.10 ± 0.01	2.50 ± 0.03
ITO-10 750 nm	20.2 ± 1.6	74.9 ± 8.3	1.8 ± 0.1	94.2 ± 26.5	0.06 ± 0.01	3.20 ± 0.56
ITO-20 750 nm	19.4 ± 0.9	102.3 ± 11.0	2.1 ± 0.1	108.5 ± 9.2	0.05 ± 0.01	2.81 ± 0.53
ITO-40 750 nm	21.0 ± 0.4	160.6 ± 3.4	3.0 ± 0.2	165.2 ± 24.9	0.05 ± 0.01	2.67 ± 0.46
ITO-SA 3 µm	19.5 ± 0.2	50.7 ± 1.9	1.4 ± 0.2	53.6 ± 5.3	0.07 ± 0.01	2.73 ± 0.17
ITO-10 3 µm	20.8 ± 0.9	41.2 ± 3.1	1.0 ± 0.0	114.3 ± 13.3	0.06 ± 0.01	7.17 ± 0.30
ITO-20 3 µm	19.4 ± 2.0	39.7 ± 0.3	1.3 ± 0.1	78.0 ± 12.3	0.09 ± 0.01	5.10 ± 0.85
ITO-40 3 µm	20.5 ± 0.4	71.7 ± 8.4	2.2 ± 0.1	84.4 ± 10.6	0.08 ± 0.01	3.05 ± 0.02

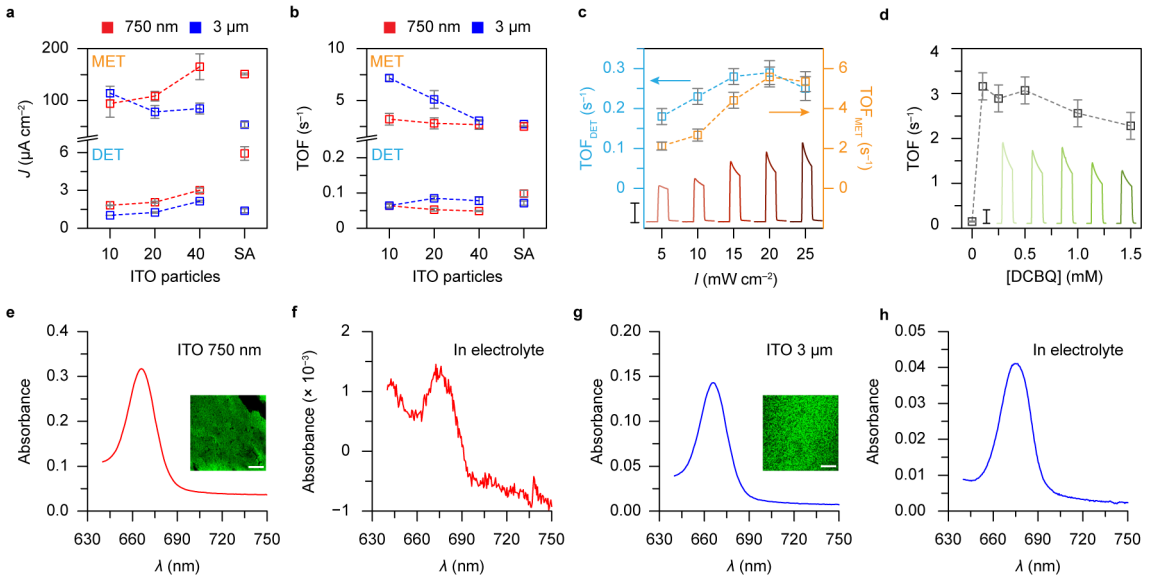

Figure 3.17 PF-PEC performance of IO-ITO|PSII electrodes. **a,b.** Photocurrent (**a**) and turnover frequencies (TOFs) (**b**) of PSII-loaded IO-ITO electrodes (mean ± s.d., $n = 3$). **c.** TOF dependence on light intensity for the ITO-SA 750 nm electrode (inset: representative DET photocurrent traces, scale bar: 5 µA cm^{-2}). **d.** TOF dependence on the concentration of DCBQ for the ITO-SA 750 nm electrode (inset: representative MET photocurrent traces, scale bar: 50 µA cm^{-2}). Conditions: M_{PSII} = 157 ± 7 pmol cm^{-2}, λ = 685 nm, I = 10 mW cm^{-2} (varied in **c**), E = 0.5 V vs. SHE, DCBQ (1 mM, for MET), 25 °C. **e–h.** UV–vis spectra of PSII immobilised on IO-ITO electrodes and PSII desorbed in the electrolyte solution. **e,f.** ITO-SA 750 nm: M_{PSII} (Electrode) = 224.4 pmol cm^{-2}; M_{PSII} (Electrolyte) = 1.8 pmol cm^{-2}. **g,h.**. ITO-SA 3 µm: M_{PSII} (Electrode) = 108.5 pmol cm^{-2}; M_{PSII} (Electrolyte) = 30.9 pmol cm^{-2}. The insets in **e,g** are CLSM images of the bioelectrodes after the PF-PEC measurement. Excitation: λ_{ex} = 633 nm; Fluorescence: λ_{em} = 650–750 nm. Scale bars: 100 µm. Note: UV–vis spectra in **e,g** were measured using methanol as the solvent. Thus, the maximal absorption peak (λ = 665 nm) differed with that measured in aqueous electrolyte (λ = 680 nm) (**f,h**).

The TOF is calculated based on the photocurrent density and protein loading of the electrode (assuming 100% of Faraday efficiency for water oxidation), which represents the average photoactivity of PSII integrated in the electrodes (**Figure 3.17b**). Despite large differences in photocurrent, 750 nm IO-ITO electrodes showed a similar TOF_{DET} of 0.07 ± 0.02 s^{-1}. The highest TOF_{DET} was achieved on the ITO-SA 750 nm electrode (0.10 ± 0.01 s^{-1}) (**Figure 3.17b**). As the MET current largely varied with the PSII loading for 750 nm IO-electrodes, TOF_{MET} of 750 nm electrodes remained close to 2.8 ± 0.5 s^{-1}, which suggests the individual activity of PSII was less affected by the mesostructure of electrodes. Likewise, 3 µm IO-ITO electrodes showed a TOF_{DET} of approximately 0.07 ± 0.01 s^{-1} (**Figure 3.17b**). The comparable TOF_{DET} for 750 nm and 3 µm IO-ITO electrodes despite

their significant differences in photocurrent and PSII loadings suggests that the enzymatic activity is not dominated by the electrode morphology. When enzymes are integrated into electrodes, their TOFs are typically much lower than the average activity of purified PSII used in this study (TOF: $\sim$20–30 s^{-1}), which indicates that most enzymes were not performing at their optimal rate.

One limitation is the light intensity reaching PSII in electrode scaffolds. Both TOF_{DET} and TOF_{MET} increased with irradiation intensity up to 20 mW cm^{-2} (**Figure 3.17c**). Further increase of the irradiation likely caused more photodamaging, which offset the enhancement of photoactivity and resulted in reduced photocurrents. Further possible limitations may reside in the insufficient wiring of proteins by the electrode scaffold, due to protein aggregation and random orientations. The adverse influence of protein orientation can be eliminated by modifying the surface chemistry of ITO to assist the electroactive orientation,[117] and by optimising the surface mesoporosity of the electrode scaffold to multiply the contact sites to the enzyme. We also find that TOF_{MET} would be affected by the mediator concentration, which may be due to the exogenous mediators quenching the excited antenna chlorophyll molecules (**Figure 3.17d**).[242,243]

After PF-PEC measurements, less than 1% of PSII was released from the 750 nm IO-ITO electrode, whereas 22% were desorbed into the electrolyte solution from the 3 μm IO-ITO electrode (**Figure 3.17e–h**), which is consistent with the results from ATR-IR spectroscopy that the 750 nm IO-ITO scaffold enabled better retention with PSII. Long-term chronoamperometry shows that the half-life of protein films inside the 750 nm IO-ITO electrode was $\sim$4 min, significantly longer than that on a flat ITO electrode (< 1 min), which manifests that the hierarchical structure is essential to secure the PSII within the electrode (**Figure 3.18a,b**). Lastly, I examined the ITO-SA 750 nm electrodes with different thicknesses. Despite having higher PSII loading, the 80 μm-thick IO-ITO electrode had similar DET photocurrent with 40 μm-thick electrode (**Figure 3.18c**). With the presence of diffusional mediators, the photocurrent correlated linearly with the electrode thickness (**Figure 3.18d**). Such difference in DET and MET reveals that PSII in thick scaffold was less inefficiently wired. TOFs for both DET and MET decreased with electrode thickness, which is consistent with previous results,[59,70] and reflects the impact of light penetration with the electrode scaffold.

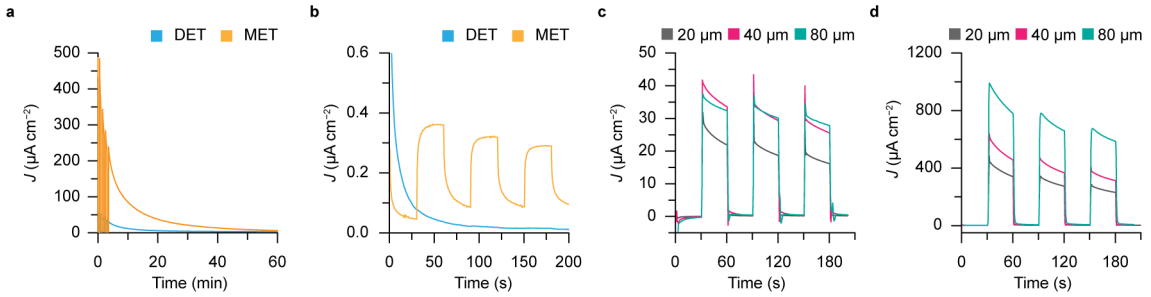

Figure 3.18 Longevity and thickness dependence of IO-ITO|PSII electrodes. **a,b.** Photocurrent traces of a PSII-loaded IO-ITO 750 nm electrode (**a**) and a flat ITO electrode (**b**). **c,d.** Photocurrent traces of PSII-loaded ITO-SA 750 nm electrodes with different thickness. **c.** DET. TOFs: ITO 20 μm, 0.27 s^{-1}; ITO 40 μm, 0.27 s^{-1}; ITO 80 μm, 0.10 s^{-1}. **d.** MET. TOFs: ITO 20 μm, 3.6 s^{-1}; ITO 40 μm, 1.7 s^{-1}; ITO 80 μm, 1.4 s^{-1}. Conditions: λ = 685 nm, I = 10 mW cm^{-2}, E = 0.5 V vs. SHE, DCBQ (1 mM for MET), 25 °C

3.5 Summary: structure-activity relationships

This chapter presents a systematic study on PSII-integrated IO-ITO electrodes to reveal structure-activity relationships underlying enzymatic catalysis in biohybrid electrodes: (1) the protein integration in an electrode scaffold will be determined both by material and morphology. IO-ITO electrodes with small macropores and large mesoporosity tend to bind most proteins by physical/electrostatic interactions; (2) DET photocurrent arising from electronic communication between electroactive proteins and electrode surfaces correlates with the protein loading in the electrode. The photoactivity of PSII is not sensitive to the electrode morphology, but will be governed by the light intensity and electronic communication at the biointerface; (3) MET photocurrent is convoluted by the interplay of protein loading and mediator diffusion within protein films and thus is dependent on the scaffold morphology. Overall, this study cements the ITO-SA 750 nm electrode as the benchmark platform for PF-PEC due to the following advantages (**Figure 3.19**): (1) the hierarchical IO architecture provides abundant conductive and hydrophilic mesoporous surfaces to secure proteins within the scaffold; (2) the polydispersed ITO nanoparticles create cavities with dimensions similar to PSII areal footprint and enable numerous contact sites to interface with the protein; (3) ITO has low light absorbance, thereby allowing high light transmission and internal scattering in the electrode scaffold.

Further studies are needed to elucidate the mass transport in protein films integrated in hierarchical electrode scaffolds. The PSII-ITO hybrid electrode represents a model system in enzymatic hybrid systems, and advances the current understanding of the protein-material interface and interaction underlying enzymatic catalysis in an artificial platform. In addition,

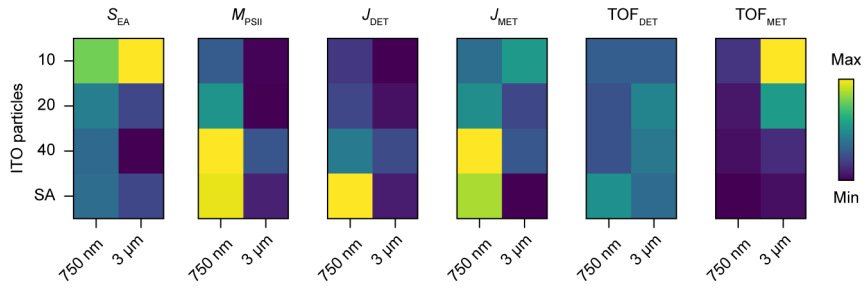

Figure 3.19 Comparison of different IO-ITO electrodes in surface area, PSII loading and photoelectrochemistry. The performance in each item is indicated by the colour bar.

this study employed an array of analytic techniques to probe the biotic-abiotic hybrid system, which could lend strengths to the ongoing research in semi-artificial photosynthesis.

Chapter 4

Interfacing photosystem II with inverse opal-graphene electrodes

The contents of this chapter have been published in a peer-reviewed article: Xin Fang, Katarzyna P. Sokol, Nina Heidary, Tarek A. Kandiel, Jenny Z. Zhang, Erwin Reisner, Nano. Lett.,* ***2019****, 19, 1844–1850. Results presented in this chapter were obtained solely by the author of this thesis.*

4.1 Introduction: graphene revisited

Graphene gains the reputation by its intrinsic properties: single layer graphene has a high specific surface area of 2630 m^2g^{-1}, high electron mobility of 200,000 $cm^2v^{-1}s^{-1}$, high Young's modulus of 10^{12} Pa, high thermal conductivity of 5,000 $Wm^{-1}K^{-1}$.[244] However, there are several misleading ambiguities that should be clarified here. First, these numbers are rarely achieved in reality because the properties of graphene vary enormously with its preparation methods. Graphene synthesised via chemical routes reluctantly approaches its benchmark properties that were often obtained from high-quality defect-less single-layer graphene produced from chemical vapour deposition (CVD). Another confusion stems from its nomenclature. In the beginning, the word "graphene" refers to monolayer two dimensional atomic crystals that are composed of sp^2 carbons, which underlines that its geometrical feature should be two dimensional single layer and chemical component should be exclusively carbon.[245] Yet the name graphene has been generalised to its analogues and derivatives such as GO, RGO and heteroatom-doped graphene. In this chapter, I followed a modified Hummer's method to prepare GO microsheets that were later reduced and assembled into

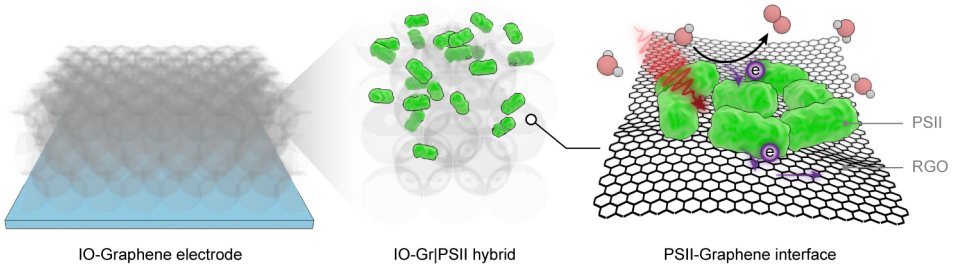

Figure 4.1 IO-graphene electrodes to interface with PSII.

an inverse opal structure. Though RGO differs with CVD-produced graphene in chemical components and physical properties, they bear the resemblance in two dimensional morphology. Therefore, I generally address the obtained electrodes as inverse opal-graphene (IO-Gr) electrodes.

Previous efforts to immobilise enzymes on electrodes highlight the importance of protein loading and electrical wiring at the interface.[239] Here, I developed inverse opal-graphene electrodes to interface with PSII in an attempt to gain understanding of how different materials can influence the enzymatic photocatalysis, by means of a side-by-side comparison with IO-ITO electrodes (**Figure 4.1**). Graphene-based materials, i.e., GO, RGO and heteroatom-doped graphene have been widely utilised to interface with enzymes such cytochromes, horseradish peroxidase and glucose oxidase for biosensing and electrocatalysis,[246–253] in view of their large biocompatible surface that binds proteins with high affinity. Such high surface area renders graphene sheets suitable as a public platform to mediate biotic and abiotic catalysts for cascade reactions,[254] which is akin to their role in artificial "Z-scheme" photocatalytic systems (**Figure 1.2c**).[23,255] In addition, they also bear a number of advantages that are appealing to photoelectrochemistry: (1) GO and RGO can be prepared in a large scale via wet chemistry;[256,257] (2) The surface chemistry (chemical components, surface charge and hydrophilicity etc) of graphene materials can be readily subjected to modifications by chemical or physical means,[258] which enables a versatile platform to study the protein-material interaction; (3) The structural plasticity allows for assembly of hierarchical architectures with various dimensions and morphologies, making electrode design and optimisation highly flexible.[259] (4) Previous spectroscopic studies suggest GO does not interfere with excitations occurring in PS II antenna complexes and therefore is potentially capable of extracting electrons from PS II, with efficiency comparable to the DCBQ-mediated electron transfer.[260]

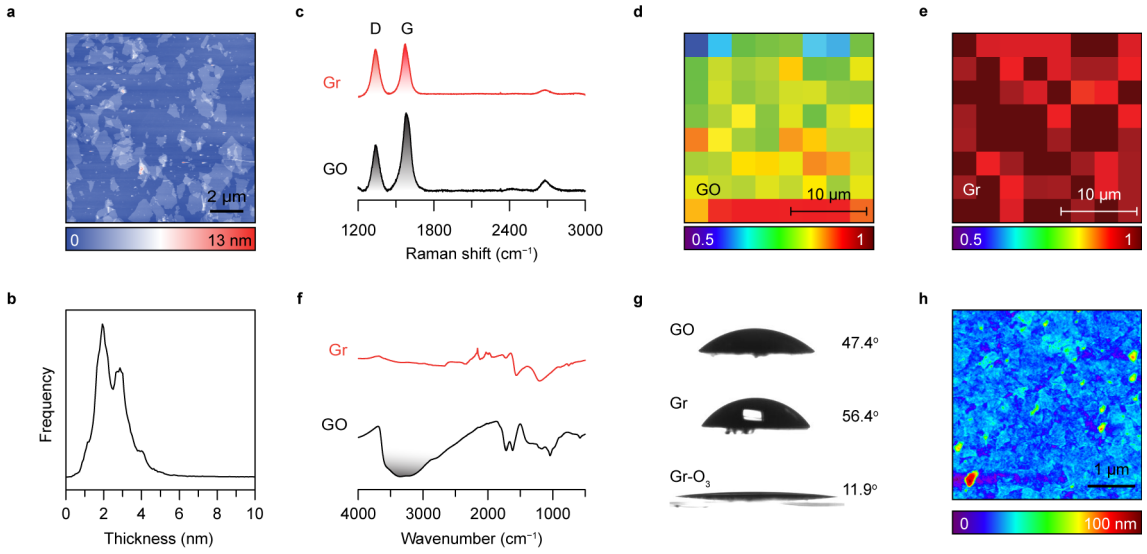

Figure 4.2 Preparation of IO-graphene electrodes. **a.** AFM image of GO sheets on a silicon wafer. **b.** Distribution of the thickness of GO. Most GO are less than 4 nm, corresponding to 1–4 layers of graphene sheets. **c–e.** Raman spectra (**c**) and Raman mapping images (**d,e**) of an IO-graphene electrode (Gr I-3 μm) and a GO film. The colour bar represents the intensity ratio between D band (~1350 cm^{-1}) and G band (~1580 cm^{-1}). The I_D/I_G increased after reduction, suggesting an increase in structural disorder arising from atomic arrangements. **f.** IR spectra of an IO-graphene electrode (Gr I-3 μm) and a GO film. Bands representing hydroxyl (~3400 cm^{-1}) and carbonyl (~1731 cm^{-1}) groups disappeared after thermal reduction. **g.** The contact angle of GO, thermally reduced graphene and ozone-treated (20 min) graphene films. The contact angle increased after thermal reduction due to the removal of hydrophilic oxygen groups pending on graphene basal planes. **h.** AFM image of the surface topography of a graphene film after thermal reduction.

4.2 Electrode structures and properties

Three-dimensional graphene electrodes can be fabricated by hydrothermal self-assembly from GO sheets or in situ growth on a template (e.g., Ni foams).[261–264] Hydrothermal self-assembly usually produces sponge-like graphene with pore size spanning from 1 to 100 μm, which is several orders of magnitude larger than the geometrical size of PS II.[265] The latter method allows for tailoring the porosity through templates, but entails high temperature (900–1000 °C) for thermolysis of gaseous carbon precursors (e.g., C_2H_4), which is incompatible of the ITO glass substrate.[266] In light of these limitations, here I prepared the inverse opal-graphene electrode through a templated self-assembly strategy (Section 2.1.3), which was performed at a lower temperature (500 °C) and yet attained a high degree of regularity.[267–270]

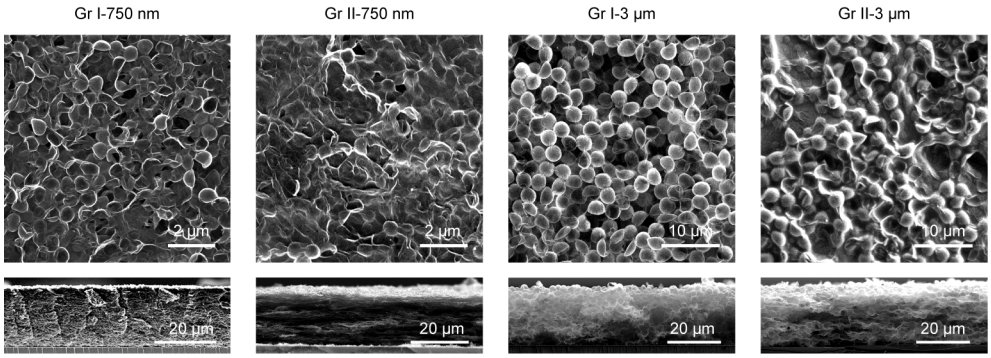

Figure 4.3 The morphology of IO-graphene electrodes. SEM images of the top and side view of the IO-graphene electrodes. All the electrodes have a controlled film thickness of 20 μm and a geometrical surface area of 0.25 cm^2.

GO was synthesised from graphite using a modified Hummer's method (Section 2.1.3).[226] The size of GO sheets ranged widely from submicro- to few micrometres (**Figure 4.2a**). The AFM scanning profiles show most GO sheets are 2–4 nm thick (**Figure 4.2b**). Given the thickness (∼1 nm) of a monolayer hydrated GO,[271] the synthesised GO comprised few layers of stacked graphene sheets. The IO-graphene electrodes were prepared by coassembling GO with PS beads. Then GO was thermally reduced into graphene (RGO) by annealing at 500 °C during which the PS template were decomposed forming macroporosity and oxygenic moieties pending on the GO surface were partially removed, thereby restoring conductivity.[272–274] Raman spectra and Raman mapping images show an increase of the intensity ratio between D (∼1350 cm^{-1}) band and G band (∼1580 cm^{-1}) after the thermal reduction, suggesting an increase in structural disorder arising from atomic arrangements (**Figure 4.2c–e**).[274,275] The alteration in chemical components was also reflected in IR spectra where bands representing hydroxyl (∼3400 cm^{-1}) and carbonyl (∼1731 cm^{-1}) groups disappeared (**Figure 4.2f**).[274] The contact angle also increased after thermal reduction due to the removal of hydrophilic oxygen groups on graphene basal planes (**Figure 4.2g**). The hydrophilicity of reduced GO can be improved by treating with ozone,[276] and afterwards the contact angle decreased from 56 ° to 12 °. The mesostructure of graphene electrodes is composed of multilayer graphene sheets, which has less porosity and roughness compared to their ITO counterparts (**Figure 4.2h**).

The structure of IO-graphene electrodes is tunable by varying the size of PS beads (750 nm and 3 μm) and the concentration of GO solutions (Gr I: 4 mg mL^{-1} and Gr II: 10 mg mL^{-1}). Four IO-graphene electrodes were prepared: Gr I-750 nm, Gr II-750 nm, Gr I-3 μm and Gr II-3 μm (**Figure 4.3**). All the electrodes have a controlled thickness of 20 μm and a geometrical area of 0.25 cm^2. In IO-graphene electrodes, the PS beads dictate the

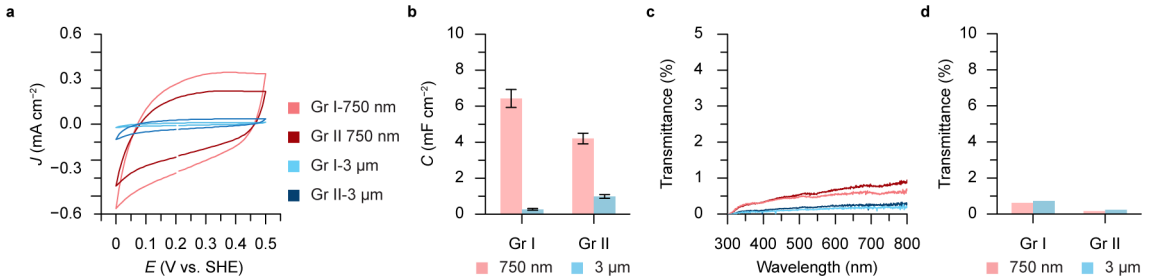

Figure 4.4 Electrochemical and optical properties of IO-graphene electrodes. **a.** CV scans. **b.** Specific capacitance (*C*). CV was performed in air at 25 °C at a scan rate of 50 mV s^{-1} in a pH 6.5 electrolyte solution containing MES (40 mM), $CaCl_2$ (20 mM), and glycerol (5%). Pt and Ag/AgCl electrodes were used as counter and reference electrodes, respectively. IO-graphene electrodes were treated with ozone for 20 min before the measurements. **c.** UV–vis spectra. **d.** Light transmittance at 665 nm.

macroporosity, whereas the concentration of the GO solution mainly affects the surface area and pathways for enzyme penetration. More graphene sheets provide higher surface area for protein binding, but may also block channels for protein integration and attenuate the light intensity. The major morphological difference with ITO counterparts is that macropores in IO-graphene electrodes were not interconnected. Proteins therefore can only penetrate into the electrodes via channels created by thermal PS decomposition.

CV scans of IO-graphene electrodes deformed slightly from a rectangular shape, possibly due to a higher internal resistance and pseudocapacitive contribution (**Figure 4.4a**).[277] No distinct redox waves appeared during the scan, suggesting the electrochemical inertness of IO-graphene electrodes within the potential window (0–0.5 V vs. SHE, pH 6.5).[278] 750 nm IO-graphene electrodes had higher capacitance due to more graphene sheets available for ion adsorption in the electrolyte solution (**Figure 4.4b**). However, excess graphene sheets are likely to overlay the 750 nm pores due to comparable dimensions, and thus inhibit the solution infiltration. Macropores in Gr II-3 µm electrode are larger than graphene sheets and hence the more graphene sheets increased surface area rather than blocked the macropores. Because reduced GO is a strong absorber of visible light,[279] the light intensity will be attenuated when light transmits through the IO-graphene electrode, undermining the photoexcitation of enzymes therein (**Figure 4.4c,d**).

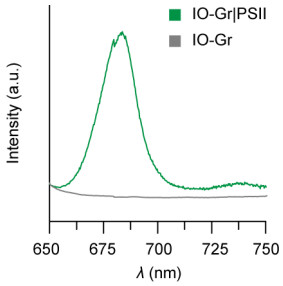

Figure 4.5 Fluorescence emission spectra of a bare and an IO-Gr|PSII electrode (Gr I-3 µm). The maximum intensity at 680 nm is derived from chlorophyll *a* in PSII.

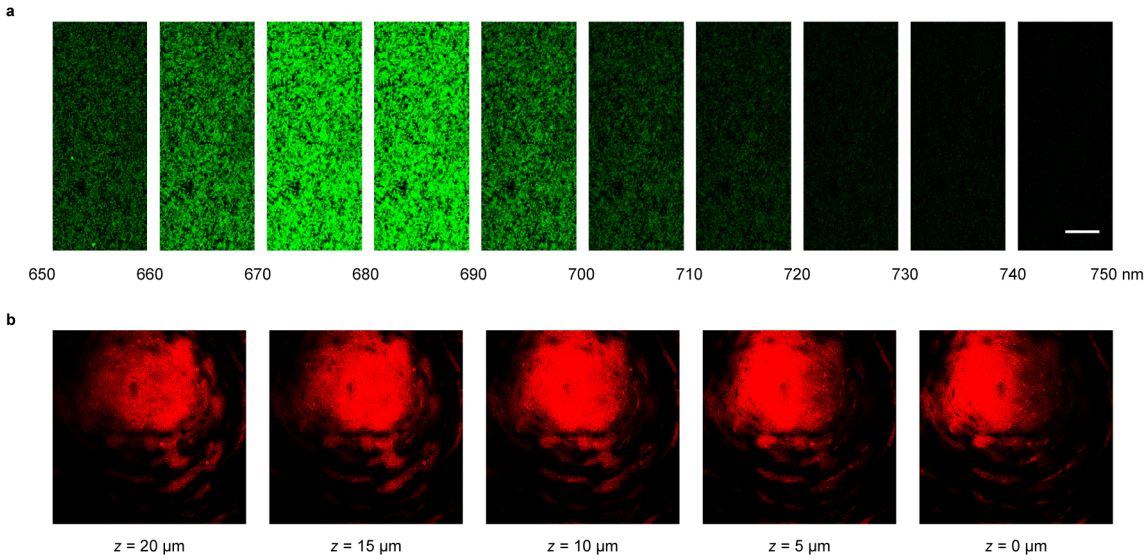

Figure 4.6 Control experiments for CLSM imaging of IO-Gr|PSII electrodes. **a.** CLSM images of varying fluorescence wavelengths. It shows that the fluorescence intensity varied according to the fluorescence spectra of PSII. Excitation: λ_{ex} = 633 nm. Scale bar: 100 µm. **b.** CLSM images of an IO-graphene electrode (Gr I-750 nm) dropcast with 5 µL of Rhodamine B solution (0.1 mg mL^{-1} in ethanol). Fluorescence emitted by Rhodamine B could be imaged regardless of the depth of the focal planes in electrodes, which shows that the fluorescence intensity can qualitatively reflect the protein population in electrode scaffolds. Excitation: λ_{ex} = 561 nm; Fluorescence: λ_{em} = 500–600 nm. A surface area of 1160 µm × 1160 µm (1.35 mm^2) was captured. z = 0 indicates the surface of an electrode.

4.3 Integration of photosystem II

Purified PSII was dropcast on IO-graphene electrodes in a similar manner. The appearance of PSII-loaded graphene electrodes barely changed due to the darkness of the graphene. The protein film inside the IO-graphene electrode was also visualised with CLSM by its strongly fluorescent chlorophyll *a* molecules. Control experiments were performed to rule out the

interference from artefacts (**Figure 4.5,4.6**). PSII films were not as uniformly distributed as in the IO-ITO electrode (**Figure 4.7**), which complicated the analysis of the protein film morphology in electrodes, but the amount of graphene had a distinct influence on the protein penetration. CLSM images show that the enzymes could penetrate through the IO-graphene electrodes except the Gr II-750 nm electrode, where most PSII accumulated near to the surface, due to excess graphene blocking pathways for protein penetration.

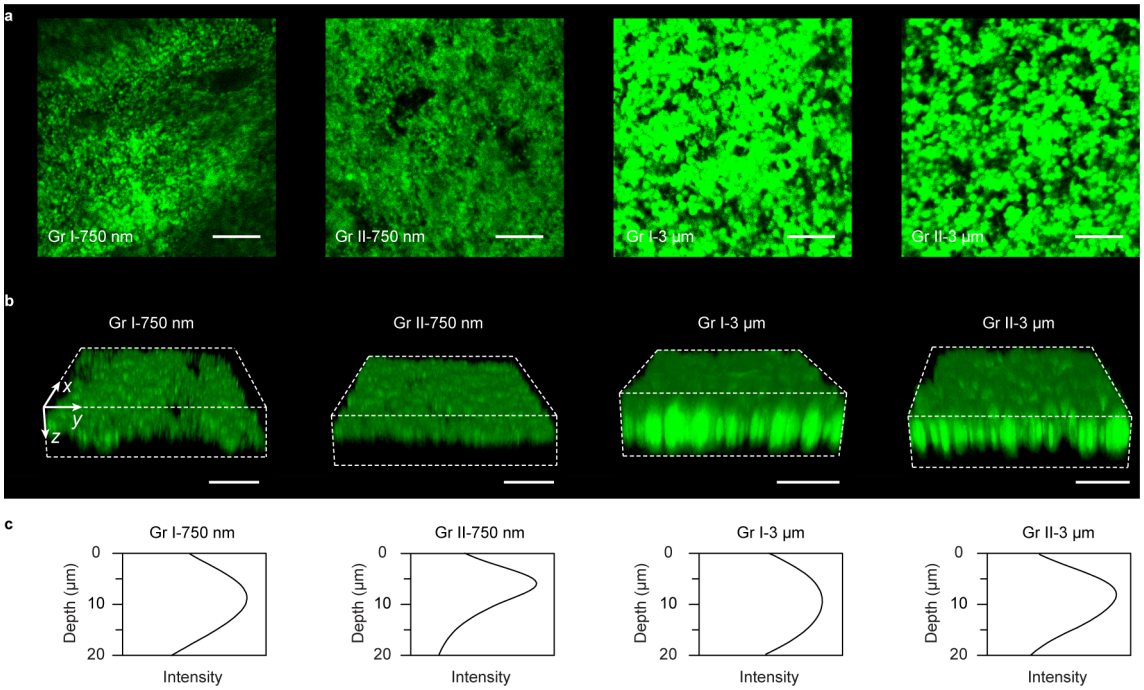

Figure 4.7 PSII distribution in IO-graphene electrodes. **a.** CLSM images of the IO-Gr|PSII electrodes. A surface area of 100 µm × 100 µm (0.01 mm^2) was captured for each electrode. **b.** 3D view of the PSII films in IO-graphene electrodes reconstructed from z-stacking images that were acquired by scanning 20 µm downward from the electrode surface. Excitation: λ_{ex} = 633 nm; Fluorescence: λ_{em} = 650–750 nm. Scale bars in **a**: 200 µm, in **b**: 20 µm. **c.** Integrated fluorescence intensity over the z-axis of the IO-Gr|PSII hybrid electrodes. Zero depth (z = 0) indicates the electrode surface. The fluorescence intensity was integrated from the relative fluorescence yield at each focal plane.

4.4 Protein-film photoelectrochemistry

IO-graphene electrodes had much lower capacity in binding PSII due to the lack of interconnected channels (**Figure 4.8a**). The Gr I-750 nm electrode has retained most PSII (∼34 pmol cm^{-2}) and increasing the graphene concentration (Gr II-750 nm) slightly decreased the

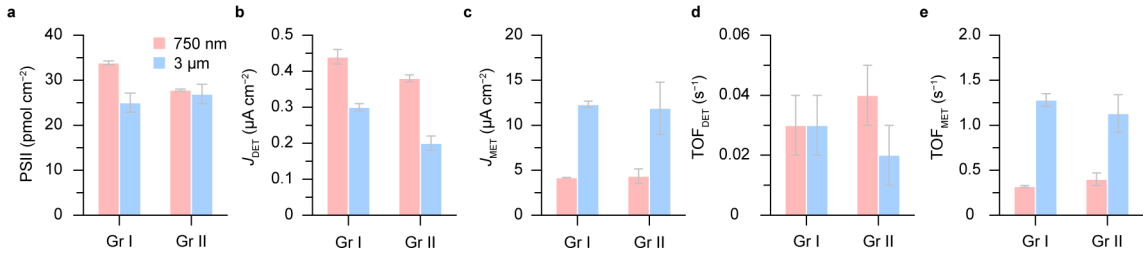

Figure 4.8 PF-PEC of IO-Gr|PSII hybrid electrodes. **a.** Loadings of PSII monomers on IO-graphene electrodes (mean ± s.d., n = 3). The amount of PSII monomers was quantified by UV–vis analysis. **b,c.** Photocurrent of DET (**b**) and MET (**c**). **d,e.** TOFs of DET (**d**) and MET (**e**). Conditions: λ = 685 nm, I = 10 mW cm^{-2}, E = 0.5 V (vs. SHE), DCBQ (1 mM for MET), 25 °C.

enzyme loading (∼28 pmol cm^{-2}). Despite different capacitance, Gr II-750 nm had similar PSII loading with Gr II-3 μm electrodes. This could be rationalised by their structural flaws that inhibited the protein penetration, making most enzymes bound by surfaces, regardless of the electrode porosity.

The DET photocurrent varied with PSII immobilised in electrodes, giving rise to similar TOFs (0.03 ± 0.01 s^{-1}) (**Figure 4.8b,d, Table 4.1**). With the presence of mediator (DCBQ), we found graphene electrodes with larger pores (Gr I-3 μm and Gr II-3 μm) generated much higher photocurrent and higher TOFs than that with smaller pores (Gr I-750 nm and G II-750 nm) (**Figure 4.8c,e**), though less PSII was immobilised. This is likely because large pores will favour the diffusion of mediators within the electrodes.

Table 4.1 Summary of PF-PEC measurements of IO-graphene and IO-ITO electrodes. 37 pmol of PS II monomers were dropcast on each electrode (geometrical area: 0.25 cm^2) and incubated in air for 15 min in the dark. TOFs were calculated assuming 100% Faraday efficiency of oxygen evolution.

Electrode	Thickness	PSII loading	J (µA cm^{-2})		TOF (s^{-1})	
	(µm)	(pmol cm^{-2})	DET	MET	DET	MET
Gr I-750 nm	19.5 ± 0.6	33.8 ± 0.4	0.4 ± 0.0	4.2 ± 0.0	0.03 ± 0.01	0.32 ± 0.01
Gr II-750 nm	21.1 ± 0.4	27.8 ± 0.2	0.4 ± 0.0	4.3 ± 0.8	0.04 ± 0.01	0.40 ± 0.07
Gr I-3 µm	20.1 ± 1.2	25.0 ± 2.1	0.3 ± 0.0	12.3 ± 0.37	0.03 ± 0.01	1.28 ± 0.07
Gr II-3 µm	21.6 ± 0.7	26.9 ± 2.2	0.2 ± 0.0	11.9 ± 2.9	0.02 ± 0.01	1.13 ± 0.21
ITO-SA 750 nm	19.7 ± 1.0	46.0 ± 1.3	1.4 ± 0.1	40.2 ± 0.9	0.01 ± 0.01	2.27 ± 0.02
ITO-SA 3 µm	19.5 ± 0.2	43.9 ± 2.6	1.0 ± 0.1	31.8 ± 2.7	0.06 ± 0.01	1.87 ± 0.07

Compared with their IO-ITO counterparts, PSII in IO-graphene electrodes exhibited less photoactivity (**Figure 4.9, Table 4.1**), which is likely due to the strong absorption of graphene sheets attenuating the light intensity reaching PSII. Moreover, graphene electrodes had less protein binding capacity, which can be attributed to their macrostructures that do not have sufficient interconnected channels for protein penetration and their mesostructures that lack topographical roughness to physically bind protein films. The nature of graphene-PSII interaction remains elusive and ATR-IR investigations were not successful due to that the vibrational signatures of GO overshadowed the amide bands of proteins. Graphene-based materials have been used to interface with PSI, the analogue of PSII,[280–282] and hydrophobic interaction has been suggested between PSI and the oxygenic groups on GO.[281] I thereby speculate PSII might preferably interact with the thermally-reduced GO through a similar fashion, which could be weaker than the electrostatic interaction taking place in IO-ITO electrodes.

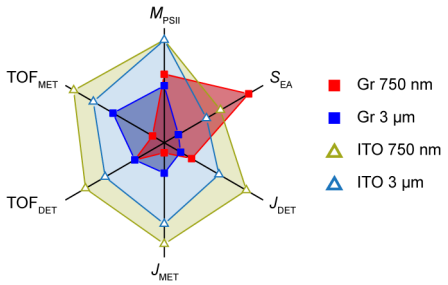

Figure 4.9 Itemised comparison between IO-graphene and IO-ITO electrodes in electrochemically-active surface area (S_{EA}, represented by specific capacitance), PSII loading (M_{PSII}), photocurrent (J) and TOFs of DET and MET.

4.5 Summary

Taking together, I have prepared an array of inverse opal graphene electrodes with different macroporosity. Interfacing PSII with these electrodes, a side-by-side comparison was conducted to reveal how electrode material and structure can influence the enzymatic photocatalysis. This chapter concludes that IO-ITO electrodes are superior to IO-graphene as platforms for photoactive bioelectrodes, because their material and structures are more favourable for protein integration and light penetration.

Chapter 5

Inverse opal-indium tin oxide electrode for microbial electrogenesis

The contents of this chapter were obtained solely by the author of this thesis, with contributions from others as outlined here: Dr. Shafeer Kalathil cultured the bacteria and performed the protein quantification and RNA extraction; Dr. Giorgio Divitini acquired the FIB-SEM images; ICP-OES analysis was conducted by Ms. Laura Healy. The RNA sequencing and data analysis was conducted by Cambridge Genomic Services (CGS).

5.1 Introduction

Interfacing the biocatalytic machinery of live cells with synthetic electrodes represents a cross-disciplinary approach for sustainable energy production and chemical synthesis.[57,130] While an array of biocatalysts are already being employed in synthetic chemistry,[283] microorganisms have demonstrated unrivalled synthetic potential due to sequences of well-tuned biosynthetic routes and the advancing techniques of synthetic biology, which allows selective synthesis of complex chemicals from the simplest feedstocks (e.g. CO_2, H_2O) under physiological conditions.[46,284] Of particular interest are electroactive bacteria such as *Geobacter* and *Shewanella* that have evolved unique mechanisms to discharge respiratory electrons by reducing insoluble Fe(III) or Mn(IV) oxides.[143] These bacteria can transport endogenous electrons across insulating and impermeable cell envelops to extracellular electron acceptors via outer membrane cyt *c*, conductive bacterial nanowires and/or self-secreted flavins.[154] Their ability to exchange electrons with inorganics via transmembrane electron conduits couples intracellular metabolism with extracellular redox transformations,[285,286] and per-

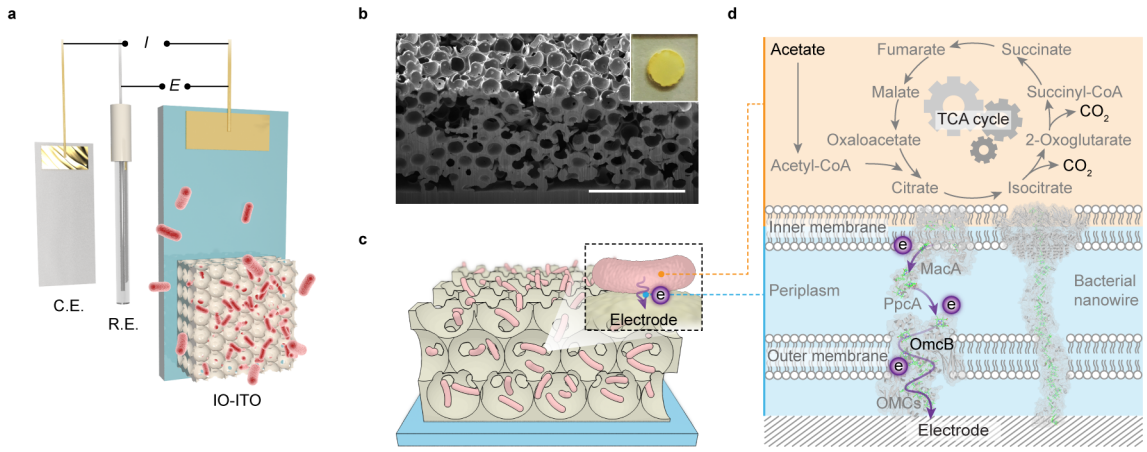

Figure 5.1 Schematic representation of microbial electrogenesis in the IO-ITO electrodes. **a.** An IO-ITO|*G. sulfurreducens* electrode is assembled into a three-electrode system with a counter electrode (C.E.) and a reference electrode (R.E.). **b.** SEM image of a bare IO-ITO electrode. Scale bar: 50 μm. The inset shows a photograph of the electrode ($S = 0.25$ cm^2). **c.** Schematic representation of a biohybrid electrode where *G. sulfurreducens* colonised on the IO-ITO scaffold. **d.** Extracellular electron transfer at the interface between *G. sulfurreducens* and an electrode. Acetate is metabolised into CO_2 via the intracellular TCA cycle and excess electrons are discharged to an external electrode via outer membrane cytochromes (OMCs).

mits a biohybrid system to exploit the biological metabolism via artificial electronics for electrogenesis and chemical synthesis.[146]

The biohybrid systems rely on electrodes that can host a colony of electroactive bacteria with intact metabolic pathways.[140] Electrodes also allow probing and controlling the bacteria's physiological functionality with electrochemical methodologies. Carbon-based electrodes, such as graphite and carbon cloth, are broadly applied in microbial fuel cells owing to their electrochemical stability, biocompatibility and structural plasticity (**Figure 1.11**).[184] Nevertheless, the architecture of these electrodes is not optimised for a large population of bacteria whilst ensuring effective diffusion of nutrients and dissipation of wastes. In addition, their hydrophobic surfaces are not conducive to electrical interaction with hydrophilic bacteria.[287] Therefore, sessile bacteria on such electrodes tend to form compact biofilms with sluggish electron transfer and inefficient mass transport, which engender adverse stresses limiting their proliferation and productivity.[175]

The hallmark of *G. sulfurreducens* is its current-producing capability in microbial fuel cells.[143] Its ability to metabolise organic pollutants and precipitate soluble heavy metals promises its applications in bioremediation.[165] Moreover, its complete genome sequence primes transcriptome analysis to probe its regulation strategies that maintain cellular homeostasis under various conditions.[148]

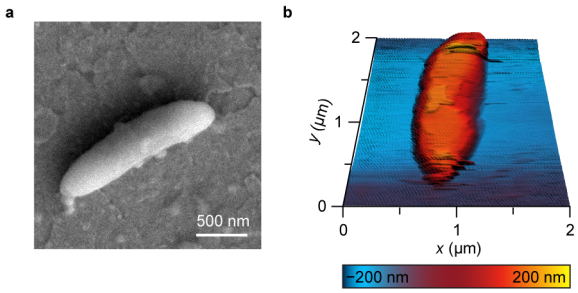

Figure 5.2 The microscopic morphology of *G. sulfurreducens*. **a.** SEM image. **b.** AFM image on a Si wafer.

In this chapter, I employed IO-ITO electrodes as a versatile platform for microbial electrogenesis (**Figure 5.1a**). ITO is hydrophilic and the porous architecture provided an easy access for bacteria penetration and colonisation (**Figure 5.1b,c**). When positive potentials were applied, planktonic *G. sulfurreducens* were immobilised from the medium solution. The sessile bacteria metabolised acetate to support its growth through the TCA cycle, while discharging excess electrons to the electrode via outer membrane cytochromes, which was registered as a continuous anodic current (**Figure 5.1d**). Transcriptome analysis by RNA sequencing revealed that *G. sulfurreducens* regulated gene expression in order to respire on electrodes. Furthermore, *S. loihica* was introduced together with *G. sulfurreducens* on the IO-ITO electrode to achieve syntrophic electrogenesis by linking their metabolic pathways, which would grant the system additional flexibility in using different electron donors.

5.2 Electrode structure

G. sulfurreducens exhibits a typical rod-shaped morphology with a length of 1.5–2 µm and diameter of 400–500 nm (**Figure 5.2**). IO-ITO electrodes were prepared by a coassembly method using 10 µm PS beads as the structural template and ITO nanoparticles (average size: 50 nm) as the electrode material to suit the dimension of *G. sulfurreducens* (Section 2.1.2). The resulting electrode features a hierarchical architecture with 8–10 µm macropores and mesoporous surface (**Figure 5.3a,b**). These macropores are interconnected by abundant channels formed during the course of template removal. The macroporosity is visualised by CLSM with Rhodamine B that was adsorbed on the scaffold (**Figure 5.3c**). The IO-ITO electrode was further characterised by X-ray microscopy and focused ion beam-scanning electron microscopy (FIB-SEM) with structural details in three dimensions, which demonstrated that the electrode scaffold enables a large surface and accessible pathways for bacteria

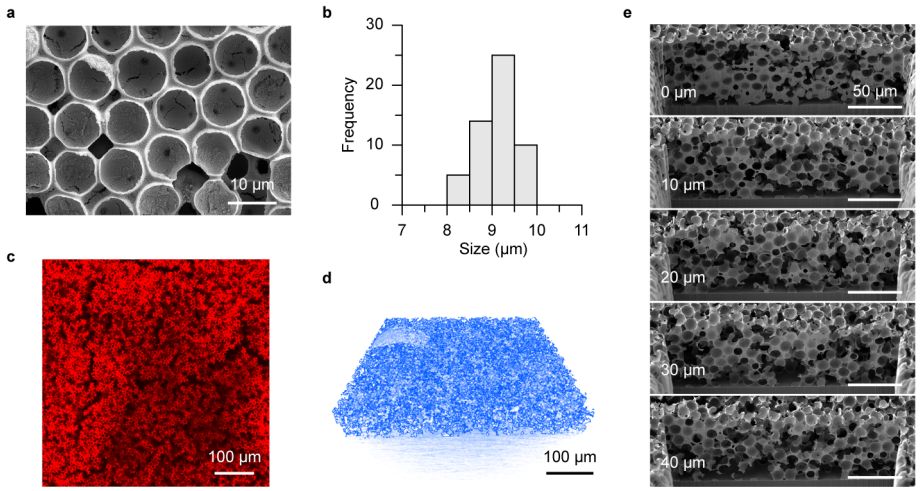

Figure 5.3 Structure of the IO-ITO electrode for microbial electrogenesis. **a.** Top-view SEM image. **b.** Histogram of the pore size distribution of the IO-ITO electrode. **c.** CLSM image of the IO-ITO electrode, showing channels that allow bacteria to penetrate. 20 µL of Rhodamine B solution (5 mM, in methanol) was dropcast on an IO-ITO electrode and dried in the dark. Excitation: λ_{ex} = 552 nm. Emission: λ_{em} = 590–640 nm. **d.** X-ray microscopy image of the interconnected IO-ITO scaffold (coloured in blue). **e.** Serial cross-sectional SEM images of the IO-ITO electrode acquired from FIB-SEM. Cross-sectional views of every 10 µm are displayed.

penetration and colonisation (**Figure 5.3d,e**). The IO-ITO electrode used in this study had a geometrical area of 0.25 cm^2 and a thickness of ∼60 µm (**Figure 5.1b**).

5.3 Microbial electrogenesis

G. sulfurreducens was cultured on an IO-ITO scaffold from the electrolyte solution by applying a potential of 0.1 V vs. SHE on the electrode. During this process, planktonic *G. sulfurreducens* landed on the electrode scaffold and metabolised acetate into CO_2 while discharging electrons to the electrode (**Figure 5.4a**). Bacteria then proliferated and progressively colonised the entire electrode, producing an increasing anodic current that plateaued at 3 mA cm^{-2} (500 mA cm^{-3}) after 80 h (**Figure 5.4b**). This current density represents a benchmark performance in microbial electrogenesis and approaches the volumetric current limit (1000 mA cm^{-3}) of a single bacterium.[213] Control experiments were conducted to determine the origin of the anodic current. First, heat-killed *G. sulfurreducens* produced the no current and its CV scan showed redox waves stemming from the electrolyte (**Figure 5.5a,b**). Moreover, the anodic current was partially reduced after the addition of malonic acid, which inhibits the succinic dehydrogenase in the TCA cycle (**Figure 5.5c**). The current production was

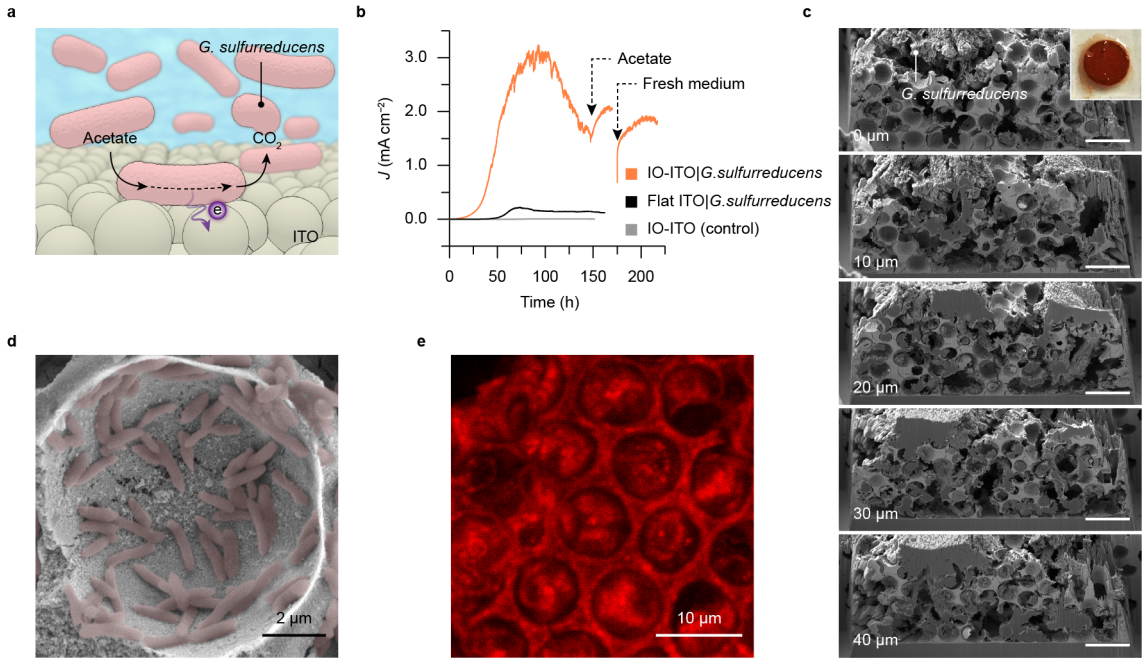

Figure 5.4 Microbial electrogenesis of *G. sulfurreducens* in IO-ITO electrodes. **a.** Schematic representation of microbial electrogenesis. *G. sulfurreducens* is respiring on an electrode surface with acetate as the electron donor whilst continuously releasing electrons to the electrode. **b.** A representative current of *G. sulfurreducens* respiring inside an IO-ITO electrode and a flat ITO electrode at 0.1 V vs. SHE with acetate (40 mM, pH 7.4). A bare IO-ITO electrode was used as a control. The two arrows indicate the addition of 40 mM acetate to the existing medium and the replenishing of a fresh medium containing 40 mM acetate, respectively. **c.** FIB-SEM images of an IO-ITO|*G. sulfurreducens* electrode prepared at 0.1 V vs. SHE for 80 h. Cross-sectional views of every 10 µm are displayed. Scale bar: 20 µm. The inset shows a photograph of the electrode (S = 0.25 cm^2). **d.** *G. sulfurreducens* (artificially coloured in red) attached on the surface of an IO-ITO electrode. **e.** CLSM images of an IO-ITO|*G. sulfurreducens* electrode. The electrode was stained with CTC (10 mM) and incubated in the dark for 30 min at 25 °C. Excitation: λ_{ex} = 488 nm; Emission: λ_{em} = 600–650 nm.

completely terminated by glutaraldehyde, a sterilant (**Figure 5.5d**). These in all confirm that the recorded current was exclusively derived from bacterial metabolism, making it a good proxy for bacteria's metabolic activity.

The high current density is attributed to the IO-ITO architecture, which compartmentalised bacteria colonies with conductive and hydrophilic scaffold, and thus allowed a large population of bacteria to actively metabolise therein. In addition, the hierarchical porosity enables efficient provision of electron donors (acetate) while effective dissipation of protons, thereby allowing for continual growth of bacteria. In contrast, *G. sulfurreducens* on a

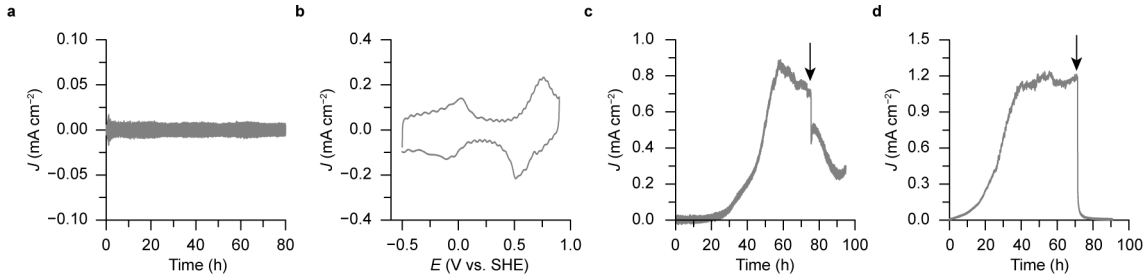

Figure 5.5 Control experiments of microbial electrogenesis. **a,b.** Chronoamperometry (**a**) and CV scan (**b**) of the IO-ITO electrode with inactivated *G. sulfurreducens*. *G. sulfurreducens* (OD 0.6) was inactivated by heating at 150 °C for 1 h in an autoclave. Conditions: E = 0.4 V vs. SHE, 40 mM acetate, pH 7.4; CV: scan rate: 5 mV s^{-1}, 30 °C, purged with N_2:CO_2 (80:20, v:v%). **c.** Effect of a metabolism inhibitor on *G. sulfurreducens*. The black arrow indicates the addition of malonic acid (10 mM) into the electrolyte solution. Malonic acid inhibits the TCA cycle and partially suppresses the metabolism of *G. sulfurreducens*. **d.** Effect of a biocide to *G. sulfurreducens*. The black arrow indicates the addition of glutaraldehyde (0.1%), a typical biocide, into the electrolyte solution. Conditions: E = 0.4 V vs. SHE, 40 mM acetate, pH 7.4, 30 °C, purged with N_2:CO_2 (80:20, v:v%).

flat ITO-coated glass gave rise to substantially less current (0.21 mA cm^{-2}) and therefore yielded a much thinner biofilm (< 5 µm) (**Figure 5.4b, 5.6a,b**). Likewise, the bacteria cannot penetrate into the IO-ITO electrodes with 3 µm pores, but formed thick biofilms on top of the electrode (**Figure 5.6c**). The presence of biofilms likely hindered the diffusion of acetate, limiting the availability of electron donors in the electrode scaffold, which could account for the resulting smaller plateau current. The current began to decay in the wake of acetate depletion, which can be partially restored by supplementing acetate into the current medium or replenishing with a fresh medium containing acetate (**Figure 5.4a**).

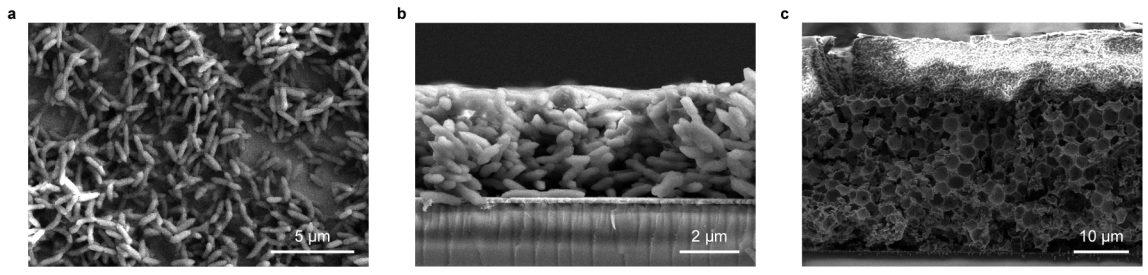

Figure 5.6 SEM images of the *G. sulfurreducens* on a flat ITO glass slide (**a**,**b**) and a 3 µm IO-ITO electrode (**c**). Conditions: E = 0.1 V vs. SHE, 40 mM acetate, pH 7.4, 30 °C, purged with N_2:CO_2 (80:20, v:v%).

The IO-ITO|*G. sulfurreducens* electrode after the anodic growth displayed a typical reddish colour stemming from the redox-active multihaem cyt *c* (**Figure 5.4c** inset). FIB-SEM imaging shows that the bacteria penetrated through the entire IO-ITO electrode and

were closely interfaced with the mesoporous scaffold (**Figure 5.4c,d**). As conventional fluorescent dyes (such as SYTO 9 and propidium iodide) adsorbed on the IO-ITO scaffold would be unable to differentiate between live and dead cells, I used an alternative dye to assess the bacterial viability. 5-cyano-2,3-ditolyl tetrazolium chloride (CTC) is a soluble non-fluorescent compound whereas its reduced form, CTC formazan, is insoluble and produces red fluorescence. Living bacteria respiring via the electron transport chain adsorb CTC dyes and reduce them into insoluble CTC formazan that precipitates in the cell. Dead bacteria and IO-ITO scaffolds cannot reduce CTC, thereby producing much less fluorescence.[288] This method allows us to assess the bacterial viability inside the IO-ITO electrode by means of evaluating their respiration activity, without being interfered by the scaffold. CLSM images manifest that bacterial viability of *G. sulfurreducens* was well-retained in the IO-ITO electrode scaffold (**Figure 5.4e, 5.7**).

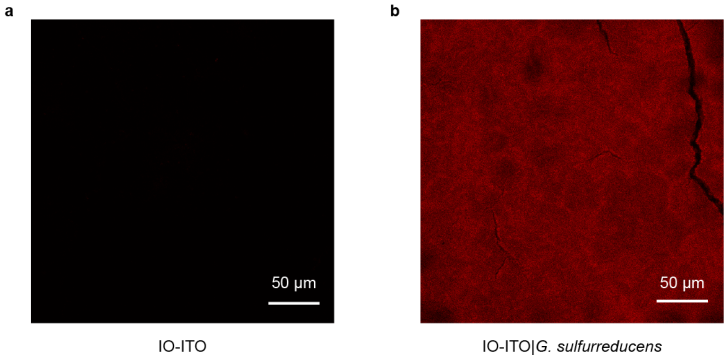

Figure 5.7 CLSM images of a bare IO-ITO electrode (**a**) and IO-ITO|*G. sulfurreducens* electrode (**b**). The electrodes were stained with 5-cyano-2,3-ditolyl tetrazolium chloride (CTC, 10 mM) and incubated in the dark for 30 min at 25 °C. Excitation: λ_{ex} = 488 nm; Emission: λ_{em} = 600–650 nm.

Under turnover conditions, the IO-ITO|*G. sulfurreducens* electrode exhibited a characteristic sigmoidal CV trace with an onset potential of −0.25 V vs. SHE (E_{CO_2/CH_3COO^-} = −0.29 V vs. SHE, pH 7.0) (**Figure 5.8a**).[182] The CV profile points to a typical catalytic response of a biofilm, where the catalytic current is limited by the extracellular electron transport via outer membrane cyt *c*.[289] This is further evidenced by a control experiment with cyt-suppressed *G. sulfurreducens* (ΔCyt). Instead of using genetic tools to create mutants with limited cytochrome expression, here we adopted a chemical approach to suppress the cytochrome synthesis by limiting the iron availability during growth.[232] This is possible because the synthesis of cyt *c* requires irons to constitute haem with protoporphyrin IX.[290] Microorganisms have developed regulatory and transport mechanisms to maintain iron homeostasis in response to variations in iron availability.[291,292] When culturing with bipyridine, an iron chelator, *G. sulfurreducens* limits the production of cytochromes under

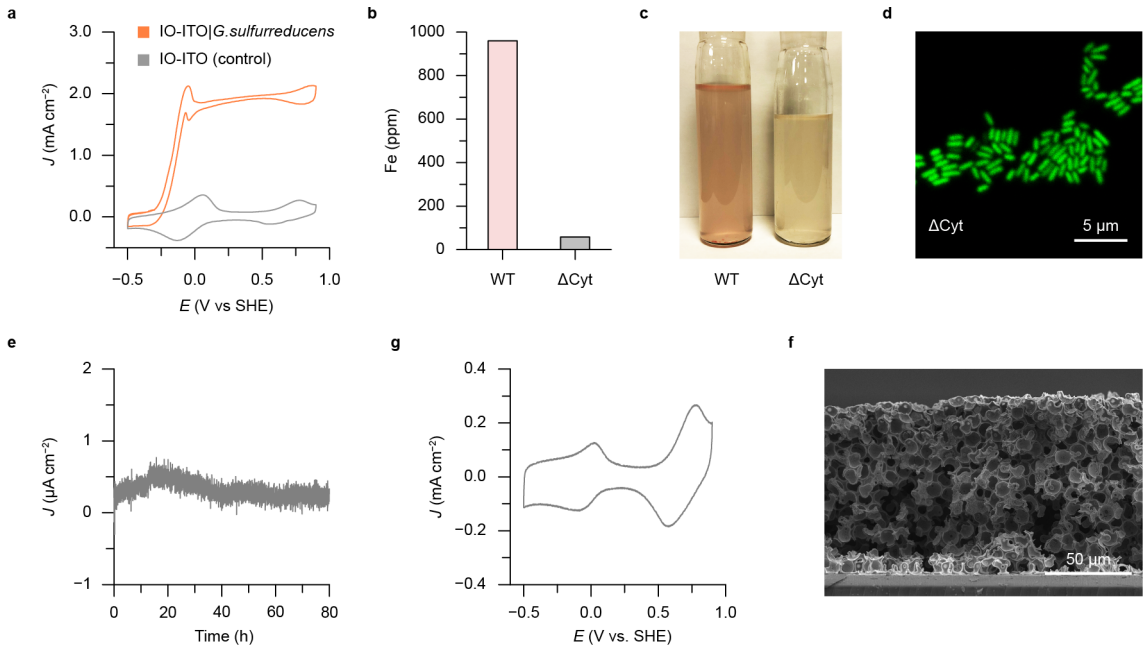

Figure 5.8 Extracellular electron transfer via outer membrane cytochromes. **a.** Representative CV scans of an IO-ITO|*G. sulfurreducens* electrode and a bare IO-ITO electrode (control) with acetate. The redox wave near 0 V vs. SHE is derived from the medium solution. Scan rate: 5 mV s^{-1}. **b.** The Fe quantity of the wild-type (WT) and cyt-suppressed (ΔCyt) *G. sulfurreducens*, determined by ICP-OES. **c.** Photographs of the WT and ΔCyt *G. sulfurreducens*. The reddish colour disappeared for ΔCyt *G. sulfurreducens* due to lack of iron-rich cytochromes. **d.** CLSM image of the ΔCyt *G. sulfurreducens* that was stained with the LIVE/DEAD BacLight bacterial viability kit (L7007) to distinguish the live (green) and dead (red) cells. The CLSM image shows a majority of ΔCyt *G. sulfurreducens* were live. Excitation: 476 nm; Emission: 480–520 nm (SYTO 9) and 610–660 nm (propidium iodide). **e,f.** Chronoamperometry and CV scan of the IO-ITO electrode with ΔCyt *G. sulfurreducens*. **f.** SEM image of the IO-ITO electrode with ΔCyt *G. sulfurreducens*. Bacteria without cyt *c* were unable to respire with the IO-ITO scaffold, thereby not forming biofilm within the electrode. Conditions: E = 0.4 V vs. SHE, 40 mM acetate, pH 7.4; CV: scan rate: 5 mV s^{-1}; 30 °C, purged with N_2:CO_2 (80:20, v:v%).

iron-deficient conditions. Elements analysis by inductively coupled plasma-optical emission spectroscopy (ICP-OES) shows a significant reduction of iron content in the resulting bacteria strain, which is also reflected by the disappearance of the indicative reddish colour (**Figure 5.8b,c**). Bacterial viability assessment suggests that the lack of cytochrome did not induce damages to cellular integrity and changes in bacterium morphology (**Figure 5.8d**). The ΔCyt *G. sulfurreducens* produced negligible current (0.5 μA cm^{-2}) and a non-turnover CV wave (**Figure 5.8e,g**), which confirms the necessity of cyt *c* for microbial electrogenesis. Electrons delivered from the bacterium were transferred through the conducting IO-ITO

scaffold. A control experiment with an insulating IO-ZrO_2 scaffold on ITO-coated glass produced negligible current and no bacterial colony was formed (**Figure 5.9**), which demonstrates that the conductivity of the electrode scaffold is essential for the bacterium's outward electron transfer and biofilm formation.

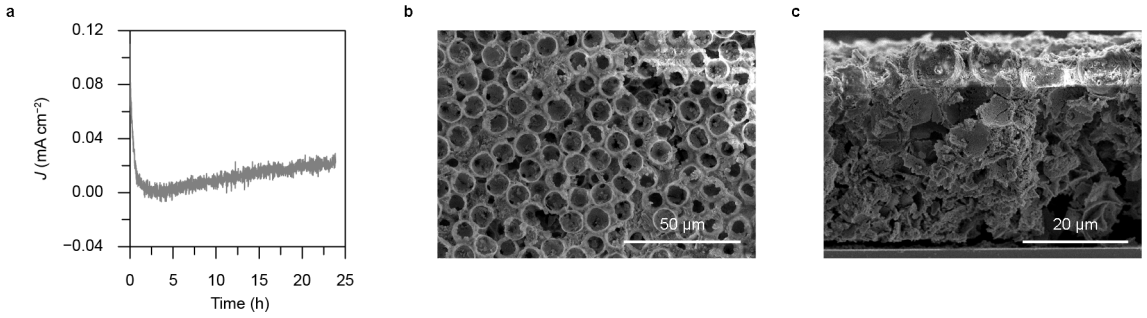

Figure 5.9 Control experiment with IO-ZrO_2 electrode (Geometrical area: 0.25 cm^2; pore size: 10 µm; thickness: 50 µm). **a.** Chronoamperometry of the IO-ZrO_2 electrode with *G. sulfurreducens*. **b,c.** SEM images of the IO-ZrO_2 electrode from the top (**b**) and side (**c**) view of the IO-ZrO_2 electrode after anodic culturing. There were no bacteria colonising within the non-conductive scaffold. Conditions: E = 0.4 V vs. SHE, 40 mM acetate, pH 7.4; 30 °C, purged with N_2:CO_2 (80:20, v:v%). The non-conductive IO-ZrO_2 scaffold was prepared on an ITO glass substrate following a similar co-assembly method using 10 µm PS beads and ZrO_2 nanoparticles (20–30 nm).

5.4 Potential dependence

The plateau anodic current was found variable with the applied electrochemical potential (**Figure 5.11a, 5.10**). The highest current density was attained at 0.1 V vs. SHE (2.9 ± 0.1 mA cm^{-2}, N = 10), whereas it reduced to 1.1 ± 0.1 mA cm^{-2} (N = 10) at 0.4 V vs. SHE (**Figure 5.11a**). Colourimetric protein quantification revealed that the biohybrid electrode at 0.1 V vs. SHE contained more proteins than at 0.4 V vs. SHE (**Figure 5.11b**). We thus infer that bacteria can overcome the thermodynamic challenge arising from a lower electrochemical potential to discharge electrons outward by adopting a different set of pathways.[293] This would allow them to maintain competitive advantages in habitats where redox states of electron acceptors are frequently varying due to environmental and meteorological perturbations. It is common practise in the field to apply high potentials (e.g. 0.4 V vs. SHE) to establish an electron sink for microbial respiration, but these results suggest that such positive potentials might not be optimal for microbial electrogenesis.

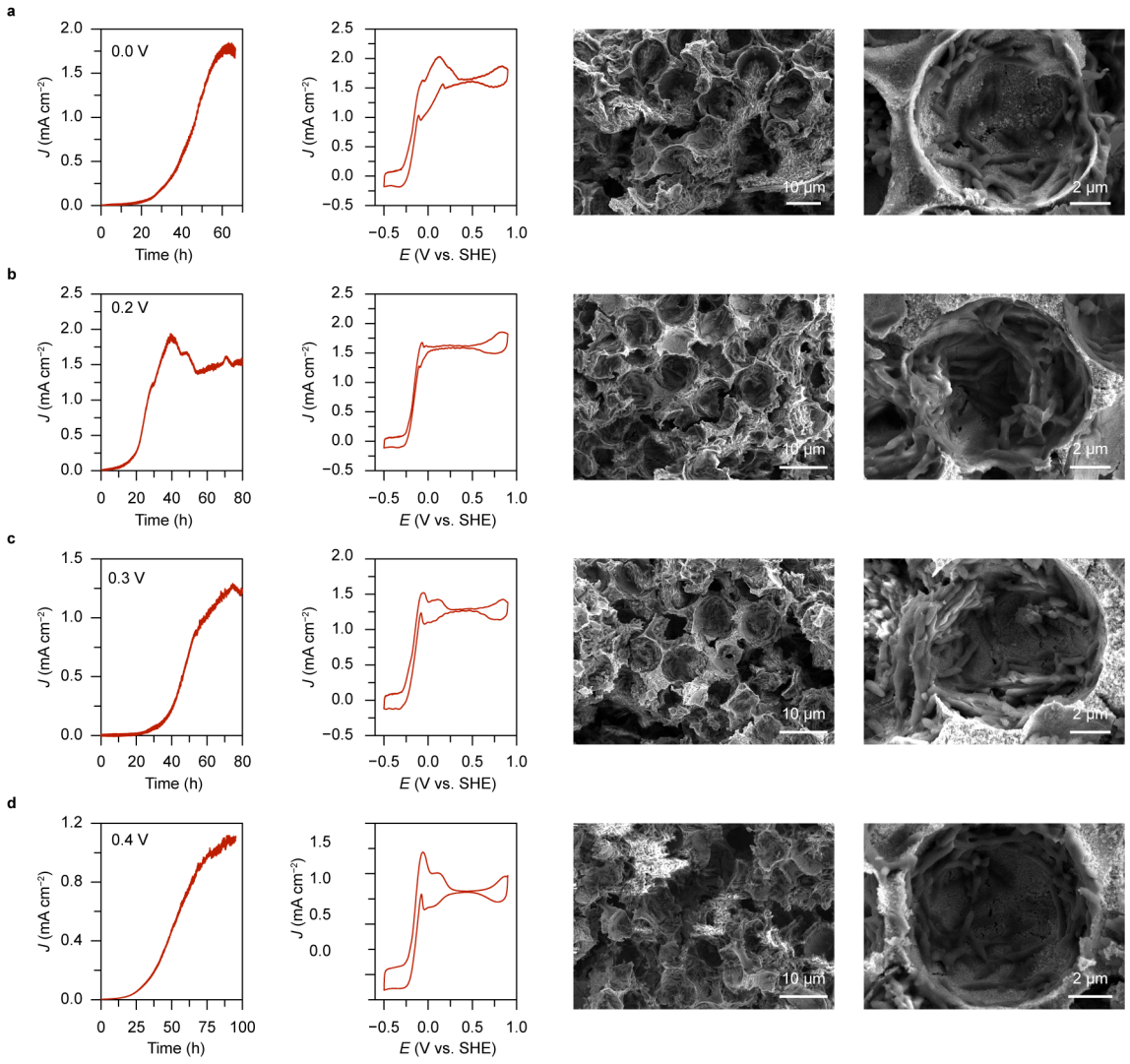

Figure 5.10 Potential dependent electrogenesis. Current density, CV scans and SEM images of IO-ITO|*G. sulfurreducens* electrodes at different potentials with acetate (40 mM, pH 7.4). **a.** 0.0 V vs. SHE; **b.** 0.2 V vs. SHE; **c.** 0.3 V vs. SHE; **d.** 0.4 V vs. SHE. Scan rate: 5 mV s^{-1}. All the electrochemical experiments were performed prepared 30 °C in N_2:CO_2 (80:20, v:v%).

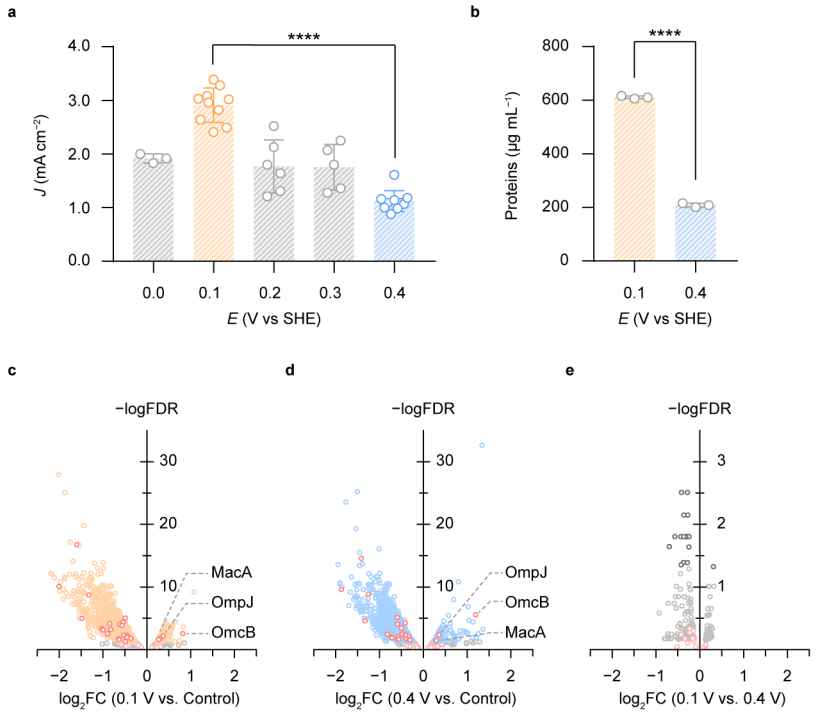

Figure 5.11 Potential dependent electrogenesis and differential gene expression analysis. **a.** Potential dependence of the current produced by IO-ITO|*G. sulfurreducens* electrodes. Independent samples: 0.0 V: $N = 3$; 0.1 V: $N = 10$; 0.2 V: $N = 6$; 0.3 V: $N = 6$; 0.4 V: $N = 10$. **b.** Colourimetric quantification of proteins in IO-ITO|*G. sulfurreducens* electrodes prepared at 0.1 V and 0.4 V vs. SHE. $N = 3$ independent samples. Error bars represent the standard error of the mean. Significance value: $^{****}p < 0.0001$. **c–e.** Volcano plots of differential gene expression of *G. sulfurreducens* in IO-ITO electrodes at 0.1 V and 0.4 V vs. SHE. **c**, 0.1 V vs. control; **d**, 0.4 V vs. control; **e**, 0.1 V vs. 0.4 V. The control group was the planktonic *G. sulfurreducens* anaerobically cultured in a medium solution with 20 mM acetate and 50 mM fumarate (pH 7.2) at 30 °C. The expression difference is represented by the log fold change in base 2 ($\log_2$FC) versus a baseline group (**c,d**, control; **e**, 0.4 V). The expression difference is considered significant provided that the false discovery rate (FDR), the adjusted p-value for multiple testing, is less than 0.05 ($-$logFDR > 1.3). Positive $\log_2$FC values represent higher expression compared with the baseline group. The red points indicate the genes encoding putative cyt *c* in *G. sulfurreducens* identified by Ref. [148]. Up-regulated genes encoding electron-carrying proteins (OmcB, OmpJ, MacA) are indicated in **c,d**. Each point represents the average value of one transcript in three replicates.

To understand whether the immobilisation and potential difference can induce transcriptional responses, RNA sequencing was employed to compare the gene expression of *G. sulfurreducens* grown on electrodes with different potentials and cultured in a medium solution with a soluble electron acceptor (fumarate). RNA sequencing can produce a genome-scale transcription map that enables a global view of transcriptome and reflects expression

levels for individual genes.[294] The RNA sequencing and data analysis were performed in Cambridge Genomic Services (Section 2.3.5). The workflow is briefly illustrated here: RNA was extracted from *G. sulfurreducens* cultured within the IO-ITO electrodes and reversely transcribed to cDNA. The cDNA was then fragmented and sequenced in a high-throughput manner to obtain short sequences termed "short sequenced reads", which were then aligned to a reference genome to produce a genome-scale transcription map. Transcript expression was calculated based on the number of reads aligned to each gene.

Table 5.1 Significance summary of differential gene expression analysis

Comparison	Total genes	FDR <0.05 genes		
		Total	Up-regulated	Down-regulated
0.1 V vs. 0.4 V	3586	19	1	18
0.1 V vs. Ctrl	3612	978	250	728
0.4 V vs Ctrl	3602	907	234	673

Table 5.2 Three genes encoding proteins involved in extracellular electron transfer

Genes	Proteins	0.1 vs. Ctrl		0.4 V vs. Ctrl		0.1 V vs. 0.4 V	
		Log_2FC	FDR	Log_2FC	FDR	Log_2FC	FDR
GSU2737	OmcB	0.83	0.003	1.19	<0.0001	-	n.s.
GSU0466	MacA	0.38	0.006	0.29	0.034	-	n.s.
GSU3304	OmpJ	0.43	0.020	0.43	0.018	-	n.s.

Differential gene expression analysis shows a substantial down-regulation of gene expression when bacteria are grown on electrodes, compared with those cultured in a medium solution with fumarate as the electron acceptor (**Figure 5.11c,d**). Amongst more than 3500 genes sequenced, ∼25% of genes were induced with significant changes (FDR < 0.05) in expression on electrodes, with ∼75% of them down-regulated (**Table 5.1**). This suggests that *G. sulfurreducens* deployed a different metabolic strategy that consumes less energy when interfaced with an electrode.[295] Microorganisms survive and thrive under different environments thanks to their acute and flexible regulatory mechanisms, which enable them to maintain their homeostasis in response to environmental variations. Through various sensing and transduction pathways, extracellular changes can be translated into intracellular signals that induce transcriptional responses. *G. sulfurreducens* can use various forms of soluble and insoluble electron acceptors.[132] Soluble electron acceptors such as fumarate can diffuse into a cell and participate in intracellular metabolism, whereas insoluble electron acceptors such as metal oxides cannot permeate through the cellular membrane and can only be utilised for anaerobic respiration by extracellular electron transfer. In a biohybrid system, an electrode with a poised electrochemical potential substitutes for natural minerals as an inexhaustible

electron sink, which forms the basis of microbial electrogenesis. When *G. sulfurreducens* is transferred to a new environment deprived of soluble electron acceptors (fumarate), bacteria will regulate gene expression to align their metabolism with the physiological needs of using an electrode as the electron acceptor. Although their cellular regulation has not been completely deciphered due to many genes with unknown functionality,[296] several genes that are found responsible for extracellular electron transport could shed light on part of their adaptation strategies. Genome-wide study has identified 111 gene encoding putative cyt *c* (109 of them found in this study) in *G. sulfurreducens*,[148] but only 16 multihaem cyt *c* were found essential for extracellular electron transfer.[297]

The transcriptional regulation is likely to occur during the initial lag phase, when electron transfer pathways are shifted to favour insoluble electron acceptors (electrodes). This is supported by the up-regulation of genes (GSU2737, GSU0466, GSU3304) encoding proteins that are involved in extracellular electron transfer (OmcB, OmpJ and MacA) (**Figure 5.4d, Table 5.2**), thereby enhancing the bacterial interaction with extracellular electron acceptors.[298–301] OmcB is an outer membrane cyt *c* essential for the Fe(III) reduction via extracellular electron transfer in nature.[299,302] OmpJ is an outer membrane protein (porin) that upholds the structural integrity of the periplasmic space for the proper functioning of electron transport components.[298] MacA is a periplasmic protein that mediates the electron transfer between the inner and the outer membrane.[300] Nevertheless, there was no significant change in gene expression at different potentials (0.1 V and 0.4 V vs. SHE) (**Figure 5.4e**), despite large differences in current density (**Figure 5.4a**), suggesting potential variations cannot stimulate extensive transcriptional responses. These findings imply that *G. sulfurreducens* adjusted its gene expression to keep intracellular metabolism in tune with physiological needs with different electron acceptors, whereas electrode potentials cannot induce tangible responses at a transcriptional level. The question on how *G. sulfurreducens* can sense electrode potentials and respond to potential variations remains unclear and requires further investigations.

5.5 Syntrophic electrogenesis

In nature, different bacteria form symbiotic partners via interspecies mass transport or electron transfer to overcome environmental disadvantages.[303] This inspires a syntrophic strategy for electrogenesis, which employs the syntrophy between mixed cultures of electroactive bacteria, and thus grants the system additional resilience to environmental perturbations such as limited electron donors. *S. loihica* is an electrogenic bacterium ubiquitously thriving in aquatic and sedimentary environments. It has evolved robust sensing and regulatory

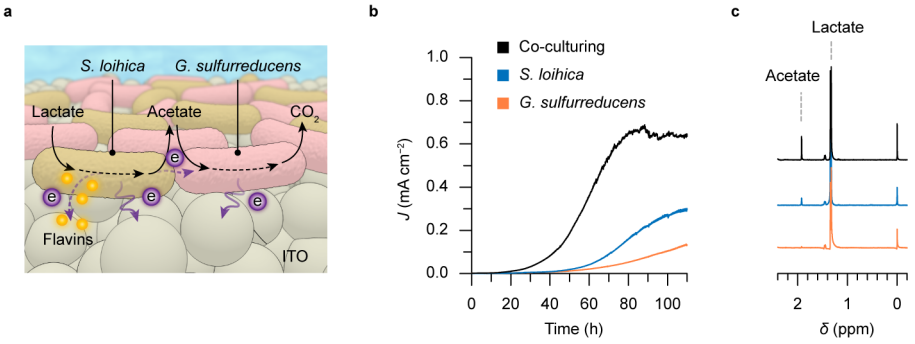

Figure 5.12 Syntrophic electrogenesis. **a.** Schematic illustration of syntrophic electrogenesis in an IO-ITO electrode. *S. loihica* metabolises lactate into acetate and transfers electrons to the electrode mainly through self-excreted flavins. *G. sulfurreducens* then consumes acetate and releases electrons to the electrode. **b.** Representative currents of *G. sulfurreducens*, *S. loihica*, and a mixed culture of *G. sulfurreducens* and *S. loihica*, with an IO-ITO electrode at 0.4 V vs. SHE with lactate (40 mM, pH 7.4). The insets are ^{1}HNMR spectra of the electrolyte solution extracted after 100 h electrogenesis with IO-ITO|*G. sulfurreducens*, IO-ITO|*S. loihica*, and IO-ITO|coculture. TMSP-d^{4} (1 mM) was used as the reference (0 ppm) and internal standard for quantification. ^{1}HNMR peaks of acetate (singlet, 1.92 ppm) and lactate (doublet, 1.34 ppm) are indicated. All the electrochemical experiments were performed under a N_2:CO_2 atmosphere (80:20, v:v%) at 30 °C.

systems that confer its metabolic versatility.[304] *S. loihica* and *G. sulfurreducens* have similar morphology and dimensions (**Figure 5.13a,b**), but differ in metabolic pathways: *S. loihica* utilises lactate as the carbon and energy resource instead of acetate and it engages with extracellular electron acceptors mainly through self-secreted flavins. By co-culturing *S. loihica* and *G. sulfurreducens* in an IO-ITO electrode, lactate can be used as the sole electron donor to support the electrogenesis of both strains. In this case, *S. loihica* metabolises lactate into acetate that can be further utilised by *G. sulfurreducens*, while both bacteria release electrons to the electrode (**Figure 5.12a**). Such syntrophic pathway can increase the stoichiometric production of electrons and further attest that the IO-ITO electrode is a robust and versatile host for various microbial communities.

As *G. sulfurreducens* poorly utilises lactate for metabolism,[137] the current output at 0.4 V vs. SHE (0.13 mA cm^{-2}) with lactate was far below that with acetate as the electron donor (1.07 mA cm^{-2}) (**Figure 5.12b**). This is also evidenced by a reduced *G. sulfurreducens* population on the electrode (**Figure 5.13c**). The current density produced by *S. loihica* (0.30 mA cm^{-2}) with lactate was smaller than that of *G. sulfurreducens* with acetate at 0.4 V vs. SHE, despite a large population of *S. loihica* on the electrode (**Figure 5.13d**). This results from a diffusion-governed extracellular electron transfer by *S. loihica*, which is kinetically less efficient compared with direct electron transfer via outer membrane cytochromes in

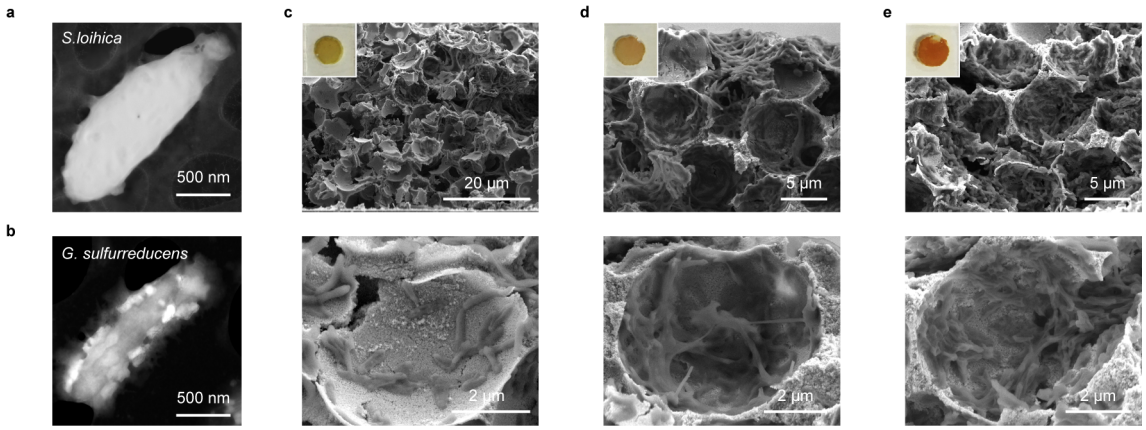

Figure 5.13 Coculturing *S. loihica* and *G. sulfurreducens* in IO-ITO electrodes. **a,b.** Scanning transmission electron microscope images of *S. loihica* (**a**) and *G. sulfurreducens* (**b**). **c–e.** Cross-sectional SEM images of IO-ITO|*G. sulfurreducens* (**a**), IO-ITO|*S. loihica* (**b**), and IO-ITO|coculture (**c**). The insets show the photographs of the hybrid electrodes. The SEM images along with photographs representatively reflect the bacterial colony in different electrodes, but they are unable to distinguish *G. sulfurreducens* and *S. loihica* due to similar morphologies. All these hybrid electrodes were prepared at 0.4 V vs. SHE with lactate (40 mM, pH 7.4) at 30 °C in N_2:CO_2 (80:20, v:v%).

G. sulfurreducens. Inoculation of both *S. loihica* and *G. sulfurreducens* attained a higher current of 0.68 mA cm^{-2}, and yielded more acetate (∼2.9 mM) than *S. loihica* alone (∼1.6 mM) (**Figure 5.12c**). These together point to a syntrophy between *G. sulfurreducens* and *S. loihica*: the presence of *G. sulfurreducens* perhaps assisted *S. loihica* in discharging more electrons via interspecies electron transfer, which produced more acetate and facilitated the growth of both strains (**Figure 5.13e**).

5.6 Summary

This chapter presents a semi-biological system employing electroactive bacteria integrated inside a porous and hydrophilic IO-ITO electrode architecture. The resulting biohybrid electrodes provided a platform to wire bacteria's intrinsic physiological functionality with artificial electronics, and allowed a high degree of control over system configuration and operation. The biohybrid electrode attained a current density of 3 mA cm^{-2} at 0.1 V vs. SHE and indicates a high population of *G. sulfurreducens* actively metabolising within the electrode scaffold. Differential gene expression analysis revealed that *G. sulfurreducens* up-regulated genes encoding electron-carrying proteins to facilitate the electron transfer toward electrodes. *G. sulfurreducens* was further cocultured with *S. loihica* in the IO-ITO electrode

to create a syntrophic pathway for electrogenesis. The bacterium-colonised electrode can be used as a "living" electrode to perform chemical reactions at cathodic conditions. Such applications will be discussed in the next chapter.

Chapter 6

Inverse opal-indium tin oxide electrode for microbial photoelectrosynthesis

The contents of this chapter were obtained solely by the author of this thesis, with contributions from others as outlined here: Dr. Shafeer Kalathil cultured G. sulfurreducens and M. barkeri; Dr. Qian Wang prepared $BiVO_4$-CoO_x electrodes.

6.1 Introduction

The anodic growth primes a microbial electrode populated with a large colony of electroactive *G. sulfurreducens*. This chapter demonstrates how such hybrid electrodes can be utilised to drive chemical reactions. This was carried out by poising negative potentials on the resulting IO-ITO|*G. sulfurreducens* electrode. Under such conditions, *G. sulfurreducens* accepts electrons from the electrode to sustain its metabolism and disposes respiratory electrons by reducing soluble fumarate or heterogeneous GO. To outsource the electron supply to a renewable source, the biohybrid electrode was coupled with a photoanode to achieve photoelectrosynthesis without applying an external electrochemical voltage. *G. sulfurreducens* could be further cultured with methanogens *M. barkeri* inside the IO-ITO scaffold to form a syntrophic partnership that could conduct CO_2 reduction to CH_4 through the direct interspecies electron transfer.

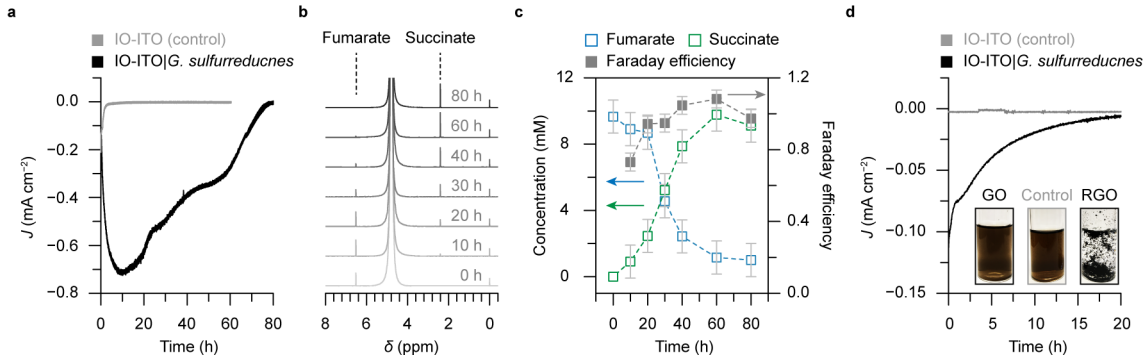

Figure 6.1 Microbial electrosynthesis with the IO-ITO|*G. sulfurreducens* electrode. **a.** Representative cathodic current of an IO-ITO|*G. sulfurreducens* V vs. SHE. A bare IO-ITO electrode was used as a control. **b.** ^{1}HNMR spectra of the electrolyte aliquoted during the course of reaction. TMSP-d^{4} (1 mM) was used as the reference (0 ppm) and internal standard for quantification. ^{1}HNMR peaks of fumarate (singlet, 6.52 ppm) and succinate (singlet, 2.41 ppm) are indicated. **c.** Quantification of reactants and products and Faraday efficiency during the course of reaction. **d.** Cathodic current of an IO-ITO|*G. sulfurreducens* electrode reducing GO (0.1 mg mL^{-1}) at −0.3 V vs. SHE. A bare IO-ITO electrode was used as a control. The insets show photographs of GO solutions before and after reduction by a bare IO-ITO and an IO-ITO|*G. sulfurreducens* electrode. All the reactions were performed in a N_2:CO_2 atmosphere (80:20 v:v%) at 30 °C, with Pt and Ag/AgCl as counter and reference electrode, respectively.

6.2 Microbial electrosynthesis

Electrosynthesis was performed with an IO-ITO|*G. sulfurreducens* electrode prepared at 0.1 V vs. SHE for 80–100 h, until the current stabilised. A prototypical reaction, fumarate reduction, was used to exemplify the potential of harnessing intracellular metabolism for chemical synthesis. Fumarate reduction to succinate is part of a biosynthetic pathway that transforms CO_2 into carboxylic acid and is an essential reaction for bacterium survival under anaerobic conditions.[305] At −0.45 V vs. SHE, the IO-ITO|*G. sulfurreducens* electrode generated a cathodic current that returned to zero after 80 h (**Figure 6.1a**). During the process, fumarate was stoichiometrically reduced to succinate with Faraday efficiency of 93 ± 12% (**Figure 6.1b,c**), whereas fumarate cannot be electrochemically reduced by a bare IO-ITO electrode at the same potential (**Figure 6.1a**).[182]

Furthermore, this hybrid electrode can carry out reactions beyond the bacterium's native metabolic pattern. Planktonic *Geobacter* can reduce GO by extracellularly transferring electrons to GO with the presence of electron donors.[306] The sessile *G. sulfurreducens* in an IO-ITO scaffold could reduce GO in a similar fashion at −0.3 V vs. SHE. The reduction of GO after 20 h is indicated by the increasing hydrophobicity of RGO and

rise of intensity ratio of D and G band in the Raman spectra (**Figure 6.1d, 6.2**).[307] In absence of bacteria, a minimum cathodic current was recorded (**Figure 6.1d**), suggesting GO was reduced by *G. sulfurreducens* and not by the IO-ITO scaffold at −0.3 V vs. SHE (conventional electrochemical GO reduction is implemented at a more negative potential; −0.7 V vs. SHE at pH 7.2).[308] It shows that *G. sulfurreducens* could accept electrons from the cathode and intracellularly reduce fumarate to succinate and extracellularly reduce GO to RGO, and further demonstrates the synthetic versatility of the biohybrid electrode to prepare functional materials beyond natural metabolites with reduced energy input under physiological conditions to rival more energy-intense synthetic routes.

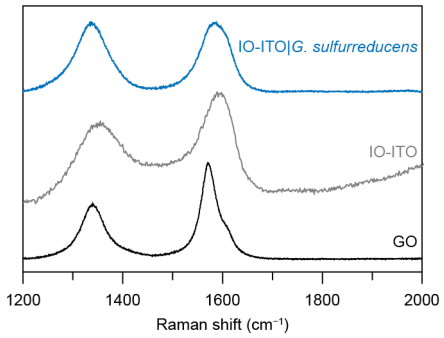

Figure 6.2 Raman spectra of the GO before and after reduced by an IO-ITO electrode and a IO-ITO|*G. sulfurreducens* hybrid electrode at −0.3 V vs. SHE. The intensity ratio of D (∼1350 cm^{-1}) and G band (∼1580 cm^{-1}): 0.57 (GO), 0.87 (IO-ITO), 1.00 (IO-ITO|*G. sulfurreducens*).

6.3 Microbial photoelectrosynthesis

In this section, I seek to couple the IO-ITO|*G. sulfurreducens* electrode to a photoanode so as to outsource the electron supply to photochemistry. I first employed an IO-TiO_2 photoanode (geometrical surface area: 0.25 cm^2) sensitised with a photosensitive phosphonated [Ru(II)(2,2′-bipyridine)$_3$]-based dye (**RuP**, λ_{max} = 457 nm) to enable visible-light absorption (**Figure 6.3a,b**).[68,311] Under irradiation, the excited **RuP*** dye injects an electron into the conduction band of TiO_2 electrode, which travels to the cathode via an external circuit, while the photogenerated hole is quenched by taking an electron from TEOA.

The onset potential of the IO-TiO_2|**RuP** photoanode in the presence of TEOA (pH 7.2) was determined at −0.6 V vs. SHE (**Figure 6.3c**), which corresponds to the quasi-Fermi level of TiO_2. The catalytic wave of fumarate reduction by the biohybrid electrode appeared at −0.2 V vs. SHE (**Figure 6.3d**). Given $E_{Fumarate/Succinate}$ = 0.03 V vs. SHE (pH 7.0), the

negative shift of onset potential presumably relates to the redox potentials of outer membrane cytochromes (−0.4–0.1 V vs. SHE),[176] which presumably take part in the electron uptake from the electrode. The energy levels were thus well-aligned to permit autonomous light-driven fumarate reduction without an electrochemical bias in two-electrode configuration (**Figure 6.3e**). After 24 h of simulated solar irradiation (I = 100 mW cm^{-2}, AM 1.5G), 0.79 ± 0.10 mM succinate was detected, along with intermediate metabolites such as malate (doublet of doublets, 2.7 ppm), pyruvate (singlet, 2.38 ppm),[285] corresponding to a succinate yield of (7.8 ± 1.1)% (**Figure 6.3f,g**). The presence of additional metabolites indicates that the bacteria retained their metabolic activity with electrons supplied by the photoanode and thus reduced fumarate via intracellular biochemical pathways. No such products were detected in absence of bacteria at the same condition. Note that the photocurrent decayed during the course of PEC reaction, which was likely due to the photodegradation of the **RuP** dye.[68]

The IO-TiO_2|**RuP** photoanode employs a sacrificial reagent (TEOA) as the electron donor and is prone to photodegradation. To overcome these drawbacks, I resorted to monoclinic $BiVO_4$ as the light-absorbing material in view of its well-suited band structure for water oxidation to O_2 (band gap: 2.4 eV; conduction band potential: −0.4 V vs. SHE, pH 7.0).[312] I employed $BiVO_4$ deposited with a CoO_x cocatalyst as the photoanode to directly extract electrons from water (in a phosphate buffer solution, pH 7.3) (**Figure 6.4a,b**).[227] The $BiVO_4$-CoO_x electrode displayed a photocurrent onset potential at −0.35 V vs. SHE (**Figure 6.4c,d**), which is close to the conduction band of $BiVO_4$. Compared with IO-

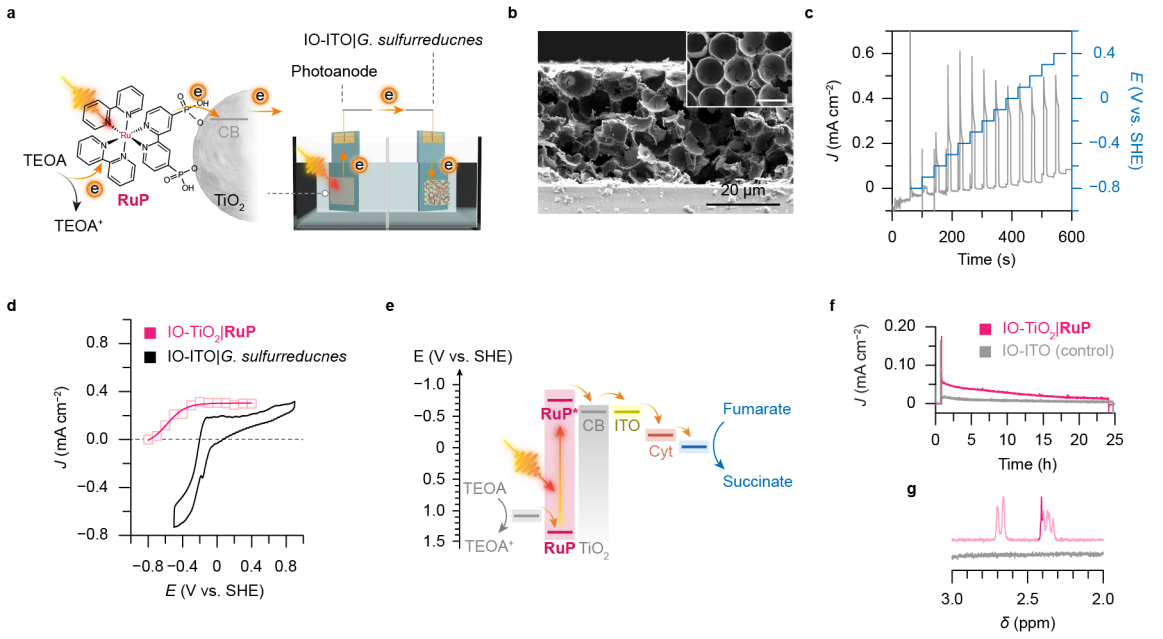

Figure 6.3 Microbial photoelectrosynthesis in a tandem system with an IO-ITO|*G. sulfurreducens* electrode connected to a dye-sensitised TiO_2 photoanode. **a.** Schematic representation of a PEC cell consisting of an IO-TiO_2|**RuP** photoanode and an IO-ITO|*G. sulfurreducens* cathode. Under irradiation, the excited **RuP*** dye injects an electron into the conduction band of TiO_2 electrode, which is further directed to the cathode via an external circuit. The $\mathbf{RuP}^+$ dye is regenerated by extracting an electron from TEOA. **b.** SEM image of an IO-TiO_2 electrode. The inset shows the top view of the electrode (scale bar: 10 μm). The IO-TiO_2 electrode has a thickness of 40 μm and macropore size of 10 μm. **c.** Stepped chronoamperometry of the IO-TiO_2|**RuP** photoanode in TEOA (25 mM, pH 7.2), with Pt and Ag/AgCl as the counter and reference electrode, respectively. The electrode was under periodic irradiation (10 s in light, 30 s in dark, I = 100 mW cm^{-2}, AM 1.5G) at stepped potentials from −0.7 V to 0.4 V vs. SHE. The experiment was performed in N_2:CO_2 (80:20, v:v%). **d.** Photocurrent from chronoamperometry of the IO-TiO_2|**RuP** (0.25 cm^2) photoanode and a CV scan of the IO-ITO|*G. sulfurreducens* electrode in fumarate (10 mM, pH 7.2) solution. Three-electrode configuration, scan rate: 5 mV s^{-1}. **e.** Energy level diagram of an IO-TiO_2|**RuP** photoanode coupled with an IO-ITO|*G. sulfurreducens* cathode with respect to an electrochemical potential scale at pH 7.0. Energy levels of TiO_2 and **RuP** are taken from Ref. [309]. As the mechanism of electron intake by bacterium remains elusive, here I tentatively assume electrons are transferred inward via cyt *c* with redox potentials centred at −0.2 V vs. SHE.[176,310] The reduction potential of fumarate (0.03 V vs. SHE) is sourced from Ref. [182]. **f.** Photocurrent of light-driven fumarate reduction with an IO-TiO_2|**RuP**||IO-ITO|*G. sulfurreducens* two-electrode tandem system at zero bias. A bare IO-ITO electrode without bacteria was used as the cathode for a control experiment (grey trace). TEOA (25 mM, in 50 mM KCl) was used as the electron donor for the photoanode. The photocurrent was normalised to the geometrical area of the cathode (0.25 cm^2). **g.** ^{1}HNMR spectra of the solution extracted from the cathode compartment after 24 h of irradiation. TMSP-d^4 (1 mM) was used as the reference (0 ppm) and internal standard for quantification. The NMR peak of succinate (singlet, 2.41 ppm) is highlighted and the doublet of doublets peaks at 2.7 ppm are assigned to malate. Conditions: 20 mM fumarate, pH 7.2, E = 0 V, I = 100 mW cm^{-2}, AM 1.5G, in a N_2:CO_2 (80:20 v:v%) atmosphere at 25 °C.

TiO_2|**RuP** photoanode, the $BiVO_4$-CoO_x electrode enabled smaller energy margin to drive photoelectrons toward the intracellular pathways (**Figure 6.4e**). As such, the resulting $BiVO_4$-CoO_x||IO-ITO|*G. sulfurreducens* tandem PEC system generated a smaller photocurrent at zero bias and yielded 0.51 ± 0.20 mM succinate after 24 h of irradiation (I = 100 mW cm^{-2}, AM 1.5G) (**Figure 6.4f,g**). In contrast, inactivation of the bacteria by biocide on the cathode resulted in no succinate and other metabolites, confirming fumarate reduction was performed through bacterial metabolism (**Figure 6.4g**).

Light-driven fumarate reduction has been previously realised using isolated flavoenzymes as the biocatalyst,[313,314] but the system performance was highly limited by the fragility of

isolated enzymes and susceptible to enzyme orientations that dictate the electron transfer at biointerfaces. The microbial system here enabled higher catalytic capacity and improved stability, thanks to the large number of robust bacteria integrated inside the IO-ITO scaffold. Moreover, the proteinaceous electron conduits on bacterial membranes allow for omnidirectional electron transfer toward electrodes, regardless of the bacteria orientation. The photosynthetic biohybrid systems here decoupled light harvesting on the photoanode from chemical transformation at the cathode, rendering the system optimisation highly flexible. The photoanode can be facilely varied in morphology to enhance photocurrent, be substituted with better-performing light absorbing materials to improve photostability, and be supplemented with water-oxidising electrocatalysts to eliminate the reliance on sacrificial electron donors. The design and implementation of microbial photoelectrosynthesis can further take lessons from mechanistic understandings and optimisation guidelines that are well-established in the field of artificial photosynthesis.

6.4 Syntrophic electrosynthesis

The IO-ITO|*G. sulfurreducens* electrode has demonstrated the ability to catalyse both biotic (fumarate reduction) and abiotic (GO reduction) reactions. However, the scope of reactions is limited by *G. sulfurreducens* that cannot reduce CO_2 due to the lack of carbon assimilation pathways. Synthetic biology offers genetic toolsets that can integrate alien CO_2-fixation

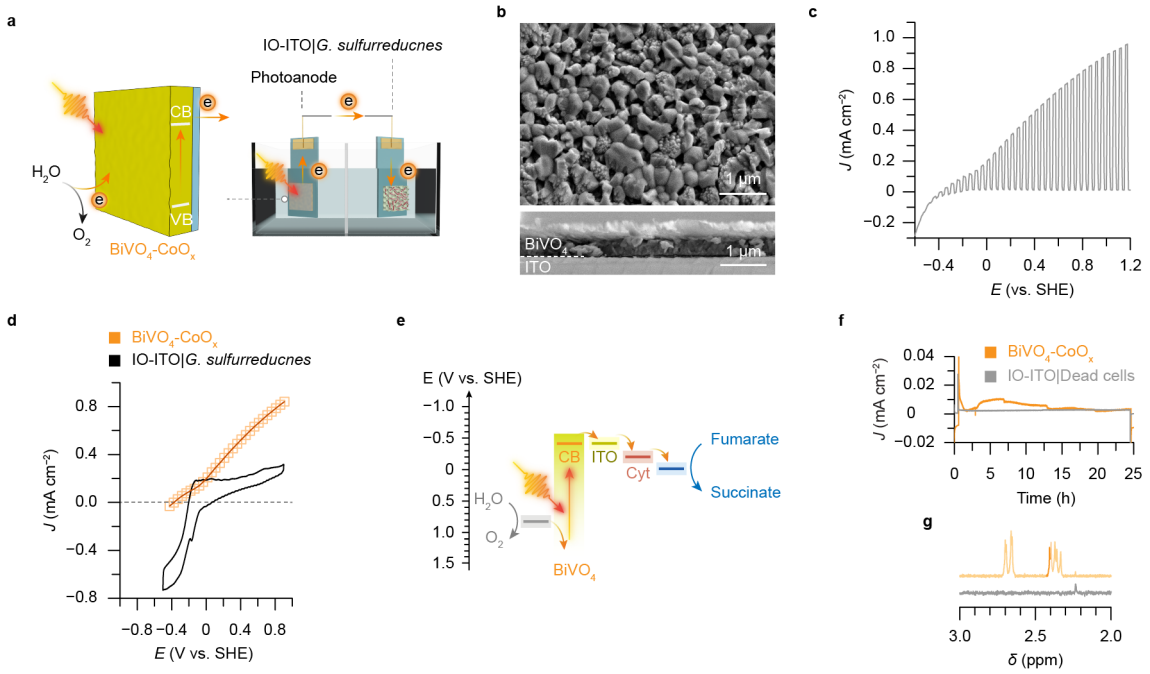

Figure 6.4 Microbial photoelectrosynthesis in a tandem system with an IO-ITO|*G. sulfurreducens* electrode connected to a $BiVO_4$-CoO_x photoanode. **a.** Schematic representation of a PEC cell consisting of a $BiVO_4$-CoO_x photoanode and an IO-ITO|*G. sulfurreducens* cathode. Under irradiation, $BiVO_4$ absorbs light and donates excited electrons to the external circuit whilst oxidising water with the aid of the CoO_x cocatalyst. **b.** Top-view and cross-sectional SEM images of an $BiVO_4$-CoO_x electrode. The thickness of $BiVO_4$ film was 500 nm and CoO_x cocatalysts were deposited on top. **c.** Linear sweep voltammetry trace of the $BiVO_4$-CoO_x electrode in phosphate buffered saline (20 mM Na_2HPO_4, pH 7.3) under periodic irradiation (5 s in light, 5 s in dark, I = 100 mW cm^{-2}, AM 1.5G). Scan rate: 5 mV s^{-1}. Pt and Ag/AgCl were employed as the counter and reference electrode, respectively. The experiment was performed in N_2:CO_2 (80:20, v:v%). **d.** Photocurrent from chronoamperometry of the $BiVO_4$-CoO_x (1.0 cm^2) photoanode and a CV scan of the IO-ITO|*G. sulfurreducens* electrode in fumarate (10 mM, pH 7.2) solution. Three-electrode configuration, scan rate: 5 mV s^{-1}. **e.** Energy level diagram of a $BiVO_4$-CoO_x photoanode coupled with an IO-ITO|*G. sulfurreducens* cathode with respect to an electrochemical potential scale at pH 7.0. The conduction band (CB) edge of $BiVO_4$ was taken from Ref. [312] **f.** Photocurrent of light-driven fumarate reduction with a $BiVO_4$-CoO_x||IO-ITO|*G. sulfurreducens* two-electrode tandem system at zero bias. A hybrid electrode with dead bacteria (inactivated by 0.1% glutaraldehyde) was used as the cathode for a control experiment (grey trace). A phosphate buffered saline solution (20 mM Na_2HPO_4, pH 7.3) was used for the photoanode compartment. The photocurrent was normalised to the geometrical area of the cathode (0.25 cm^2). **g.** ^{1}HNMR spectra of the solution extracted from the cathode compartment after 24 h of irradiation. TMSP-d^4 (1 mM) was used as the reference (0 ppm) and internal standard for quantification. The NMR peak of succinate (singlet, 2.41 ppm) is highlighted and the doublet of doublets peaks at 2.7 ppm are assigned to malate. Conditions: 20 mM fumarate, pH 7.2, E = 0 V, I = 100 mW cm^{-2}, AM 1.5G, in a N_2:CO_2 (80:20 v:v%) atmosphere at 25 °C.

pathways (e.g. Calvin cycle) into heterotrophic microorganisms such as *E. coli*.[315] Yet *G. sulfurreducens* has not been subjected to genetic engineering to this end, and the extensive regulation and complex interactions between metabolic pathways can render such alternation problematic.[47] On the other hand, methanogenic archaea can reduce CO_2 into CH_4 during the course of anaerobic respiration, but have limited electron uptake ability from electrode.[316] It has been shown that *G. metallireducens* can electrically interact with *M. barkeri*, a cyt-containing methanogen, through direct interspecies electron transfer, which allowed stoichiometric conversion of ethanol to CH_4 unattainable by individual strains alone.[317] Here I show such synergistic symbiosis can be leveraged to carry out CO_2 reduction to CH_4 with IO-ITO electrodes colonised with mixed cultures of *G. sulfurreducens* and *M. barkeri* (**Figure 6.5**). This process is reminiscent of the syntrophic electrogenesis where two strains of bacteria cooperate to generate electricity, and is hereby termed as “synthrophic

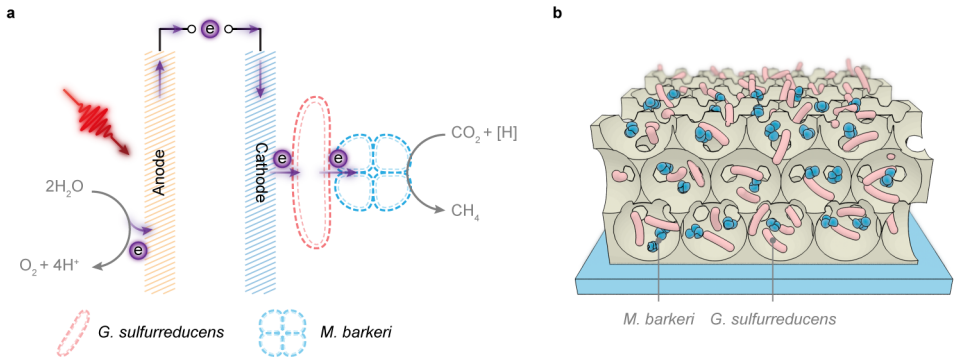

Figure 6.5 Coculturing *G. sulfurreducens* and *M. barkeri* in IO-ITO electrodes for syntrophic electrosynthesis. **a.** Schematic representation of light-driven syntrophic electrosynthesis. A photoanode is used to harvest solar light and extract electrons from water to feed the downstream chemical synthesis. A cathode is cocultured with *G. sulfurreducens* and *M. barkeri* and reduces CO_2 to CH_4 via interspecies electron transfer. **b.** Schematic illustration of an IO-ITO electrode scaffold populated by *G. sulfurreducens* (red) and *M. barkeri* (blue).

electrosynthesis". Bacterial cocultures, i.e., electrotrophs and methanogens or acetogens, have previously been employed to produce CH_4 or acetate from CO_2 with electrons supplied by a graphite electrode and mediated by biotically-generated H_2 between species (Section 1.7.4).[318] In the symbiotic system here, *G. sulfurreducens* can interact with *M. barkeri* in a different manner, namely, by direct interspecies electron transfer.

IO-ITO electrode with 20 μm macropores were designed to provide sufficient surface for the cocultures (Section 2.1.2). The syntrophic electrosynthesis was implemented following a workflow illustrated in **Figure 6.6a**. First, *G. sulfurreducens* was cultured in an IO-ITO scaffold at 0.4 V vs. SHE, with acetate as the electron donor (**Figure 6.6b**). Then the resulting IO-ITO|*G. sulfurreducens* electrode was placed in a new medium containing methanol as the electron donor to *M. barkeri* at 0.4 V vs. SHE. Possible electron acceptors (HCO_3^-, CO_3^{2-}, CO_2) were removed from the electrolyte. The current decay in the first 24 h was derived from the consumption of acetate remained in the *G. sulfurreducens* biofilm and further suggests that *G. sulfurreducens* could not metabolise methanol (**Figure 6.6c**). After inoculating *M. barkeri*, the anodic current increased as a result of the metabolic conversion of methanol. Negligible current was detected when *M. barkeri* was cocultured with an inactivated IO-ITO|*G. sulfurreducens* electrode (*G. sulfurreducens* in the electrode was inactivated by glutaraldehyde) (**Figure 6.6c**, the grey trace), suggesting *M. barkeri* discharged electrons to the electrode via *G. sulfurreducens*. The attained coculture electrode was transferred to a fresh medium in absence of both electron donors and soluble electron acceptors, so as to consume the remaining methanol (**Figure 6.6d**). Lastly, the IO-ITO|coculture electrode was poised with −0.4 V vs. SHE and furnished with CO_2 (in the form of HCO_3^-, CO_3^{2-}).

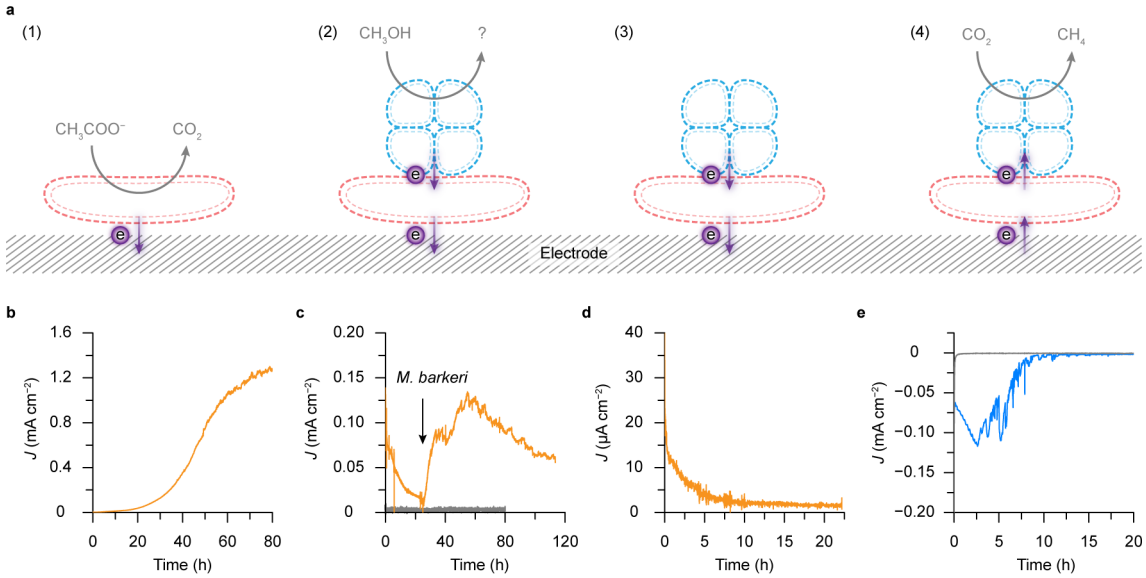

Figure 6.6 Workflow and chronoamperometry of syntrophic electrosynthesis with *G. sulfurreducens* and *M. barkeri*. **a.** Workflow of syntrophic electrosynthesis. (1) *G. sulfurreducens* is first cultured within an IO-ITO (20 μm) anode with acetate as the electron donor. (2) *M. barkeri* is cultured within the IO-ITO|*G. sulfurreducens* electrode with methanol as the sole electron donor to *M. barkeri* in absence of soluble electron acceptors (HCO_3^-, CO_3^{2-}, CO_2). (3) The resulting IO-ITO|mixed-culture is placed in a fresh medium without electron donors and soluble electron acceptors at anodic conditions to consume methanol remaining in biofilms. (4) A negative potential is applied on the IO-ITO|coculture electrode to perform CO_2-to-CH_4 conversion by means of interspecies electron transfer. **b.** Anodic growth of *G. sulfurreducens* in an IO-ITO (20 μm) electrode. Conditions: $E = 0.4$ vs. SHE, pH 7.4, 40 mM acetate, N_2:CO_2 (80:20, v:v%), 30 °C. **c.** Coculturing *M. barkeri* within the IO-ITO|*G. sulfurreducens* electrode. The arrow indicates the addition of *M. barkeri* into the medium solution. Grey trace: coculturing *M. barkeri* with an inactivated IO-ITO|*G. sulfurreducens* electrode. Conditions: $E = 0.4$ vs. SHE, pH 7.4, 123 mM methanol, without HCO_3^-, N_2, 37 °C. **d.** Consuming remaining methanol in the biofilms. Conditions: $E = 0.4$ vs. SHE, pH 7.4, without HCO_3^-, N_2, 37 °C. **e.** Microbial reduction of CO_2 into CH_4 with the IO-ITO|coculture electrode. Grey trace: coculturing *M. barkeri* with an inactivated IO-ITO|coculture electrode. Conditions: $E = -0.4$ V vs. SHE, pH 7.4, N_2:CO_2 (80:20, v:v%), 37 °C.

The potential was judiciously selected to minimise the inference of H_2 evolution whilst maintain electron uptake by *G. sulfurreducens*. 0.93 ± 0.17 μmol CH_4 was detected as the only reduction product, corresponding to Faraday efficiency of $103 \pm 22\%$. No CH_4 was generated with an inactivated IO-ITO|coculture electrode (**Figure 6.6e**, the grey trace).

However, several issues remained in this study: (1) *G. sulfurreducens* and *M. barkeri* cannot be distinguished by SEM imaging (**Figure 6.7**). More efforts are needed to prove the

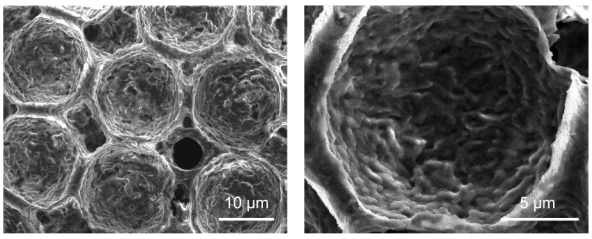

Figure 6.7 SEM images of an IO-ITO|coculture electrode with *G. sulfurreducens* and *M. barkeri*.

presence of *M. barkeri* inside the electrode scaffold, and furthermore, prove the interspecies electron transfer that underlies the syntrophic symbiosis with *G. sulfurreducens*. (2) The reduction current decayed within 10 h, which could arise from the inactivation of bacteria or oxygen inhibition, and needs explanations from further studies. (3) Isotopic-labeling experiments with $^{13}CO_2$ are also required to confirm that the detected CH_4 comes from the CO_2.

6.5 Summary

This chapter demonstrates the application of the bacterium-colonised electrode in chemical synthesis. By virtue of the electron uptake capability, *G. sulfurreducens* can accept electrons from its interfacing IO-ITO scaffold and catalyse the reduction of fumarate to succinate within the cell. In addition, the bacteria can transfer electrons to extracellular GO microsheets, producing RGO at mild reaction conditions. The IO-ITO|*G. sulfurreducens* electrode was further coupled with a photoanode, i.e., IO-TiO_2|**RuP** or $BiVO_4$-CoO_x to generate electrons from light irradiation. At last, methanogenic *M. barkeri* was cocultured with *G. sulfurreducens* in an IO-ITO electrode to drive CO_2 reduction to CH_4 by means of interspecies electron transfer. The syntrophic electrosynthesis takes advantage of the synergistic symbiosis in nature to extended the scope of attainable reactions. This microbial hybrid electrode allows intercellular metabolism to function in concert with extracellular redox transformations via the electrical interplay at the biointerface, and represents a promising strategy to produce high-value chemicals with renewable sources.

Chapter 7

Conclusions

7.1 Thesis summary

The research works presented in this thesis are part of the ongoing explorations in semi-artificial photosynthesis to realise solar-to-chemical conversion in an efficient, selective, and productive manner. This was achieved by integrating biocatalysts in the form of enzymes or microbes into electrode scaffolds with tailored structures. In particular, I developed an array of inverse opal-structured electrodes to host photosynthetic enzymes and electroactive bacteria (**Figure 7.1**), to carry out redox reactions that would otherwise be challenging to pursue with synthetic chemistry, with the aid of photoelectrochemistry.

The IO-electrodes were prepared by a coassembly method with PS beads as the structural template. Changing the size of PS beads, the electrode's macroporosity can be varied to suit biocatalysts with different dimensions. In this thesis, I have made IO-ITO electrodes with 750 nm, 3 μm, 10 μm and 20 μm macropores. 750 nm and 3 μm IO-ITO electrodes were used to host nanosized PSII for PF-PEC, while 10 μm and 20 μm IO-ITO electrodes were employed to culture bacteria with micrometre footprints for microbial electrogenesis and electrosynthesis. Macropores in these electrodes were interconnected allowing biocatalysts to penetrate inside the scaffold. Another dimension of the structure is mesoporosity that is assembled by building blocks such as ITO nanoparticles and GO sheets. The mesoporosity forms the surface directly in contact with the biocatalysts and can be varied through the particle size or concentration of the GO solution. The electrode morphology plays a crucial role in dictating the interaction and electronic communication with biocatalysts. In light of this, Chapter 3 looked into the impact of these morphological changes on the activity of light-driven biocatalysis, in a model biohybrid system consisting of PSII and the IO-ITO electrode. An array of IO-ITO electrodes

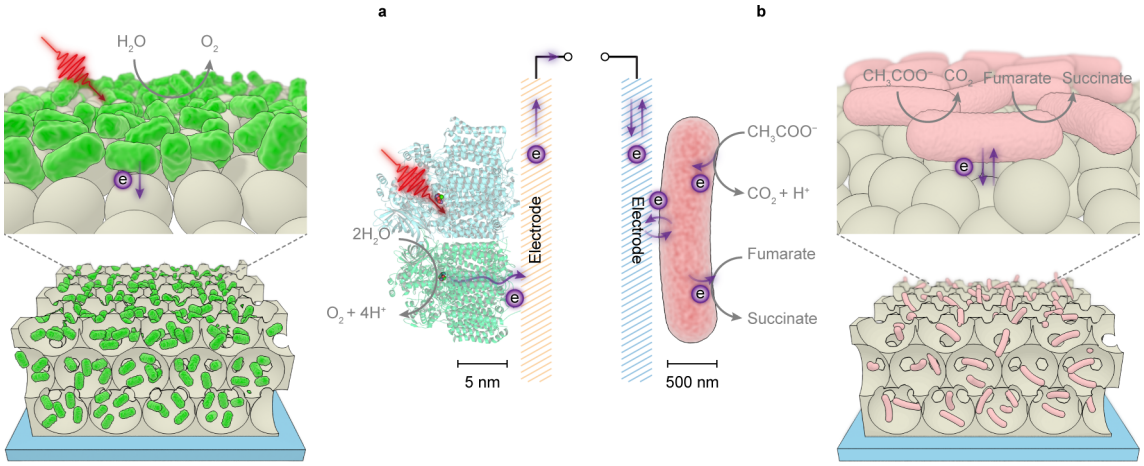

Figure 7.1 Interfacing PSII (**a**) and *G. sulfurreducens* (**b**) with IO-ITO electrodes for semi-artificial photosynthesis

with different macro- and mesostructures were prepared and subsequently loaded with PSII for PEC investigations. PSII in the IO-ITO scaffold was quantified by UV–vis spectroscopy and visualised by confocal fluorescence microscopy, which generated the correlation between the protein loading capacity with electrode structures. Furthermore, in situ ATR-IR was employed to probe the protein adsorption and desorption in the IO-ITO scaffold and shed light on the nature of the protein-material interaction at the interface. Studies in protein integration in the electrode revealed a two-fold interaction between PSII and the IO-ITO scaffold: PSII was physically trapped within the mesopores formed by ITO nanoparticles and electrostatically adsorbed on the electrode surface. The photocurrent measured by PF-PEC proportionally correlated with the protein loading, giving rise to similar TOFs. 750 nm IO-ITO electrode made from polydispersed nanoparticles stood out as the best-performing electrode in terms of high protein loading and photocurrent. The notable disparity between DET and MET signified that a major limitation in enzymatic photocatalysis resided in the electronic coupling between proteins and electrode surfaces, which is susceptible to random enzyme orientations. The structure-activity relationship established here suggests that structural optimisation may further enhance the protein loading, but has limited contribution to the improvement of photoactivity that hinges on the electrical wiring and light transmission within electrodes. The lessons learned in this chapter provide additional knowledge to the field where the protein-electrode interaction was poorly understood, and hopefully can shift the emphasis from structure design to interface engineering, when seeking better in vitro enzymatic activity in artificial environments. The methodology developed in this chapter can be applied for further interrogations into similar biohybrid systems with state-of-the-art analytical techniques.

In addition to conducting metal oxide (ITO), I also utilised RGO as the electrode material by virtue of its widely-appreciated high surface area and versatile surface chemistry. Chapter 4 investigated the PSII in IO-graphene electrodes following a similar paradigm with Chapter 3. Nevertheless, IO-graphene electrodes generally underperformed in protein loading capacity and PF-PEC compared with their ITO counterparts, due to structural flaws preventing protein penetration and light absorption by RGO attenuating excitations. It is concluded that RGO electrodes are not suitable as the platform to underpin the PF-PEC of photoactive enzymes.

Both PSII-ITO and PSII-graphene hybrid electrodes endured light-induced degradation in performance that lasted for less than 10 min, which is a reflection of a general drawback of enzymatic hybrid systems arising from enzyme fragility. In light of this, I turned to another form of biocatalysts—whole cells that include biosynthetic pathways as an entirety within the cell envelop. I chose *G. sulfurreducens* as the model bacterium because of its naturally-evolved mechanisms to discharge electrons to insoluble electron acceptors. This allows positively-poised electrodes to substitute for natural minerals as artificial electron acceptors and provide conductive scaffolds for microbial proliferation. To this end, Chapter 5 employed IO-ITO electrodes with 10 μm macropores to accommodate bacterial colonies. The bacterial growth in the IO-ITO was indicated by the continual anodic current arising from anaerobic metabolism, and later examined by FIB-SEM. A benchmark current density of 3 mA cm^{-2} was attained at 0.1 V vs. SHE. Intriguingly, at 0.4 V vs. SHE, the microbial hybrid electrode produced less current (1 mA cm^{-2}). Such potential dependence was investigated by differential gene expression analysis to yield more insights into bacteria's response to the redox potential of electron acceptors. It revealed that bacteria deployed a different metabolic pathway to interact with an electrode and upregulated genes encoding electron-carrying proteins to facilitate the electron transfer toward electrodes. Moreover, a second bacterium *S. loihica* was cocultured with *G. sulfurreducens* in the IO-ITO electrode to produce electricity via syntrophic partnership, which granted the system additional flexibility in using different electron donors.

The anodic culturing primes a hybrid electrode populated by *G. sulfurreducens* that was employed for electrosynthesis in Chapter 6. The electron uptake ability of *G. sulfurreducens* allows direct use of electrons supplied by an electrode to drive reducing reactions within and beyond intrinsic metabolic patterns. Fumarate reduction and GO reduction were selected as model reactions to exemplify this idea. It showed that *G. sulfurreducens* could accept electrons from the cathode and intracellularly reduce fumarate to succinate and extracellularly reduce GO to RGO. To further implement the conception of "photoelectrosynthesis", the microbial hybrid electrode was coupled with a photoanode to outsource the electron supply to photochemistry. IO-TiO_2|**RuP** electrode provided higher driving force for electron transfer

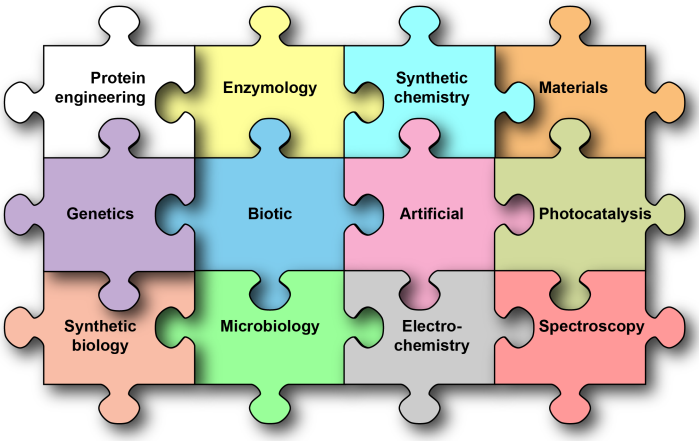

Figure 7.2 Multidisciplinary pattern underling the development of semi-artificial photosynthesis

but required sacrificial electron donors to avoid the kinetically-sluggish water oxidation, while $BiVO_4$-CoO_x electrode could withdraw electrons directly from water but narrowed the margin in energy required to drive the reaction. While the conversion yield and system longevity are not yet high enough for scaled up applications, such proof-of-concept system demonstrates that photoelectrochemistry and biological metabolism can work in synergy via the electrical interplay at biointerfaces for solar-to-chemical conversion. At last, to extend the scope of attainable reactions, methanogenic *M. barkeri* was cocultured into an IO-ITO|*G. sulfurreducens* electrode to drive CO_2 reduction to CH_4 by means of interspecies electron transfer. The syntrophic electrosynthesis takes advantage of the synergistic symbiosis in nature to perform synthetic reactions beyond the repertoire of individual strains of microorganisms.

Taking together, this thesis deals with biohybrid systems that leverage biocatalysis in chemical transformation, and combine strengths of synthetic materials and photoelectrochemistry. This thesis presents a cross-disciplinary approach to tackle pressing issues confronting artificial photosynthesis and synthetic chemistry, and to create avenues in the production of high value fuels and chemicals with renewable energy sources.

7.2 Looking forward

Semi-artificial photosynthesis shifts the paradigm of implementing solar-to-chemical conversion by rationally integrating biocatalysts in the form of proteins and whole cells with synthetic components, which traverses the fields of enzymology, microbiology, materials

science, electrochemistry, and photocatalysis (**Figure 7.2**). The ultimate goal is to catalyse the transformation of CO_2, H_2O, and N_2 into fuels, value-added chemicals and fertilisers via a sustainable path and synthesise complex fine chemicals with high yield and selectivity with renewable energy sources. Within such framework, future possibilities can be generated from the intertwining and expansion of these fields. Here I briefly sketch out several promising opportunities.

At the biotic side, more enzymes or bacteria relevant to fuel/chemical production can be added into the inventory. The methodologies established with model biocatalysts, e.g., electrode design, protein/microbe loading, interface engineering, can be extrapolated to new biocatalysts to create new reaction pathways. For example, **RuP**-TiO_2 particles were first used to adsorb H_2ases for photocatalytic HER.[58,69] The use of the same light absorber was later extended to CODH and FDH for CO_2 reduction.[222,319] CdS nanorods developed for CdS-H_2ase complexes have been employed to drive N_2-to-NH_3 conversion with N_2ases.[320,321] Likewise, CdS nanoparticles have been in situ deposited on the surface of *E. coli* and *M. thermoacetica*.[60,322] It is reasonable to envision that similar strategy can be applied to other acetogens such as *S. ovata* and methanogens like *M. barkeri*. Knowledge extracted from the previous systems also will be useful to guide the design and optimisation of later derivatives.[323]

Biocatalysts are widely-appreciated for their high product selectivity, yet such catalytic prowess is confined to naturally-occurring reactions. This drawback limits their application in synthetic chemistry and biotechnology, but also shapes the stereotype how chemists perceive biocatalysts in general. One way to expand the reaction scope is orchestrating various catalysts, including biotic or synthetic, to drive cascade reactions toward more complex products.[324] An enzyme cascade has been introduced into a tandem PEC cell to reduce CO_2 into methanol.[325] This thesis has exploited the symbiosis of electrotrophs and methanogens to consume exogenous electrons and generate CH_4 from CO_2 (Section 6.4). More opportunities are emerging is this respect to judiciously construct reaction pathways and sensibly direct electron and carbon flux toward desired products.

The second approach arises when advancing genetic techniques interface with enzymology and microbiology. With the derived methodologies, enzymes can be engineered with improved promiscuity and stability. PSII has been introduced with a polyhistidine tag near the stromal side in order to enhance the linkage with Ni-terminated moieties on an electrode surface.[88] Similar surface modification can be envisaged for other enzymes to improve the interaction with light-absorbing materials. Pathways in microorganisms can be altered to maximise the chemical production or heterologously introduced to unlock non-natural

reactions. Metabolic engineering can allow heterotrophic *E. coli* to synthesise sugar from CO_2,[315] and cyanobacteria to drive the reduction of C=C bonds,[326] or produce valuable aromatic compounds directly from CO_2.[327] Engineered microbes conferred additional pathways can work with light absorbers to yield synthetically useful products beyond their natural metabolites.[328] Moreover, genetic toolkit can alter the existing or enable new physiological functionalities on model microorganisms. For example, current production of electrogenic microorganisms can be enhanced by increasing metabolic fluxes, promoting electron shuttle secretion, encouraging the biofilm formation, etc.[329] Heterologous electron conduits have been transplanted into *E. coli* to confer extracellular electron transfer capability.[329,330] *S. oneidensis* has been engineered to metabolise glucose as carbon and energy source.[331] Beyond this, these techniques also provide powerful means to generate insights into the poorly understood questions posed in this thesis with regard to microbial metabolism strategies in response to variations in electron acceptors and pathways for inward electron uptake from electrodes, which, in turn, will facilitate the rational design of next-generation biohybrid systems.

In parallel, progress at the artificial side can be translated into strengths to stimulate the advancement of semi-artificial photosynthesis systems. Development of materials science and synthetic chemistry will provide more opportunities in tuning materials' composition, morphology and property at various levels to improve the interaction with biocatalysts or adapt to different reaction conditions. A recent report demonstrated the application of metal–organic framework to confine FDH within its precisely defined volume and porosity and stabilise enzymatic activity at non-physiological conditions.[332] Metal-organic framework was also employed to encapsulate anaerobic bacteria (*M. thermoacetica*) so as to protect them against oxidative stress arising from irradiation.[333] Such strategy is feasibly applicable to other enzymes or bacteria. Another emerging possibility is to foster interaction with biocatalysts at subentity level, instead of forming heterogeneous biointerfaces. This has been realised by fusing dye molecules with cyt P450 to replace native redox partners,[334] or anchoring Pt nanoparticles with PSI for light-driven H_2 evolution.[335] At subcellular scale, Au nanoclusters or molecular dyes have been exloited to intervene pathways within cells with optical stimulation as bioorthogonal cues for intracellular modulation.[336–338] Furthermore, the intracellular metabolism can be coupled with extracellular redox transformations to in situ manufacture functional materials such as polymers and inorganic particles.[286,339,340] These materials may provide additional benefits to promote extracellular electron transfer or cytoprotection.[340]

Photochemistry provides another thrust in future development. Many photosynthetic biohybrid systems reviewed in this thesis were limited by light absorbers that cannot afford

sufficient driving force to perform reactions, or suffered from continuing degradation faster than the inactivation of biocatalysts. Potential solutions may arise from the iterative cycle of design, synthesis and characterisation in the field of artificial photosynthesis, which yields a variety of photocatalysts with fine-tuned properties and morphologies. Progress in this field can instantly contribute to the construction and optimisation of biohybrid systems. For example, carbon nitride emerged as an attractive visible-light absorber due to its well-fit band structure, low cost, and robustness,[48] and carbon nitride-H_2ase complexes have been shown effective in photocatalytic H_2 production.[341,342] As such, more applications can be anticipated by replacing H_2ase with FDH, or substituting for toxic CdS to interface with acetogenic bacteria. Studies into these newly-derived systems will gain more knowledge of the biotic-abiotic interplay and generate guidelines of the making of better systems.

Lastly, the research in semi-artificial photosynthesis reverberates with the development of analytic techniques (Section: 1.12). Protocols established for probing artificial photocatalytic systems can be applied to study the biohybrid systems in a similar manner. For instance, ATR-IR previously was deployed to track molecular catalysts and reaction intermediates during catalytic cycles,[241] while it also assisted to probe the enzyme-electrode interaction in H_2ase-TiO_2, FDH-TiO_2 and PSII-ITO systems.[105,221,222] Their versatility renders these tools readily transferable to biohybrid assemblies with different formulas, and offers a high degree of flexibility to work in tandem with (photo)electrochemistry for in operando studies. These cutting-edge techniques can also aid in elucidation of fundamental issues with respect to interactions between biological entities and synthetic materials, which are inaccessible by conventional methods. For example, transient absorption spectroscopy was employed to elucidate the kinetics and pathways of electron transfer between H_2ase and CdS,[343] and will be helpful to pinpoint the rate-limiting steps in other enzyme-light absorber systems in biohybrid portfolio, such as H_2ase or FDH with carbon dots, carbon nitride, dye-sensitised TiO_2. This technique has also managed to delineate the inward electron transfer pathways between CdS nanoparticles and *M. thermoacetica*.[323] While the electron uptake mechanisms of other bacteria such as *G. sulfurreducens*, *S. ovata* and *M. barkeri* remain elusive, similar investigations are much needed together with lessons learned from genetic studies to generate a clearer picture of how these bacteria interact with artificial electron donors and utilise electrons to sustain their metabolism. Semi-artificial photosynthesis synergises functional components from different disciplines. Advances in each field will ripple through the rest of the pattern, and yield new opportunities to further the development and implementation of the biohybrid systems. Conclusions drawn from these studies will deepen the current understanding of biology-materials interplay and form concrete steps to expedite the evolution of semi-artificial photosynthesis toward maturity.

I would like to end the thesis by reviewing an article published in 1912 by Giacomo Ciamician, an Italian chemist.[344,345] This article envisages a future where solar energy was utilised to drive synthetic reactions by means of "an artificial photochemical process", and thereby is deemed as the origin of the conception of artificial photosynthesis.

> *"Where vegetation is rich, photochemistry may be left to the plants and, by rational cultivation, solar radiation may be used for industrial purposes. In the desert regions, unsuitable to any kind of cultivation, photochemistry will artificially put their solar energy to practical uses.*
>
> *On the arid lands there will spring up industrial colonies without smoke and without smokestacks ; forests of glass tubes will extend over the plants and glass buildings will rise everywhere ; inside of these will take place the photochemical processes that hitherto have been the guarded secret of the plants, but that will have been mastered by human industry which will know how to make them bear even more abundant fruit than nature, for nature is not in a hurry and mankind is. And if in a distant future the supply of coal becomes completely exhausted, civilization will not be checked by that, for life and civilization will continue as long as the sun shines!"*

In a sense, Ciamician's prophecy has come true: his visions of the future seem much like a typical chemical laboratory working at artificial photosynthesis where this thesis was completed, and I hope this thesis has demonstrated how solar energy can be put to practical uses with "the guarded secret of the plants".

References

[1] P. K. Nayak, S. Mahesh, H. J. Snaith, D. Cahen, *Nat. Rev. Mater.* **2019**, *4*, 269–285.

[2] A. Polman, M. Knight, E. C. Garnett, B. Ehrler, W. C. Sinke, *Science* **2016**, *352*, aad4424.

[3] Y. Tachibana, L. Vayssieres, J. R. Durrant, *Nat. Photon.* **2012**, *6*, 511–518.

[4] J. H. Montoya, L. C. Seitz, P. Chakthranont, A. Vojvodic, T. F. Jaramillo, J. K. Nørskov, *Nat. Mater.* **2017**, *16*, 70–81.

[5] N. Nelson, A. Ben-Shem, *Nat. Rev. Mol. Cell Biol.* **2004**, *5*, 971–982.

[6] R. E. Blankenship, *Molecular Mechanisms of Photosynthesis, 2nd Edition*, Wiley-Blackwell, **2014**.

[7] G. G. B. Tcherkez, G. D. Farquhar, T. J. Andrews, *Proc. Natl. Acad. Sci. U.S.A* **2006**, *103*, 7246–7251.

[8] T. J. Erb, J. Zarzycki, *Curr. Opin. Biotechnol.* **2018**, *49*, 100–107.

[9] M. Hagemann, H. Bauwe, *Curr. Opin. Chem. Biol.* **2016**, *35*, 109–116.

[10] R. Croce, H. van Amerongen, *Nat. Chem. Biol.* **2014**, *10*, 492–501.

[11] X.-G. Zhu, S. P. Long, D. R. Ort, *Annu. Rev. Plant Biol.* **2010**, *61*, 235–261.

[12] R. E. Blankenship, D. M. Tiede, J. Barber, G. W. Brudvig, G. Fleming, M. Ghirardi, M. R. Gunner, W. Junge, D. M. Kramer, A. Melis, T. A. Moore, C. C. Moser, D. G. Nocera, A. J. Nozik, D. R. Ort, W. W. Parson, R. C. Prince, R. T. Sayre, *Science* **2011**, *332*, 805–809.

[13] X.-G. Zhu, S. P. Long, D. R. Ort, *Curr. Opin. Biotechnol.* **2008**, *19*, 153–159.

[14] A. Fujishima, K. Honda, *Nature* **1972**, *238*, 37–38.

[15] M. G. Walter, E. L. Warren, J. R. McKone, S. W. Boettcher, Q. Mi, E. A. Santori, N. S. Lewis, *Chem. Rev.* **2010**, *110*, 6446–6473.

[16] S. Chen, L.-W. Wang, *Chem. Mater.* **2012**, *24*, 3659–3666.

[17] K. Sivula, R. van de Krol, *Nat. Rev. Mater.* **2016**, *1*, 15010.

[18] K. Maeda, K. Domen, *J. Phys. Chem. C* **2007**, *111*, 7851–7861.

[19] K. Maeda, *ACS Catal.* **2013**, *3*, 1486–1503.

[20] R. Kobayashi, T. Takashima, S. Tanigawa, S. Takeuchi, B. Ohtani, H. Irie, *Phys. Chem. Chem. Phys.* **2016**, *18*, 27754–27760.

[21] S. Chen, T. Takata, K. Domen, *Nat. Rev. Mater.* **2017**, *2*, 17050.

[22] K. Maeda, M. Higashi, D. Lu, R. Abe, K. Domen, *J. Am. Chem. Soc.* **2010**, *132*, 5858–5868.

[23] A. Iwase, Y. H. Ng, Y. Ishiguro, A. Kudo, R. Amal, *J. Am. Chem. Soc.* **2011**, *133*, 11054–11057.

[24] Y. Sasaki, H. Kato, A. Kudo, *J. Am. Chem. Soc.* **2013**, *135*, 5441–5449.

[25] S. Keene, R. Bala Chandran, S. Ardo, *Energy Environ. Sci.* **2019**, *12*, 261–272.

[26] D. M. Fabian, S. Hu, N. Singh, F. A. Houle, T. Hisatomi, K. Domen, F. E. Osterloh, S. Ardo, *Energy Environ. Sci.* **2015**, *8*, 2825–2850.

[27] Q. Wang, T. Hisatomi, Q. Jia, H. Tokudome, M. Zhong, C. Wang, Z. Pan, T. Takata, M. Nakabayashi, N. Shibata, Y. Li, I. D. Sharp, A. Kudo, T. Yamada, K. Domen, *Nat. Mater.* **2016**, *15*, 611–615.

[28] J. Luo, J.-H. Im, M. T. Mayer, M. Schreier, M. K. Nazeeruddin, N.-G. Park, S. D. Tilley, H. J. Fan, M. Grätzel, *Science* **2014**, *345*, 1593–1596.

[29] C. R. Cox, J. Z. Lee, D. G. Nocera, T. Buonassisi, *Proc. Natl. Acad. Sci. U.S.A* **2014**, *111*, 14057–14061.

[30] E. Pastor, F. Le Formal, M. T. Mayer, S. D. Tilley, L. Francàs, C. A. Mesa, M. Grätzel, J. R. Durrant, *Nat. Commun.* **2017**, *8*, 14280.

[31] O. Zandi, T. W. Hamann, *Nat. Chem.* **2016**, *8*, 778–783.

[32] K. J. Lee, N. Elgrishi, B. Kandemir, J. L. Dempsey, *Nat. Rev. Chem.* **2017**, *1*, 0039.

[33] A. Landman, H. Dotan, G. E. Shter, M. Wullenkord, A. Houaijia, A. Maljusch, G. S. Grader, A. Rothschild, *Nat. Mater.* **2017**, *16*, 646–651.

[34] A. Vilanova, T. Lopes, C. Spenke, M. Wullenkord, A. Mendes, *Energy Storage Mater.* **2018**, *13*, 175–188.

[35] M. R. Singh, K. Papadantonakis, C. Xiang, N. S. Lewis, *Energy Environ. Sci.* **2015**, *8*, 2760–2767.

[36] J. Jin, K. Walczak, M. R. Singh, C. Karp, N. S. Lewis, C. Xiang, *Energy Environ. Sci.* **2014**, *7*, 3371–3380.

[37] D. Kim, K. K. Sakimoto, D. Hong, P. Yang, *Angew. Chem. Int. Ed.* **2015**, *54*, 3259–3266.

[38] J. Liu, Y. Liu, N. Liu, Y. Han, X. Zhang, H. Huang, Y. Lifshitz, S.-T. Lee, J. Zhong, Z. Kang, *Science* **2015**, *347*, 970–974.

[39] A. D. Handoko, F. Wei, Jenndy, B. S. Yeo, Z. W. Seh, *Nat. Catal.* **2018**, *1*, 922–934.

[40] A. M. Appel, J. E. Bercaw, A. B. Bocarsly, H. Dobbek, D. L. DuBois, M. Dupuis, J. G. Ferry, E. Fujita, R. Hille, P. J. A. Kenis, C. A. Kerfeld, R. H. Morris, C. H. F. Peden, A. R. Portis, S. W. Ragsdale, T. B. Rauchfuss, J. N. H. Reek, L. C. Seefeldt, R. K. Thauer, G. L. Waldrop, *Chem. Rev.* **2013**, *113*, 6621–6658.

[41] X. Li, J. Wen, J. Low, Y. Fang, J. Yu, *Sci. China Mater.* **2014**, *57*, 70–100.

[42] X. Chang, T. Wang, J. Gong, *Energy Environ. Sci.* **2016**, *9*, 2177–2196.

[43] R. Kortlever, J. Shen, K. J. P. Schouten, F. Calle-Vallejo, M. T. M. Koper, *J. Phys. Chem. Lett.* **2015**, *6*, 4073–4082.

[44] F. A. Armstrong, J. Hirst, *Proc. Natl. Acad. Sci. U.S.A* **2011**, *108*, 14049.

[45] C. M. Agapakis, P. M. Boyle, P. A. Silver, *Nat. Chem. Biol.* **2012**, *8*, 527–535.

[46] J. W. Lee, D. Na, J. M. Park, J. Lee, S. Choi, S. Y. Lee, *Nat. Chem. Biol.* **2012**, *8*, 536–546.

[47] J. Nielsen, J. D. Keasling, *Cell* **2016**, *164*, 1185–1197.

[48] H. Kasap, C. A. Caputo, B. C. M. Martindale, R. Godin, V. W.-h. Lau, B. V. Lotsch, J. R. Durrant, E. Reisner, *J. Am. Chem. Soc.* **2016**, *138*, 9183–9192.

[49] D. W. Wakerley, M. F. Kuehnel, K. L. Orchard, K. H. Ly, T. E. Rosser, E. Reisner, *Nat. Energy* **2017**, *2*, 17021.

[50] H. Kasap, D. S. Achilleos, A. Huang, E. Reisner, *J. Am. Chem. Soc.* **2018**, *140*, 11604–11607.

[51] T. Uekert, M. F. Kuehnel, D. W. Wakerley, E. Reisner, *Energy Environ. Sci.* **2018**, *11*, 2853–2857.

[52] N. Cox, M. Retegan, F. Neese, D. A. Pantazis, A. Boussac, W. Lubitz, *Science* **2014**, *345*, 804–808.

[53] J. Jia, L. C. Seitz, J. D. Benck, Y. Huo, Y. Chen, J. W. D. Ng, T. Bilir, J. S. Harris, T. F. Jaramillo, *Nat. Commun.* **2016**, *7*, 13237.

[54] X. Zhou, R. Liu, K. Sun, Y. Chen, E. Verlage, S. A. Francis, N. S. Lewis, C. Xiang, *ACS Energy Lett.* **2016**, *1*, 764–770.

[55] L. Buzzetti, G. E. M. Crisenza, P. Melchiorre, *Angew. Chem. Int. Ed.* **2019**, *58*, 3730–3747.

[56] N. Kornienko, N. Heidary, G. Cibin, E. Reisner, *Chem. Sci.* **2018**, *9*, 5322–5333.

[57] N. Kornienko, J. Z. Zhang, K. K. Sakimoto, P. Yang, E. Reisner, *Nat. Nanotechnol.* **2018**, *13*, 890–899.

[58] E. Reisner, D. J. Powell, C. Cavazza, J. C. Fontecilla-Camps, F. A. Armstrong, *J. Am. Chem. Soc.* **2009**, *131*, 18457–18466.

[59] D. Mersch, C.-Y. Lee, J. Z. Zhang, K. Brinkert, J. C. Fontecilla-Camps, A. W. Rutherford, E. Reisner, *J. Am. Chem. Soc.* **2015**, *137*, 8541–8549.

[60] K. K. Sakimoto, A. B. Wong, P. Yang, *Science* **2016**, *351*, 74.

[61] C. Liu, J. J. Gallagher, K. K. Sakimoto, E. M. Nichols, C. J. Chang, M. C. Y. Chang, P. Yang, *Nano Lett.* **2015**, *15*, 3634–3639.

[62] A. Heller, *Acc. Chem. Res.* **1990**, *23*, 128–134.

[63] C. Léger, S. J. Elliott, K. R. Hoke, L. J. C. Jeuken, A. K. Jones, F. A. Armstrong, *Biochemistry* **2003**, *42*, 8653–8662.

[64] W. J. Albery, J. R. Knowles, *Biochemistry* **1976**, *15*, 5631–5640.

[65] A. Warshel, *Proc. Natl. Acad. Sci. U.S.A* **1978**, *75*, 5250.

[66] S. V. Hexter, F. Grey, T. Happe, V. Climent, F. A. Armstrong, *Proc. Natl. Acad. Sci. U.S.A* **2012**, *109*, 11516.

[67] K. A. Vincent, A. Parkin, F. A. Armstrong, *Chem. Rev.* **2007**, *107*, 4366–4413.

[68] F. Lakadamyali, E. Reisner, *Chem. Commun.* **2011**, *47*, 1695–1697.

[69] E. Reisner, J. C. Fontecilla-Camps, F. A. Armstrong, *Chem. Commun.* **2009**, 550–552.

[70] K. P. Sokol, D. Mersch, V. Hartmann, J. Z. Zhang, M. M. Nowaczyk, M. Rögner, A. Ruff, W. Schuhmann, N. Plumeré, E. Reisner, *Energy Environ. Sci.* **2016**, *9*, 3698–3709.

[71] M. Suga, F. Akita, K. Hirata, G. Ueno, H. Murakami, Y. Nakajima, T. Shimizu, K. Yamashita, M. Yamamoto, H. Ago, J.-R. Shen, *Nature* **2015**, *517*, 99–103.

[72] I. D. Young, M. Ibrahim, R. Chatterjee, S. Gul, F. D. Fuller, S. Koroidov, A. S. Brewster, R. Tran, R. Alonso-Mori, T. Kroll, T. Michels-Clark, H. Laksmono, R. G. Sierra, C. A. Stan, R. Hussein, M. Zhang, L. Douthit, M. Kubin, C. de Lichtenberg, L. Vo Pham, H. Nilsson, M. H. Cheah, D. Shevela, C. Saracini, M. A. Bean, I. Seuffert, D. Sokaras, T.-C. Weng, E. Pastor, C. Weninger, T. Fransson, L. Lassalle, P. Bräuer, P. Aller, P. T. Docker, B. Andi, A. M. Orville, J. M. Glownia, S. Nelson, M. Sikorski, D. Zhu, M. S. Hunter, T. J. Lane, A. Aquila, J. E. Koglin, J. Robinson, M. Liang, S. Boutet, A. Y. Lyubimov, M. Uervirojnangkoorn, N. W. Moriarty, D. Liebschner, P. V. Afonine, D. G. Waterman, G. Evans, P. Wernet, H. Dobbek, W. I. Weis, A. T. Brunger, P. H. Zwart, P. D. Adams, A. Zouni, J. Messinger, U. Bergmann, N. K. Sauter, J. Kern, V. K. Yachandra, J. Yano, *Nature* **2016**, *540*, 453–457.

[73] Y. Umena, K. Kawakami, J.-R. Shen, N. Kamiya, *Nature* **2011**, *473*, 55–60.

[74] J.-R. Shen, *Annu. Rev. Plant Biol.* **2015**, *66*, 23–48.

[75] K. N. Ferreira, T. M. Iverson, K. Maghlaoui, J. Barber, S. Iwata, *Science* **2004**, *303*, 1831–1837.

[76] X. Wei, X. Su, P. Cao, X. Liu, W. Chang, M. Li, X. Zhang, Z. Liu, *Nature* **2016**, *534*, 69–74.

[77] L. S. van Bezouwen, S. Caffarri, R. S. Kale, R. Kouřil, A.-M. W. H. Thunnissen, G. T. Oostergetel, E. J. Boekema, *Nat. Plants* **2017**, *3*, 17080.

[78] X. Su, J. Ma, X. Wei, P. Cao, D. Zhu, W. Chang, Z. Liu, X. Zhang, M. Li, *Science* **2017**, *357*, 815–820.

[79] J. Barber, *Chem. Soc. Rev.* **2009**, *38*, 185–196.

[80] R. Croce, H. van Amerongen, *Science* **2017**, *357*, 752.

[81] A. Klauss, M. Haumann, H. Dau, *Proc. Natl. Acad. Sci. U.S.A* **2012**, *109*, 16035–16040.

[82] T. Cardona, A. Sedoud, N. Cox, A. W. Rutherford, *Biochim. Biophys. Acta Bioenerg.* **2012**, *1817*, 26–43.

[83] B. Kok, B. Forbush, M. McGloin, *Photochem. Photobiol.* **1970**, *11*, 457–475.

[84] H. Dau, M. Haumann, *Coord. Chem. Rev.* **2008**, *252*, 273–295.

[85] J. Kern, R. Chatterjee, I. D. Young, F. D. Fuller, L. Lassalle, M. Ibrahim, S. Gul, T. Fransson, A. S. Brewster, R. Alonso-Mori, R. Hussein, M. Zhang, L. Douthit, C. de Lichtenberg, M. H. Cheah, D. Shevela, J. Wersig, I. Seuffert, D. Sokaras, E. Pastor, C. Weninger, T. Kroll, R. G. Sierra, P. Aller, A. Butryn, A. M. Orville, M. Liang, A. Batyuk, J. E. Koglin, S. Carbajo, S. Boutet, N. W. Moriarty, J. M. Holton, H. Dobbek, P. D. Adams, U. Bergmann, N. K. Sauter, A. Zouni, J. Messinger, J. Yano, V. K. Yachandra, *Nature* **2018**, *563*, 421–425.

[86] M. D. Kärkäs, O. Verho, E. V. Johnston, B. Åkermark, *Chem. Rev.* **2014**, *114*, 11863–12001.

[87] Y. Kato, M. Sugiura, A. Oda, T. Watanabe, *Proc. Natl. Acad. Sci. U.S.A* **2009**, *106*, 17365.

[88] N. Terasaki, M. Iwai, N. Yamamoto, T. Hiraga, S. Yamada, Y. Inoue, *Thin Solid Films* **2008**, *516*, 2553–2557.

[89] M. Sugiura, Y. Inoue, *Plant Cell Physiol.* **1999**, *40*, 1219–1231.

[90] D. J. Vinyard, G. M. Ananyev, G. Charles Dismukes, *Annu. Rev. Biochem.* **2013**, *82*, 577–606.

[91] R. de Wijn, H. J. van Gorkom, *Biochemistry* **2001**, *40*, 11912–11922.

[92] N. Murata, S. Takahashi, Y. Nishiyama, S. I. Allakhverdiev, *Biochim. Biophys. Acta Bioenerg.* **2007**, *1767*, 414–421.

[93] S. Takahashi, M. R. Badger, *Trends Plant Sci.* **2011**, *16*, 53–60.

[94] N. Ohnishi, S. I. Allakhverdiev, S. Takahashi, S. Higashi, M. Watanabe, Y. Nishiyama, N. Murata, *Biochemistry* **2005**, *44*, 8494–8499.

[95] Y. Nishiyama, S. I. Allakhverdiev, N. Murata, *Biochim. Biophys. Acta Bioenerg.* **2006**, *1757*, 742–749.

[96] J. Z. Zhang, K. P. Sokol, N. Paul, E. Romero, R. van Grondelle, E. Reisner, *Nat. Chem. Biol.* **2016**, *12*, 1046–1052.

[97] R. Kale, A. E. Hebert, L. K. Frankel, L. Sallans, T. M. Bricker, P. Pospisil, *Proc. Natl. Acad. Sci. U.S.A* **2017**, *114*, 2988–2993.

[98] N. Kornienko, J. Z. Zhang, K. P. Sokol, S. Lamaison, A. Fantuzzi, R. van Grondelle, A. W. Rutherford, E. Reisner, *J. Am. Chem. Soc.* **2018**, *140*, 17923–17931.

[99] C. Zhang, C. Chen, H. Dong, J.-R. Shen, H. Dau, J. Zhao, *Science* **2015**, *348*, 690–693.

[100] S. Ye, C. Ding, R. Chen, F. Fan, P. Fu, H. Yin, X. Wang, Z. Wang, P. Du, C. Li, *J. Am. Chem. Soc.* **2018**, *140*, 3250–3256.

[101] D. Wang, R. N. Sampaio, L. Troian-Gautier, S. L. Marquard, B. H. Farnum, B. D. Sherman, M. V. Sheridan, C. J. Dares, G. J. Meyer, T. J. Meyer, *J. Am. Chem. Soc.* **2019**, *141*, 7926–7933.

[102] Y. Kato, R. Nagao, T. Noguchi, *Proc. Natl. Acad. Sci. U.S.A* **2016**, *113*, 620–625.

[103] M. Kato, J. Z. Zhang, N. Paul, E. Reisner, *Chem. Soc. Rev.* **2014**, *43*, 6485–6497.

[104] A. Agostiano, A. Ceglie, M. D. Monica, *Bioelectrochem. Bioenerg.* **1984**, *12*, 499–507.

[105] X. Fang, K. P. Sokol, N. Heidary, T. A. Kandiel, J. Z. Zhang, E. Reisner, *Nano Lett.* **2019**, *19*, 1844–1850.

[106] K. Brinkert, F. Le Formal, X. Li, J. Durrant, A. W. Rutherford, A. Fantuzzi, *Biochim. Biophys. Acta Bioenerg.* **2016**, *1857*, 1497–1505.

[107] J. Maly, C. Di Meo, M. De Francesco, A. Masci, J. Masojidek, M. Sugiura, A. Volpe, R. Pilloton, *Bioelectrochemistry* **2004**, *63*, 271–275.

[108] J. Maly, J. Krejci, M. Ilie, L. Jakubka, J. Masojidek, R. Pilloton, K. Sameh, P. Steffan, Z. Stryhal, M. Sugiura, *Anal. Bioana. Chem.* **2005**, *381*, 1558–1567.

[109] A. Badura, B. Esper, K. Ataka, C. Grunwald, C. Wöll, J. Kuhlmann, J. Heberle, M. Rögner, *Photochem. Photobiol.* **2006**, *82*, 1385–1390.

[110] A. Ruff, *Curr. Opin. Electrochem.* **2017**, *5*, 66–73.

[111] A. Badura, D. Guschin, B. Esper, T. Kothe, S. Neugebauer, W. Schuhmann, M. Rögner, *Electroanalysis* **2008**, *20*, 1043–1047.

[112] K. K. Rao, D. O. Hall, N. Vlachopoulos, M. Grätzel, M. C. W. Evans, M. Seibert, *J. Photochem. Photobiol. B* **1990**, *5*, 379–389.

[113] W. Wang, Z. Wang, Q. Zhu, G. Han, C. Ding, J. Chen, J.-R. Shen, C. Li, *Chem. Commun.* **2015**, *51*, 16952–16955.

[114] J. Li, X. Feng, J. Fei, P. Cai, J. Huang, J. Li, *J. Mater. Chem. A* **2016**, *4*, 12197–12204.

[115] J. Li, X. Feng, Y. Jia, Y. Yang, P. Cai, J. Huang, J. Li, *J. Mater. Chem. A* **2017**, *5*, 19826–19835.

[116] M. Kato, T. Cardona, A. W. Rutherford, E. Reisner, *J. Am. Chem. Soc.* **2012**, *134*, 8332–8335.

[117] M. Kato, T. Cardona, A. W. Rutherford, E. Reisner, *J. Am. Chem. Soc.* **2013**, *135*, 10610–10613.

[118] C.-Y. Lee, B. Reuillard, K. P. Sokol, T. Laftsoglou, C. W. J. Lockwood, S. F. Rowe, E. T. Hwang, J. C. Fontecilla-Camps, L. J. C. Jeuken, J. N. Butt, E. Reisner, *Chem. Commun.* **2016**, *52*, 7390–7393.

[119] B. Reuillard, K. H. Ly, P. Hildebrandt, L. J. C. Jeuken, J. N. Butt, E. Reisner, *J. Am. Chem. Soc.* **2017**, *139*, 3324–3327.

[120] K. P. Sokol, W. E. Robinson, J. Warnan, N. Kornienko, M. M. Nowaczyk, A. Ruff, J. Z. Zhang, E. Reisner, *Nat. Energy* **2018**, *3*, 944–951.

[121] K. P. Sokol, W. E. Robinson, A. R. Oliveira, J. Warnan, M. M. Nowaczyk, A. Ruff, I. A. C. Pereira, E. Reisner, *J. Am. Chem. Soc.* **2018**, *140*, 16418–16422.

[122] K. R. Stieger, S. C. Feifel, H. Lokstein, M. Hejazi, A. Zouni, F. Lisdat, *J. Mater. Chem. A* **2016**, *4*, 17009–17017.

[123] D. Ciornii, M. Riedel, K. R. Stieger, S. C. Feifel, M. Hejazi, H. Lokstein, A. Zouni, F. Lisdat, *J. Am. Chem. Soc.* **2017**, *139*, 16478–16481.

[124] M. Riedel, W. J. Parak, A. Ruff, W. Schuhmann, F. Lisdat, *ACS Catal.* **2018**, *8*, 5212–5220.

[125] M. Riedel, J. Wersig, A. Ruff, W. Schuhmann, A. Zouni, F. Lisdat, *Angew. Chem. Int. Ed.* **2019**, *58*, 801–805.

[126] J. Z. Zhang, P. Bombelli, K. P. Sokol, A. Fantuzzi, A. W. Rutherford, C. J. Howe, E. Reisner, *J. Am. Chem. Soc.* **2018**, *140*, 6–9.

[127] T. Wenzel, D. Härtter, P. Bombelli, C. J. Howe, U. Steiner, *Nat. Commun.* **2018**, *9*, 1299.

[128] J. D. Benck, B. A. Pinaud, Y. Gorlin, T. F. Jaramillo, *PLOS ONE* **2014**, *9*, e107942.

[129] A. Bachmeier, V. C. C. Wang, T. W. Woolerton, S. Bell, J. C. Fontecilla-Camps, M. Can, S. W. Ragsdale, Y. S. Chaudhary, F. A. Armstrong, *J. Am. Chem. Soc.* **2013**, *135*, 15026–15032.

[130] K. K. Sakimoto, N. Kornienko, P. Yang, *Acc. Chem. Res.* **2017**, *50*, 476–481.

[131] J. Ye, J. Yu, Y. Zhang, M. Chen, X. Liu, S. Zhou, Z. He, *Appl. Catal. B: Environ.* **2019**, *257*, 117916.

[132] D. R. Lovley, T. Ueki, T. Zhang, N. S. Malvankar, P. M. Shrestha, K. A. Flanagan, M. Aklujkar, J. E. Butler, L. Giloteaux, A.-E. Rotaru, D. E. Holmes, A. E. Franks, R. Orellana, C. Risso, K. P. Nevin, R. K. Poole, *Adv. Microbial Physiol.* **2011**, *59*, 1–100.

[133] K. P. Nevin, H. Richter, S. F. Covalla, J. P. Johnson, T. L. Woodard, A. L. Orloff, H. Jia, M. Zhang, D. R. Lovley, *Environ. Microbiol.* **2008**, *10*, 2505–2514.

[134] A. S. Galushko, B. Schink, *Arch. Microbiol.* **2000**, *174*, 314–321.

[135] J. E. Butler, N. D. Young, D. R. Lovley, *BMC Genomics* **2010**, *11*, 40.

[136] T. Zhang, S. M. Gannon, K. P. Nevin, A. E. Franks, D. R. Lovley, *Environ. Microbiol.* **2010**, *12*, 1011–1020.

[137] A. M. Speers, G. Reguera, *Appl. Environ. Microbiol.* **2012**, *78*, 437–444.

[138] R. T. Anderson, H. A. Vrionis, I. Ortiz-Bernad, C. T. Resch, P. E. Long, R. Dayvault, K. Karp, S. Marutzky, D. R. Metzler, A. Peacock, D. C. White, M. Lowe, D. R. Lovley, *Appl. Environ. Microbiol.* **2003**, *69*, 5884–5891.

[139] R. S. Cutting, V. S. Coker, N. D. Telling, R. L. Kimber, C. I. Pearce, B. L. Ellis, R. S. Lawson, G. van der Laan, R. A. D. Pattrick, D. J. Vaughan, E. Arenholz, J. R. Lloyd, *Environ. Sci. Technol.* **2010**, *44*, 2577–2584.

[140] X. Xie, C. Criddle, Y. Cui, *Energy Environ. Sci.* **2015**, *8*, 3418–3441.

[141] H. H. Hau, J. A. Gralnick, *Annu. Rev. Microbiol.* **2007**, *61*, 237–258.

[142] J. F. Heidelberg, I. T. Paulsen, K. E. Nelson, E. J. Gaidos, W. C. Nelson, T. D. Read, J. A. Eisen, R. Seshadri, N. Ward, B. Methe, R. A. Clayton, T. Meyer, A. Tsapin, J. Scott, M. Beanan, L. Brinkac, S. Daugherty, R. T. DeBoy, R. J. Dodson, A. S. Durkin, D. H. Haft, J. F. Kolonay, R. Madupu, J. D. Peterson, L. A. Umayam, O. White, A. M. Wolf, J. Vamathevan, J. Weidman, M. Impraim, K. Lee, K. Berry, C. Lee, J. Mueller, H. Khouri, J. Gill, T. R. Utterback, L. A. McDonald, T. V. Feldblyum, H. O. Smith, J. C. Venter, K. H. Nealson, C. M. Fraser, *Nat. Biotechnol.* **2002**, *20*, 1118–1123.

[143] B. E. Logan, R. Rossi, A. Ragab, P. E. Saikaly, *Nat. Rev. Microbiol.* **2019**, *17*, 307–319.

[144] K. B. Gregory, D. R. Bond, D. R. Lovley, *Environ. Microbiol.* **2004**, *6*, 596–604.

[145] K. B. Gregory, D. R. Lovley, *Environ. Sci. Technol.* **2005**, *39*, 8943–8947.

[146] A. Kumar, L. H.-H. Hsu, P. Kavanagh, F. Barrière, P. N. L. Lens, L. Lapinsonnière, J. H. Lienhard V, U. Schröder, X. Jiang, D. Leech, *Nat. Rev. Chem.* **2017**, *1*, 0024.

[147] Y. Yang, M. Xu, J. Guo, G. Sun, *Process Biochem.* **2012**, *47*, 1707–1714.

[148] B. A. Methé, K. E. Nelson, J. A. Eisen, I. T. Paulsen, W. Nelson, J. F. Heidelberg, D. Wu, M. Wu, N. Ward, M. J. Beanan, R. J. Dodson, R. Madupu, L. M. Brinkac, S. C. Daugherty, R. T. DeBoy, A. S. Durkin, M. Gwinn, J. F. Kolonay, S. A. Sullivan, D. H. Haft, J. Selengut, T. M. Davidsen, N. Zafar, O. White, B. Tran, C. Romero, H. A. Forberger, J. Weidman, H. Khouri, T. V. Feldblyum, T. R. Utterback, S. E. Van Aken, D. R. Lovley, C. M. Fraser, *Science* **2003**, *302*, 1967–1969.

[149] J. R. Lloyd, C. Leang, A. L. H. Myerson, M. V. Coppi, S. Cuifo, B. Methe, S. J. Sandler, D. R. Lovley, *Biochem. J.* **2003**, *369*, 153–161.

[150] K. Inoue, C. Leang, A. E. Franks, T. L. Woodard, K. P. Nevin, D. R. Lovley, *Environ. Microbiol. Rep.* **2011**, *3*, 211–217.

[151] B. M. Fonseca, C. M. Paquete, S. E. Neto, I. Pacheco, C. M. Soares, R. O. Louro, *Biochem. J.* **2013**, *449*, 101.

[152] R. S. Hartshorne, C. L. Reardon, D. Ross, J. Nuester, T. A. Clarke, A. J. Gates, P. C. Mills, J. K. Fredrickson, J. M. Zachara, L. Shi, A. S. Beliaev, M. J. Marshall, M. Tien, S. Brantley, J. N. Butt, D. J. Richardson, *Proc. Natl. Acad. Sci. U.S.A* **2009**, *106*, 22169–22174.

[153] T. A. Clarke, M. J. Edwards, A. J. Gates, A. Hall, G. F. White, J. Bradley, C. L. Reardon, L. Shi, A. S. Beliaev, M. J. Marshall, Z. Wang, N. J. Watmough, J. K. Fredrickson, J. M. Zachara, J. N. Butt, D. J. Richardson, *Proc. Natl. Acad. Sci. U.S.A* **2011**, *108*, 9384–9389.

[154] L. Shi, H. Dong, G. Reguera, H. Beyenal, A. Lu, J. Liu, H.-Q. Yu, J. K. Fredrickson, *Nat. Rev. Microbiol.* **2016**, *14*, 651–662.

[155] G. Reguera, K. D. McCarthy, T. Mehta, J. S. Nicoll, M. T. Tuominen, D. R. Lovley, *Nature* **2005**, *435*, 1098–1101.

[156] Y. A. Gorby, S. Yanina, J. S. McLean, K. M. Rosso, D. Moyles, A. Dohnalkova, T. J. Beveridge, I. S. Chang, B. H. Kim, K. S. Kim, D. E. Culley, S. B. Reed, M. F. Romine, D. A. Saffarini, E. A. Hill, L. Shi, D. A. Elias, D. W. Kennedy, G. Pinchuk, K. Watanabe, S. Ishii, B. Logan, K. H. Nealson, J. K. Fredrickson, *Proc. Natl. Acad. Sci. U.S.A* **2006**, *103*, 11358–11363.

[157] F. Wang, Y. Gu, J. P. O'Brien, S. M. Yi, S. E. Yalcin, V. Srikanth, C. Shen, D. Vu, N. L. Ing, A. I. Hochbaum, E. H. Egelman, N. S. Malvankar, *Cell* **2019**, *177*, 361–369.e10.

[158] S. Pirbadian, S. E. Barchinger, K. M. Leung, H. S. Byun, Y. Jangir, R. A. Bouhenni, S. B. Reed, M. F. Romine, D. A. Saffarini, L. Shi, Y. A. Gorby, J. H. Golbeck, M. Y. El-Naggar, *Proc. Natl. Acad. Sci. U.S.A* **2014**, *111*, 12883.

[159] P. Subramanian, S. Pirbadian, M. Y. El-Naggar, G. J. Jensen, *Proc. Natl. Acad. Sci. U.S.A* **2018**, *115*, E3246.

[160] E. Marsili, D. B. Baron, I. D. Shikhare, D. Coursolle, J. A. Gralnick, D. R. Bond, *Proc. Natl. Acad. Sci. U.S.A* **2008**, *105*, 3968–3973.

[161] H. von Canstein, J. Ogawa, S. Shimizu, J. R. Lloyd, *Appl. Environ. Microbiol.* **2008**, *74*, 615–623.

[162] N. J. Kotloski, J. A. Gralnick, D. K. Newman, *mBio* **2013**, *4*, e00553–12.

[163] A. K. Marcus, B. E. Rittmann, H.-S. Lee, P. Parameswaran, R. Krajmalnik-Brown, C. I. Torres, *FEMS Microbiol. Rev.* **2010**, *34*, 3–17.

[164] M. C. Potter, *Proc. R. Soc. Lond. B Biol. Sci.* **1911**, *84*, 260–276.

[165] B. E. Logan, K. Rabaey, *Science* **2012**, *337*, 686–690.

[166] N. Lebedev, S. M. Strycharz-Glaven, L. M. Tender, *Front. Energy Res.* **2014**, *2*, 34.

[167] S. M. Strycharz-Glaven, R. M. Snider, A. Guiseppi-Elie, L. M. Tender, *Energy Environ. Sci.* **2011**, *4*, 4366–4379.

[168] N. S. Malvankar, M. T. Tuominen, D. R. Lovley, *Energy Environ. Sci.* **2012**, *5*, 6247–6249.

[169] S. M. Strycharz-Glaven, L. M. Tender, *Energy Environ. Sci.* **2012**, *5*, 6250–6255.

[170] N. S. Malvankar, S. E. Yalcin, M. T. Tuominen, D. R. Lovley, *Nat. Nanotechnol.* **2014**, *9*, 1012–1017.

[171] M. D. Yates, S. M. Strycharz-Glaven, J. P. Golden, J. Roy, S. Tsoi, J. S. Erickson, M. Y. El-Naggar, S. C. Barton, L. M. Tender, *Nat. Nanotechnol.* **2016**, *11*, 910–913.

[172] R. M. Snider, S. M. Strycharz-Glaven, S. D. Tsoi, J. S. Erickson, L. M. Tender, *Proc. Natl. Acad. Sci. U.S.A* **2012**, *109*, 15467–15472.

[173] S. Pirbadian, M. Y. El-Naggar, *Phys. Chem. Chem. Phys.* **2012**, *14*, 13802–13808.

[174] M. D. Yates, J. P. Golden, J. Roy, S. M. Strycharz-Glaven, S. Tsoi, J. S. Erickson, M. Y. El-Naggar, S. Calabrese Barton, L. M. Tender, *Phys. Chem. Chem. Phys.* **2015**, *17*, 32564–32570.

[175] D. R. Bond, S. M. Strycharz-Glaven, L. M. Tender, C. I. Torres, *ChemSusChem* **2012**, *5*, 1099–1105.

[176] L. A. Zacharoff, M. Y. El-Naggar, *Curr. Opin. Electrochem.* **2017**, *4*, 182–189.

[177] L. Robuschi, J. P. Tomba, G. D. Schrott, P. S. Bonanni, P. M. Desimone, J. P. Busalmen, *Angew. Chem. Int. Ed.* **2013**, *52*, 925–928.

[178] A. E. Franks, K. P. Nevin, H. Jia, M. Izallalen, T. L. Woodard, D. R. Lovley, *Energy Environ. Sci.* **2009**, *2*, 113–119.

[179] A. E. Franks, R. H. Glaven, D. R. Lovley, *ChemSusChem* **2012**, *5*, 1092–1098.

[180] S. M. Strycharz, A. P. Malanoski, R. M. Snider, H. Yi, D. R. Lovley, L. M. Tender, *Energy Environ. Sci.* **2011**, *4*, 896–913.

[181] Y. Liu, D. R. Bond, *ChemSusChem* **2012**, *5*, 1047–1053.

[182] K. Rabaey, R. Rozendal, *Nat. Rev. Microbiol.* **2010**, *8*, 706–716.

[183] D. R. Lovley, *Environ. Microbiol. Rep.* **2011**, *3*, 27–35.

[184] S. Li, C. Cheng, A. Thomas, *Adv. Mater.* **2017**, *29*, 1602547.

[185] K. K. Sakimoto, N. Kornienko, S. Cestellos-Blanco, J. Lim, C. Liu, P. Yang, *J. Am. Chem. Soc.* **2018**, *140*, 1978–1985.

[186] S. M. Strycharz, R. H. Glaven, M. V. Coppi, S. M. Gannon, L. A. Perpetua, A. Liu, K. P. Nevin, D. R. Lovley, *Bioelectrochemistry* **2011**, *80*, 142–150.

[187] D. E. Ross, J. M. Flynn, D. B. Baron, J. A. Gralnick, D. R. Bond, *PLOS ONE* **2011**, *6*, e16649.

[188] Y.-C. Yong, Y.-Y. Yu, X. Zhang, H. Song, *Angew. Chem. Int. Ed.* **2014**, *53*, 4480–4483.

[189] S. M. Strycharz, T. L. Woodard, J. P. Johnson, K. P. Nevin, R. A. Sanford, F. E. Löffler, D. R. Lovley, *Appl. Environ. Microbiol.* **2008**, *74*, 5943–5947.

[190] S. M. Strycharz, S. M. Gannon, A. R. Boles, A. E. Franks, K. P. Nevin, D. R. Lovley, *Environ. Microbiol. Rep.* **2010**, *2*, 289–294.

[191] Y.-C. Yong, X.-C. Dong, M. B. Chan-Park, H. Song, P. Chen, *ACS Nano* **2012**, *6*, 2394–2400.

[192] Y. Zhao, K. Watanabe, R. Nakamura, S. Mori, H. Liu, K. Ishii, K. Hashimoto, *Chem. Eur. J.* **2010**, *16*, 4982–4985.

[193] C. Ding, H. Liu, Y. Zhu, M. Wan, L. Jiang, *Energy Environ. Sci.* **2012**, *5*, 8517–8522.

[194] R. Bian, Y. Jiang, Y. Wang, J.-K. Sun, J. Hu, L. Jiang, H. Liu, *Adv. Funct. Mater.* **2018**, *28*, 1707408.

[195] K. Katuri, M. L. Ferrer, M. C. Gutiérrez, R. Jiménez, F. del Monte, D. Leech, *Energy Environ. Sci.* **2011**, *4*, 4201–4210.

[196] X. Xie, M. Ye, L. Hu, N. Liu, J. R. McDonough, W. Chen, H. N. Alshareef, C. S. Criddle, Y. Cui, *Energy Environ. Sci.* **2012**, *5*, 5265–5270.

[197] X. Xie, G. Yu, N. Liu, Z. Bao, C. S. Criddle, Y. Cui, *Energy Environ. Sci.* **2012**, *5*, 6862–6866.

[198] S. Zhao, Y. Li, H. Yin, Z. Liu, E. Luan, F. Zhao, Z. Tang, S. Liu, *Sci. Adv.* **2015**, *1*, e1500372.

[199] D. R. Bond, D. R. Lovley, *Appl. Environ. Microbiol.* **2003**, *69*, 1548–1555.

[200] S. K. Chaudhuri, D. R. Lovley, *Nat. Biotechnol.* **2003**, *21*, 1229–1232.

[201] X. Xie, L. Hu, M. Pasta, G. F. Wells, D. Kong, C. S. Criddle, Y. Cui, *Nano Lett.* **2011**, *11*, 291–296.

[202] J. Luo, H. D. Jang, T. Sun, L. Xiao, Z. He, A. P. Katsoulidis, M. G. Kanatzidis, J. M. Gibson, J. Huang, *ACS Nano* **2011**, *5*, 8943–8949.

[203] X.-W. Liu, X.-F. Sun, Y.-X. Huang, G.-P. Sheng, S.-G. Wang, H.-Q. Yu, *Energy Environ. Sci.* **2011**, *4*, 1422–1427.

[204] X. Xie, W. Zhao, H. R. Lee, C. Liu, M. Ye, W. Xie, B. Cui, C. S. Criddle, Y. Cui, *ACS Nano* **2014**, *8*, 11958–11965.

[205] A. Baudler, I. Schmidt, M. Langner, A. Greiner, U. Schröder, *Energy Environ. Sci.* **2015**, *8*, 2048–2055.

[206] D. Massazza, R. Parra, J. P. Busalmen, H. E. Romeo, *Energy Environ. Sci.* **2015**, *8*, 2707–2712.

[207] S. Zhou, J. Tang, Y. Yuan, G. Yang, B. Xing, *Environ. Sci. Technol. Lett.* **2018**, *5*, 564–570.

[208] C. Zhao, P. Gai, C. Liu, X. Wang, H. Xu, J. Zhang, J.-J. Zhu, *J. Mater. Chem. A* **2013**, *1*, 12587–12594.

[209] G. Gnana kumar, C. J. Kirubaharan, S. Udhayakumar, C. Karthikeyan, K. S. Nahm, *Ind. Eng. Chem. Res.* **2014**, *53*, 16883–16893.

[210] C.-e. Zhao, W.-J. Wang, D. Sun, X. Wang, J.-R. Zhang, J.-J. Zhu, *Chem. Eur. J.* **2014**, *20*, 7091–7097.

[211] R. Wang, M. Yan, H. Li, L. Zhang, B. Peng, J. Sun, D. Liu, S. Liu, *Adv. Mater.* **2018**, *30*, 1800618.

[212] J. S. McLean, G. Wanger, Y. A. Gorby, M. Wainstein, J. McQuaid, S. Ishii, O. Bretschger, H. Beyenal, K. H. Nealson, *Environ. Sci. Technol.* **2010**, *44*, 2721–2727.

[213] X. Jiang, J. Hu, E. R. Petersen, L. A. Fitzgerald, C. S. Jackan, A. M. Lieber, B. R. Ringeisen, C. M. Lieber, J. C. Biffinger, *Nat. Commun.* **2013**, *4*, 2751.

[214] B. J. Gross, M. Y. El-Naggar, *Rev. Sci. Instrum.* **2015**, *86*, 064301.

[215] N. Kornienko, K. H. Ly, W. E. Robinson, N. Heidary, J. Z. Zhang, E. Reisner, *Acc. Chem. Res.* **2019**, *52*, 1439–1448.

[216] E. Marsili, J. B. Rollefson, D. B. Baron, R. M. Hozalski, D. R. Bond, *Appl. Environ. Microbiol.* **2008**, *74*, 7329–7337.

[217] M. del Barrio, M. Sensi, C. Orain, C. Baffert, S. Dementin, V. Fourmond, C. Léger, *Acc. Chem. Res.* **2018**, *51*, 769–777.

[218] H. Richter, K. P. Nevin, H. Jia, D. A. Lowy, D. R. Lovley, L. M. Tender, *Energy Environ. Sci.* **2009**, *2*, 506–516.

[219] T. Reda, J. Hirst, *J. Phys. Chem. B* **2006**, *110*, 1394–1404.

[220] A. Barth, *Biochim. Biophys. Acta Bioenerg.* **2007**, *1767*, 1073–1101.

[221] D. H. Nam, J. Z. Zhang, V. Andrei, N. Kornienko, N. Heidary, A. Wagner, K. Nakanishi, K. P. Sokol, B. Slater, I. Zebger, S. Hofmann, J. C. Fontecilla-Camps, C. B. Park, E. Reisner, *Angew. Chem. Int. Ed.* **2018**, *57*, 10595–10599.

[222] M. Miller, W. E. Robinson, A. R. Oliveira, N. Heidary, N. Kornienko, J. Warnan, I. A. C. Pereira, E. Reisner, *Angew. Chem. Int. Ed.* **2019**, *58*, 4601–4605.

[223] E. Siebert, M. Horch, Y. Rippers, J. Fritsch, S. Frielingsdorf, O. Lenz, F. Velazquez Escobar, F. Siebert, L. Paasche, U. Kuhlmann, F. Lendzian, M.-A. Mroginski, I. Zebger, P. Hildebrandt, *Angew. Chem. Int. Ed.* **2013**, *52*, 5162–5165.

[224] M. Horch, J. Schoknecht, M. A. Mroginski, O. Lenz, P. Hildebrandt, I. Zebger, *J. Am. Chem. Soc.* **2014**, *136*, 9870–9873.

[225] T. Sasaki, Y. Endo, M. Nakaya, K. Kanie, A. Nagatomi, K. Tanoue, R. Nakamura, A. Muramatsu, *J. Mater. Chem.* **2010**, *20*, 8153–8157.

[226] H. Sun, X. You, J. Deng, X. Chen, Z. Yang, J. Ren, H. Peng, *Adv. Mater.* **2014**, *26*, 2868–2873.

[227] M. Zhong, T. Hisatomi, T. Minegishi, H. Nishiyama, M. Katayama, T. Yamada, K. Domen, *J. Mater. Chem. A* **2016**, *4*, 9858–9864.

[228] H. Kuhl, J. Kruip, A. Seidler, A. Krieger-Liszkay, M. Bünker, D. Bald, A. J. Scheidig, M. Rögner, *J. Biol. Chem.* **2000**, *275*, 20652–20659.

[229] A. Sedoud, L. Kastner, N. Cox, S. El-Alaoui, D. Kirilovsky, A. W. Rutherford, *Biochim. Biophys. Acta Bioenerg.* **2011**, *1807*, 216–226.

[230] A. Boussac, F. Rappaport, P. Carrier, J.-M. Verbavatz, R. Gobin, D. Kirilovsky, A. W. Rutherford, M. Sugiura, *J. Biol. Chem.* **2004**, *279*, 22809–22819.

[231] R. J. Porra, W. A. Thompson, P. E. Kriedemann, *Biochim. Biophys. Acta Bioenerg.* **1989**, *975*, 384–394.

[232] M. Estevez-Canales, A. Kuzume, Z. Borjas, M. Füeg, D. Lovley, T. Wandlowski, A. Esteve-Núñez, *Environ. Microbiol. Rep.* **2015**, *7*, 219–226.

[233] M. M. Bradford, *Anal. Biochem.* **1976**, *72*, 248–254.

[234] P. Simon, Y. Gogotsi, *Nat. Mater.* **2008**, *7*, 845–854.

[235] H. Kim, C. M. Gilmore, A. Piqué, J. S. Horwitz, H. Mattoussi, H. Murata, Z. H. Kafafi, D. B. Chrisey, *J. Appl. Phys.* **1999**, *86*, 6451–6461.

[236] M. Mierzwa, E. Lamouroux, A. Walcarius, M. Etienne, *Electroanalysis* **2018**, *30*, 1241–1258.

[237] N. R. Neale, B. G. Lee, S. H. Kang, A. J. Frank, *J. Phys. Chem. C* **2011**, *115*, 14341–14346.

[238] J. I. L. Chen, G. von Freymann, V. Kitaev, G. A. Ozin, *J. Am. Chem. Soc.* **2007**, *129*, 1196–1202.

[239] P. O. Saboe, E. Conte, M. Farell, G. C. Bazan, M. Kumar, *Energy Environ. Sci.* **2017**, *10*, 14–42.

[240] S. E. Glassford, B. Byrne, S. G. Kazarian, *Biochim. Biophys. Acta Proteins Proteom.* **2013**, *1834*, 2849–2858.

[241] B. Reuillard, K. H. Ly, T. E. Rosser, M. F. Kuehnel, I. Zebger, E. Reisner, *J. Am. Chem. Soc.* **2017**, *139*, 14425–14435.

[242] R. J. Dennenberg, P. A. Jursinic, S. A. McCarthy, *Biochim. Biophys. Acta Bioenerg.* **1986**, *852*, 222–233.

[243] N. G. Bukhov, G. Sridharan, E. A. Egorova, R. Carpentier, *Biochim. Biophys. Acta Bioenerg.* **2003**, *1604*, 115–123.

[244] Y. Zhu, S. Murali, W. Cai, X. Li, J. W. Suk, J. R. Potts, R. S. Ruoff, *Advanced Materials* **2010**, *22*, 3906–3924.

[245] A. Bianco, H.-M. Cheng, T. Enoki, Y. Gogotsi, R. H. Hurt, N. Koratkar, T. Kyotani, M. Monthioux, C. R. Park, J. M. D. Tascon, J. Zhang, *Carbon* **2013**, *65*, 1–6.

[246] J. Zhang, F. Zhang, H. Yang, X. Huang, H. Liu, J. Zhang, S. Guo, *Langmuir* **2010**, *26*, 6083–6085.

[247] Q. Zeng, J. Cheng, L. Tang, X. Liu, Y. Liu, J. Li, J. Jiang, *Adv. Funct. Mater.* **2010**, *20*, 3366–3372.

[248] M. V. A. Martins, A. R. Pereira, R. A. S. Luz, R. M. Iost, F. N. Crespilho, *Phys. Chem. Chem. Phys.* **2014**, *16*, 17426–17436.

[249] S. Alwarappan, R. K. Joshi, M. K. Ram, A. Kumar, *Appl. Phys. Lett.* **2010**, *96*, 263702.

[250] F. Zhang, B. Zheng, J. Zhang, X. Huang, H. Liu, S. Guo, J. Zhang, *J. Phys. Chem. C* **2010**, *114*, 8469–8473.

[251] D. Cui, L. Mi, X. Xu, J. Lu, J. Qian, S. Liu, *Langmuir* **2014**, *30*, 11833–11840.

[252] M. Gong, P. Adhikari, Y. Gong, T. Wang, Q. Liu, B. Kattel, W.-Y. Ching, W.-L. Chan, J. Z. Wu, *Adv. Funct. Mater.* **2018**, *28*, 1704797.

[253] D. Zhao, L. Li, J. Zhou, *Appl. Surf. Sci.* **2018**, *428*, 825–834.

[254] T. Xue, B. Peng, M. Xue, X. Zhong, C.-Y. Chiu, S. Yang, Y. Qu, L. Ruan, S. Jiang, S. Dubin, R. B. Kaner, J. I. Zink, M. E. Meyerhoff, X. Duan, Y. Huang, *Nat. Commun.* **2014**, *5*, 3200.

[255] K. Iwashina, A. Iwase, Y. H. Ng, R. Amal, A. Kudo, *J. Am. Chem. Soc.* **2015**, *137*, 604–607.

[256] V. C. Tung, M. J. Allen, Y. Yang, R. B. Kaner, *Nat. Nanotechnol.* **2009**, *4*, 25–29.

[257] S. Park, R. S. Ruoff, *Nat. Nanotechnol.* **2009**, *4*, 217–224.

[258] J. Liu, J. Tang, J. J. Gooding, *J. Mater. Chem.* **2012**, *22*, 12435–12452.

[259] N. Yousefi, X. Lu, M. Elimelech, N. Tufenkji, *Nat. Nanotechnol.* **2019**, *14*, 107–119.

[260] N. Paul, PhD thesis, University of Cambridge, **2015**.

[261] J.-L. Shi, W.-C. Du, Y.-X. Yin, Y.-G. Guo, L.-J. Wan, *J. Mater. Chem. A* **2014**, *2*, 10830–10834.

[262] J. Ma, J. Wang, Y.-S. He, X.-Z. Liao, J. Chen, J.-Z. Wang, T. Yuan, Z.-F. Ma, *J. Mater. Chem. A* **2014**, *2*, 9200–9207.

[263] Z. Chen, W. Ren, L. Gao, B. Liu, S. Pei, H.-M. Cheng, *Nat. Mater.* **2011**, *10*, 424–428.

[264] Y. Ito, Y. Tanabe, H. J. Qiu, K. Sugawara, S. Heguri, N. H. Tu, K. K. Huynh, T. Fujita, T. Takahashi, K. Tanigaki, M. Chen, *Angew. Chem. Int. Ed.* **2014**, *53*, 4822–4826.

[265] Y. Xu, G. Shi, X. Duan, *Acc. Chem. Res.* **2015**, *48*, 1666–1675.

[266] P. M. Wilson, G. N. Mbah, T. G. Smith, D. Schmidt, R. Y. Lai, T. Hofmann, A. Sinitskii, *J. Mater. Chem. C* **2014**, *2*, 1879–1886.

[267] B. G. Choi, M. Yang, W. H. Hong, J. W. Choi, Y. S. Huh, *ACS Nano* **2012**, *6*, 4020–4028.

[268] H. Wang, D. Zhang, T. Yan, X. Wen, J. Zhang, L. Shi, Q. Zhong, *J. Mater. Chem. A* **2013**, *1*, 11778–11789.

[269] C. Wu, X. Huang, G. Wang, L. Lv, G. Chen, G. Li, P. Jiang, *Adv. Funct. Mater.* **2013**, *23*, 506–513.

[270] X. Cheng, D. Li, Y. Wu, R. Xu, Y. Yu, *J. Mater. Chem. A* **2019**, *7*, 4913–4921.

[271] S. Stankovich, D. A. Dikin, R. D. Piner, K. A. Kohlhaas, A. Kleinhammes, Y. Jia, Y. Wu, S. T. Nguyen, R. S. Ruoff, *Carbon* **2007**, *45*, 1558–1565.

[272] X. Wang, L. Zhi, K. Müllen, *Nano Lett.* **2008**, *8*, 323–327.

[273] H. C. Schniepp, J.-L. Li, M. J. McAllister, H. Sai, M. Herrera-Alonso, D. H. Adamson, R. K. Prud'homme, R. Car, D. A. Saville, I. A. Aksay, *J. Phys. Chem. B* **2006**, *110*, 8535–8539.

[274] A. Bagri, C. Mattevi, M. Acik, Y. J. Chabal, M. Chhowalla, V. B. Shenoy, *Nat. Chem.* **2010**, *2*, 581–587.

[275] C. Mattevi, G. Eda, S. Agnoli, S. Miller, K. A. Mkhoyan, O. Celik, D. Mastrogiovanni, G. Granozzi, E. Garfunkel, M. Chhowalla, *Adv. Funct. Mater.* **2009**, *19*, 2577–2583.

[276] Y. Mulyana, M. Uenuma, Y. Ishikawa, Y. Uraoka, *J. Phys. Chem. C* **2014**, *118*, 27372–27381.

[277] Y. Wang, Z. Shi, Y. Huang, Y. Ma, C. Wang, M. Chen, Y. Chen, *J. Phys. Chem. C* **2009**, *113*, 13103–13107.

[278] A. Ambrosi, C. K. Chua, A. Bonanni, M. Pumera, *Chem. Rev.* **2014**, *114*, 7150–7188.

[279] G. Liao, S. Chen, X. Quan, H. Yu, H. Zhao, *J. Mater. Chem.* **2012**, *22*, 2721–2726.

[280] D. Gunther, G. LeBlanc, D. Prasai, J. R. Zhang, D. E. Cliffel, K. I. Bolotin, G. K. Jennings, *Langmuir* **2013**, *29*, 4177–4180.

[281] G. LeBlanc, K. M. Winter, W. B. Crosby, G. K. Jennings, D. E. Cliffel, *Adv. Energy Mater.* **2014**, *4*, 1301953.

[282] E. Darby, G. LeBlanc, E. A. Gizzie, K. M. Winter, G. K. Jennings, D. E. Cliffel, *Langmuir* **2014**, *30*, 8990–8994.

[283] M. T. Reetz, *J. Am. Chem. Soc.* **2013**, *135*, 12480–12496.

[284] M. J. Smanski, H. Zhou, J. Claesen, B. Shen, M. A. Fischbach, C. A. Voigt, *Nat. Rev. Microbiol.* **2016**, *14*, 135–149.

[285] S. F. Rowe, G. Le Gall, E. V. Ainsworth, J. A. Davies, C. W. J. Lockwood, L. Shi, A. Elliston, I. N. Roberts, K. W. Waldron, D. J. Richardson, T. A. Clarke, L. J. C. Jeuken, E. Reisner, J. N. Butt, *ACS Catal.* **2017**, *7*, 7558–7566.

[286] C. M. Dundas, A. J. Graham, D. K. Romanovicz, B. K. Keitz, *ACS Synth. Biol.* **2018**, *7*, 2726–2736.

[287] C.-m. Ding, M.-l. Lv, Y. Zhu, L. Jiang, H. Liu, *Angew. Chem. Int. Ed.* **2015**, *54*, 1446–1451.

[288] T. Kobayashi, T. Mito, N. Watanabe, T. Suzuki, A. Shiraishi, Y. Ohashi, *J. Clin. Microbiol.* **2012**, *50*, 1606–1612.

[289] S. M. Strycharz-Glaven, L. M. Tender, *ChemSusChem* **2012**, *5*, 1106–1118.

[290] J. M. Stevens, O. Daltrop, J. W. A. Allen, S. J. Ferguson, *Acc. Chem. Res.* **2004**, *37*, 999–1007.

[291] R. A. O'Neil, D. E. Holmes, M. V. Coppi, L. A. Adams, M. J. Larrahondo, J. E. Ward, K. P. Nevin, T. L. Woodard, H. A. Vrionis, A. L. N'Guessan, D. R. Lovley, *Environ. Microbiol.* **2008**, *10*, 1218–1230.

[292] M. Embree, Y. Qiu, W. Shieu, H. Nagarajan, R. O'Neil, D. Lovley, K. Zengler, H. L. Drake, *Appl. Environ. Microbiol.* **2014**, *80*, 2918–2927.

[293] C. E. Levar, C. H. Chan, M. G. Mehta-Kolte, D. R. Bond, D. K. Newman, *mBio* **2014**, *5*, e02034–14.

[294] Z. Wang, M. Gerstein, M. Snyder, *Nat. Rev. Genet.* **2009**, *10*, 57–63.

[295] A. Wagner, *Mol. Biol. Evol.* **2005**, *22*, 1365–1374.

[296] C. H. Chan, C. E. Levar, F. Jiménez-Otero, D. R. Bond, G. O'Toole, *J. Bacteriol.* **2017**, *199*, e00340–17.

[297] L. Shi, T. C. Squier, J. M. Zachara, J. K. Fredrickson, *Mol. Microbiol.* **2007**, *65*, 12–20.

[298] E. Afkar, G. Reguera, M. Schiffer, D. R. Lovley, *BMC Microbiol.* **2005**, *5*, 41.

[299] C. Leang, M. V. Coppi, D. R. Lovley, *J. Bacteriol.* **2003**, *185*, 2096–2103.

[300] J. E. Butler, F. Kaufmann, M. V. Coppi, C. Núñez, D. R. Lovley, *J. Bacteriol.* **2004**, *186*, 4042–4045.

[301] T. C. Santos, M. A. Silva, L. Morgado, J. M. Dantas, C. A. Salgueiro, *Dalton Trans.* **2015**, *44*, 9335–9344.

[302] T. Ueki, L. N. DiDonato, D. R. Lovley, *FEMS Microbiol. Lett.* **2017**, *364*, fnx093.

[303] D. R. Lovley, *Annu. Rev. Microbiol.* **2017**, *71*, 643–664.

[304] J. K. Fredrickson, M. F. Romine, A. S. Beliaev, J. M. Auchtung, M. E. Driscoll, T. S. Gardner, K. H. Nealson, A. L. Osterman, G. Pinchuk, J. L. Reed, D. A. Rodionov, J. L. M. Rodrigues, D. A. Saffarini, M. H. Serres, A. M. Spormann, I. B. Zhulin, J. M. Tiedje, *Nat. Rev. Microbiol.* **2008**, *6*, 592–603.

[305] A. Kröger, V. Geisler, E. Lemma, F. Theis, R. Lenger, *Arch. Microbiol.* **1992**, *158*, 311–314.

[306] S. Kalathil, K. P. Katuri, A. S. Alazmi, S. Pedireddy, N. Kornienko, P. M. F. J. Costa, P. E. Saikaly, *Chem. Mater.* **2019**, *31*, 3686–3693.

[307] S. Pei, H.-M. Cheng, *Carbon* **2012**, *50*, 3210–3228.

[308] M. Zhou, Y. Wang, Y. Zhai, J. Zhai, W. Ren, F. Wang, S. Dong, *Chem. Eur. J.* **2009**, *15*, 6116–6120.

[309] J. Warnan, J. Willkomm, J. N. Ng, R. Godin, S. Prantl, J. R. Durrant, E. Reisner, *Chem. Sci.* **2017**, *8*, 3070–3079.

[310] M. Rosenbaum, F. Aulenta, M. Villano, L. T. Angenent, *Bioresour. Technol.* **2011**, *102*, 324–333.

[311] J. Willkomm, K. L. Orchard, A. Reynal, E. Pastor, J. R. Durrant, E. Reisner, *Chem. Soc. Rev.* **2016**, *45*, 9–23.

[312] Y. Park, K. J. McDonald, K.-S. Choi, *Chem. Soc. Rev.* **2013**, *42*, 2321–2337.

[313] A. Bachmeier, B. J. Murphy, F. A. Armstrong, *J. Am. Chem. Soc.* **2014**, *136*, 12876–12879.

[314] G. A. M. Hutton, B. Reuillard, B. C. M. Martindale, C. A. Caputo, C. W. J. Lockwood, J. N. Butt, E. Reisner, *J. Am. Chem. Soc.* **2016**, *138*, 16722–16730.

[315] N. Antonovsky, S. Gleizer, E. Noor, Y. Zohar, E. Herz, U. Barenholz, L. Zelcbuch, S. Amram, A. Wides, N. Tepper, D. Davidi, Y. Bar-On, T. Bareia, D. G. Wernick, I. Shani, S. Malitsky, G. Jona, A. Bar-Even, R. Milo, *Cell* **2016**, *166*, 115–125.

[316] A. R. Rowe, S. Xu, E. Gardel, A. Bose, P. Girguis, J. P. Amend, M. Y. El-Naggar, M. W. Ribbe, *mBio* **2019**, *10*, e02448–18.

[317] A.-E. Rotaru, P. M. Shrestha, F. Liu, B. Markovaite, S. Chen, K. P. Nevin, D. R. Lovley, G. Voordouw, *Appl. Environ. Microbiol.* **2014**, *80*, 4599–4605.

[318] J. S. Deutzmann, A. M. Spormann, *ISME J.* **2017**, *11*, 704–714.

[319] T. W. Woolerton, S. Sheard, E. Reisner, E. Pierce, S. W. Ragsdale, F. A. Armstrong, *J. Am. Chem. Soc.* **2010**, *132*, 2132–2133.

[320] K. A. Brown, M. B. Wilker, M. Boehm, G. Dukovic, P. W. King, *J. Am. Chem. Soc.* **2012**, *134*, 5627–5636.

[321] K. A. Brown, D. F. Harris, M. B. Wilker, A. Rasmussen, N. Khadka, H. Hamby, S. Keable, G. Dukovic, J. W. Peters, L. C. Seefeldt, P. W. King, *Science* **2016**, *352*, 448–450.

[322] B. Wang, C. Zeng, K. H. Chu, D. Wu, H. Y. Yip, L. Ye, P. K. Wong, *Adv. Energy Mater.* **2017**, *7*, 1700611.

[323] N. Kornienko, K. K. Sakimoto, D. M. Herlihy, S. C. Nguyen, A. P. Alivisatos, C. B. Harris, A. Schwartzberg, P. Yang, *Proc. Natl. Acad. Sci. U.S.A* **2016**, *113*, 11750–11755.

[324] F. Rudroff, M. D. Mihovilovic, H. Gröger, R. Snajdrova, H. Iding, U. T. Bornscheuer, *Nat. Catal.* **2018**, *1*, 12–22.

[325] S. K. Kuk, R. K. Singh, D. H. Nam, R. Singh, J.-K. Lee, C. B. Park, *Angew. Chem. Int. Ed.* **2017**, *56*, 3827–3832.

[326] K. Köninger, Á. Gómez Baraibar, C. Mügge, C. E. Paul, F. Hollmann, M. M. Nowaczyk, R. Kourist, *Angew. Chem. Int. Ed.* **2016**, *55*, 5582–5585.

[327] J. Ni, H.-Y. Liu, F. Tao, Y.-T. Wu, P. Xu, *Angew. Chem. Int. Ed.* **2018**, *57*, 15990–15994.

[328] J. Guo, M. Suástegui, K. K. Sakimoto, V. M. Moody, G. Xiao, D. G. Nocera, N. S. Joshi, *Science* **2018**, *362*, 813–816.

[329] M. A. TerAvest, C. M. Ajo-Franklin, *Biotechnol. Bioeng.* **2016**, *113*, 687–697.

[330] M. A. TerAvest, T. J. Zajdel, C. M. Ajo-Franklin, *ChemElectroChem* **2014**, *1*, 1874–1879.

[331] D. Choi, S. B. Lee, S. Kim, B. Min, I.-G. Choi, I. S. Chang, *Bioresour. Technol.* **2014**, *154*, 59–66.

[332] Y. Chen, P. Li, H. Noh, C.-W. Kung, C. T. Buru, X. Wang, X. Zhang, O. K. Farha, *Angew. Chem. Int. Ed.* **2019**, *58*, 7682–7686.

[333] Z. Ji, H. Zhang, H. Liu, O. M. Yaghi, P. Yang, *Proc. Natl. Acad. Sci. U.S.A* **2018**, *115*, 10582–10587.

[334] N.-H. Tran, D. Nguyen, S. Dwaraknath, S. Mahadevan, G. Chavez, A. Nguyen, T. Dao, S. Mullen, T.-A. Nguyen, L. E. Cheruzel, *J. Am. Chem. Soc.* **2013**, *135*, 14484–14487.

[335] I. J. Iwuchukwu, M. Vaughn, N. Myers, H. O'Neill, P. Frymier, B. D. Bruce, *Nat. Nanotechnol.* **2009**, *5*, 73–79.

[336] H. Zhang, H. Liu, Z. Tian, D. Lu, Y. Yu, S. Cestellos-Blanco, K. K. Sakimoto, P. Yang, *Nat. Nanotechnol.* **2018**, *13*, 900–905.

[337] Y. V. Lee, B. Tian, *Nano Lett.* **2019**, *19*, 2189–2197.

[338] J. H. Park, S. H. Lee, G. S. Cha, D. S. Choi, D. H. Nam, J. H. Lee, J.-K. Lee, C.-H. Yun, K. J. Jeong, C. B. Park, *Angew. Chem. Int. Ed.* **2015**, *54*, 969–973.

[339] G. Fan, C. M. Dundas, A. J. Graham, N. A. Lynd, B. K. Keitz, *Proc. Natl. Acad. Sci. U.S.A* **2018**, *115*, 4559–4564.

[340] T.-s. Song, H. Zhang, H. Liu, D. Zhang, H. Wang, Y. Yang, H. Yuan, J. Xie, *Bioresour. Technol.* **2017**, *243*, 573–582.

[341] C. A. Caputo, M. A. Gross, V. W. Lau, C. Cavazza, B. V. Lotsch, E. Reisner, *Angew. Chem. Int. Ed.* **2014**, *53*, 11538–11542.

[342] C. A. Caputo, L. Wang, R. Beranek, E. Reisner, *Chem. Sci.* **2015**, *6*, 5690–5694.

[343] M. B. Wilker, K. E. Shinopoulos, K. A. Brown, D. W. Mulder, P. W. King, G. Dukovic, *J. Am. Chem. Soc.* **2014**, *136*, 4316–4324.

[344] G. Ciamician, *Science* **1912**, *36*, 385–394.

[345] N. Armaroli, V. Balzani, *Angew. Chem. Int. Ed.* **2007**, *46*, 52–66.